

UNIVERSIDAD CARLOS III DE MADRID



Escuela Politécnica Superior

**ABSOLUTE INSTABILITY IN THE NEAR FIELD OF
LOW-DENSITY JETS**

Tesis Doctoral

Autor
Wilfried Coenen

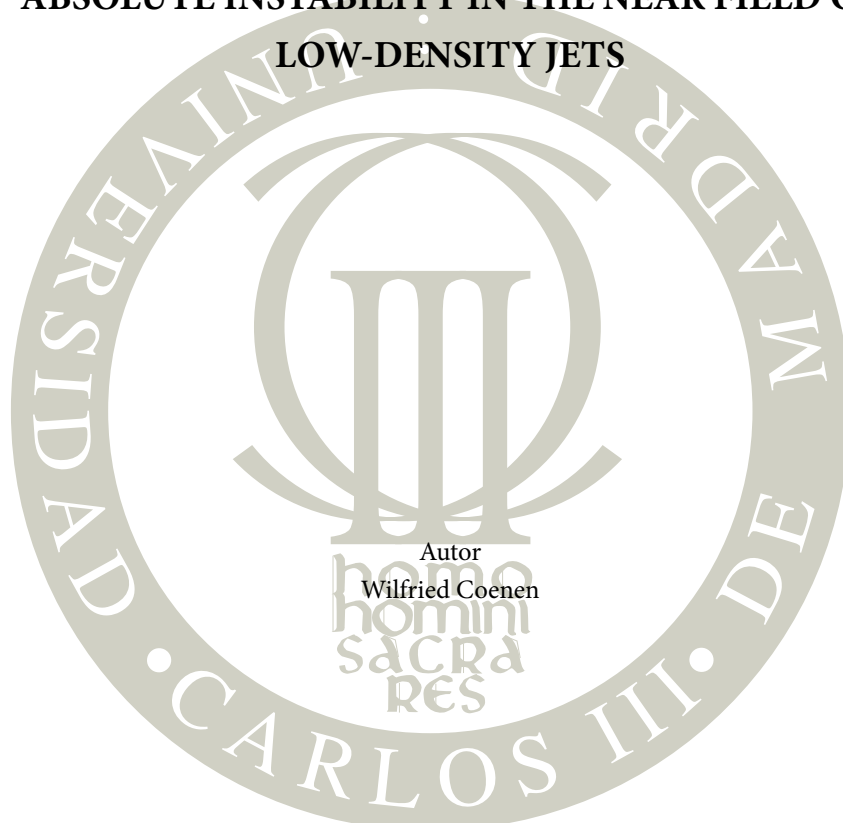
Director
Alejandro Sevilla Santiago

DEPARTAMENTO DE INGENIERÍA TÉRMICA Y DE FLUIDOS

Leganés, abril 2010

DEPARTAMENTO DE INGENIERÍA TÉRMICA Y DE FLUIDOS
Escuela Politécnica Superior

**ABSOLUTE INSTABILITY IN THE NEAR FIELD OF
LOW-DENSITY JETS**



Autor
Wilfried Coenen

Director de Tesis
Alejandro Sevilla Santiago

Leganés, abril 2010

To my parents, my brother, and to Ana

TESIS DOCTORAL

ABSOLUTE INSTABILITY IN THE NEAR FIELD OF LOW-DENSITY JETS

Autor: Wilfried Coenen

Director de Tesis: Alejandro Sevilla Santiago

Firma del Tribunal Calificador:

Firma

Presidente: D. Norman Riley

Vocal: D. Ramón Fernández Fera

Vocal: D. José Manuel Gordillo Arias de Saavedra

Vocal: D. Carlos Martínez Bazán

Secretario: D. Antonio Luis Sánchez Pérez

Suplente: D. Enrique Sanmiguel Rojas

Suplente: D. Carlos del Pino Peñas

Calificación:

Leganés, 5 de abril de 2010

Abstract

Variable density jets are known to support self-sustained oscillations when the jet-to-ambient density ratio is sufficiently small. This change in dynamical response to small perturbations is associated with a transition from convective to absolute instability of the underlying unperturbed base flow. The focus of this dissertation lies in the use of linear stability theory to describe the convective to absolute instability transition of buoyancy-free low-density jets emerging from a circular injector tube at moderately high Reynolds numbers and low Mach numbers. Particular interest is given to the influence of the length of the injector tube on the stability characteristics of the resulting jet flow, whose base velocity profile at the jet exit is computed in terms of the nondimensional tube length L_t by integrating the boundary layer equations along the injector.

We begin with the investigation of inviscid axisymmetric and helical modes of instability in a heated jet for different values of the jet-to-ambient density ratio. For short tubes $L_t \ll 1$ the base velocity profile at the tube exit is uniform except in a thin surrounding boundary layer. Correspondingly, the stability analysis reproduces previous results of uniform velocity jets, according to which the jet becomes absolutely unstable to axisymmetric modes for a critical density ratio $S_c \simeq 0.66$, and to helical modes for $S_c \simeq 0.35$. For tubes of increasing length the analysis reveals that both modes exhibit absolutely unstable regions for all values of L_t and small enough values of the density ratio. In the case of the helical mode, we find that S_c increases monotonically with L_t , reaching its maximum value $S_c \simeq 0.5$ as the exit velocity approaches the Poiseuille profile for $L_t \gg 1$. Concerning the axisymmetric mode, its associated value of S_c achieves a maximum value $S_c \simeq 0.9$ for $L_t \simeq 0.04$ and then decreases to approach $S_c \simeq 0.7$ for $L_t \gg 1$. The absolute growth rates in this limiting case of near-Poiseuille jet profiles are however extremely small for $m = 0$, in agreement with the fact that axisymmetric disturbances of a jet with parabolic profile are neutrally stable. As a result, for $S < 0.5$ the absolute growth rate of the helical mode becomes larger than that of the axisymmetric mode for sufficiently large values of L_t , suggesting that the helical mode may prevail in the instability development of very light jets issuing from long injectors.

A second part of this dissertation is devoted to the viscous linear instability of parallel gas flows with piecewise constant base profiles in the limit of low Mach numbers, both for planar and axisymmetric geometries such as mixing layers, jets and wakes. Our results generalize those of Drazin (*J. Fluid Mech.* vol. 10, 1961, p. 571), by contemplating

the possibility of arbitrary jumps in density and transport properties between two uniform streams separated by a vortex sheet. The eigenfunctions, obtained analytically in the regions of uniform flow, are matched through an appropriate set of jump conditions at the discontinuity of the basic flow, which are derived by repeated integration of the linearized conservation equations in their primitive variable form. The development leads to an algebraic dispersion relation that is validated through comparisons with stability calculations performed with continuous profiles and is applied, in particular, to study the effects of molecular transport on the spatiotemporal stability of parallel non-isothermal gaseous jets and wakes with very thin shear layers.

Finally we go back to the stability analysis of low-density jets emerging from circular nozzles or tubes, this time considering viscous perturbations so that the Reynolds number enters the stability problem. We consider separately the two particular cases of a hot gas jet discharging into a colder ambient of the same gas, as well as the isothermal discharge of a jet of gas with molecular weight smaller than that of the ambient gas. In both cases, we consider the detailed downstream evolution of the local stability properties in the near field of the jet with the aim at establishing the convective or absolute nature of the instability. We discuss the relationship of our results with those obtained in previous works with use made of parametric velocity and density profiles, and compare both approaches with the actual global transition observed in experiments performed with hot and light jets.

Resumen

Los chorros sumergidos con densidad variable presentan oscilaciones auto-excitadas cuando la relación de densidad chorro/ambiente es suficientemente pequeña. Este cambio en la respuesta dinámica del chorro está asociado a la transición entre inestabilidad convectiva y absoluta en el flujo base no perturbado. La presente tesis doctoral se centra en el uso de la teoría de estabilidad lineal para describir dicha transición en el caso de chorros laminares libres de menor densidad que el ambiente, descargando desde un inyector cilíndrico a altos números de Reynolds, bajos números de Mach, y con efectos de flotabilidad despreciables. Se presta especial atención al efecto de la longitud del tubo de inyección sobre las propiedades de estabilidad del chorro, cuyo perfil inicial de velocidad se describe a través de un parámetro adimensional L_t mediante la integración de las ecuaciones de capa límite en la región de entrada del inyector.

Se comienza con un estudio de estabilidad no viscosa para chorros calientes axisimétricos de gas, considerando tanto el modo de inestabilidad axisimétrico como el helicoidal en función de la relación de densidad chorro/ambiente. En el límite de inyectores cortos, $L_t \ll 1$, el perfil de velocidad en la salida es uniforme excepto en una capa límite anular de pequeño espesor. En este caso, el análisis de estabilidad reproduce resultados conocidos para chorros de velocidad uniforme: los modos axisimétrico y helicoidal se hacen absolutamente inestables para valores de la relación de densidad por debajo de sendos valores críticos, respectivamente dados por $S_c \simeq 0.66$ y $S_c \simeq 0.35$. El análisis realizado revela que, conforme aumenta la longitud del tubo, ambos modos poseen regiones de inestabilidad absoluta para cualquier valor de L_t y relaciones de densidad suficientemente pequeñas. En el caso del modo helicoidal, se ha encontrado que S_c crece monótonamente con L_t , alcanzando asintóticamente su valor máximo $S_c \simeq 0.5$ cuando el perfil de velocidad inicial tiende al perfil de Poiseuille en el límite $L_t \gg 1$. En el caso del modo axisimétrico, el correspondiente valor de S_c alcanza un máximo local $S_c \simeq 0.9$ para $L_t \simeq 0.04$, y luego decrece hasta alcanzar un valor asintótico $S_c \simeq 0.7$ para $L_t \gg 1$. Sin embargo, el ritmo de crecimiento absoluto del modo axisimétrico en el límite de perfiles próximos al de Poiseuille se hace muy pequeño, de acuerdo con el hecho de que las perturbaciones axisimétricas en un chorro libre con perfil de Poiseuille son neutralmente estables. En consecuencia, para $S < 0.5$ el ritmo de crecimiento absoluto del modo helicoidal se hace mayor que el del modo axisimétrico para valores suficientemente grandes de L_t , lo que sugiere que el modo helicoidal podría prevalecer

en chorros de muy pequeña densidad descargando desde inyectores muy largos.

En la segunda parte de la tesis se aborda el problema de estabilidad lineal viscosa de flujos paralelos de gas con perfiles base uniformes a trozos, en el límite de bajos números de Mach, contemplando geometrías planas y cilíndricas como capas de mezcla, chorros y estelas. Los resultados obtenidos representan una generalización del trabajo de Drazin (*J. Fluid Mech.* vol. 10, 1961, p. 571), contemplando la posibilidad de saltos arbitrarios en la densidad y en las propiedades de transporte entre dos corrientes uniformes separadas por una capa de torbellinos. Las autofunciones se proporcionan analíticamente en las regiones de flujo uniforme, y se acoplan en la capa de torbellinos mediante unas condiciones de salto apropiadas, obtenidas mediante integración sucesiva de las ecuaciones de conservación linealizadas en variables primitivas. El desarrollo permite obtener una relación de dispersión algebraica, que se valida mediante comparaciones con cálculos de estabilidad realizados con perfiles continuos, y que se aplica, en particular, para estudiar los efectos del transporte molecular sobre la estabilidad espacio-temporal de chorros y estelas de gas con capas de cortadura muy delgadas.

Finalmente, se retoma el estudio de la estabilidad local espacio-temporal de chorros de baja densidad descargando desde un inyector cilíndrico o desde una tobera, pero considerando perturbaciones viscosas, de modo que aparece el número de Reynolds como parámetro adicional en el problema de estabilidad. Se consideran separadamente los casos de chorros de gas con temperatura mayor pero igual composición que el ambiente, así como de chorros isoterms con menor peso molecular que la atmósfera en reposo en la que descargan, comúnmente denominados chorros calientes y chorros ligeros, respectivamente. En ambos casos, se considera en detalle la evolución aguas abajo de las propiedades de estabilidad local en el campo cercano del chorro, con el fin de establecer el carácter convectivo o absoluto de la inestabilidad. Se discute la relación de los resultados obtenidos con trabajos anteriores en los que se hace uso de perfiles paramétricos de velocidad, y se comparan ambos con la transición que se observa experimentalmente en chorros calientes y ligeros.

Contents

Abstract	i
Resumen	iii
1 Introduction and theoretical background	1
1.1 Introduction	1
1.2 Outline of the dissertation	4
1.3 Theoretical background	5
1.3.1 Conservation equations for slender low-density jets	5
1.3.2 Linear stability equations	9
1.3.3 Local absolute/convective instability	12
1.3.4 Relation between local and global instability	20
References	22
2 Inviscid stability of light jets emerging from injector tubes	27
2.1 Introduction	28
2.2 Formulation	31
2.3 Linear instability of the jet flow	35
2.4 Conclusions	44
References	45
3 Viscous stability analysis of flows with discontinuous base profiles	49
3.1 Introduction	49
3.2 Stability equations for low-Mach-number parallel flows	51
3.3 Boundary conditions for the disturbances at a discontinuity	54
3.4 Stability eigenproblem with piecewise-constant base profiles	59
3.4.1 Stability equations for uniform base profiles	61
3.4.2 Jets and wakes with symmetric base profiles	62
3.5 Application to the stability of non-isothermal jets and wakes	64
3.5.1 Temporal stability analysis	66
3.5.2 Spatiotemporal stability analysis and A/C transition	68
3.6 Conclusions	74

vi CONTENTS

3.7 Appendix: The dispersion relation	76
References	77
4 Viscous absolute instability of hot and light round jets	79
4.1 Introduction	79
4.2 Formulation	81
4.3 Results	83
4.4 Conclusions	90
References	90
5 General conclusions and future prospects	93
References	95
A Numerical methods	97
A.1 Numerical integration of the jet flow	97
A.2 Chebyshev spectral collocation method	98
A.3 Saddle point determination	100
References	100
Alphabetical list of references	103
Curriculum Vitae	111

Introduction and theoretical background

1.1 Introduction

Self-sustained oscillations in open shear flows

Jets, wakes, mixing layers and boundary layers are examples of commonly encountered *open shear flows*. These flows are characterized by a strong shear in the cross-stream direction, and typically exhibit a spatial development along the stream, starting from a well-defined point in space, for example the injector or nozzle exit plane from which a free jet emerges. The term *open shear flows* refers to the fluid particles entering and leaving the domain of interest in finite time without being recycled, as opposed to *closed* flows such as the Couette flow between two concentric rotating cylinders or Rayleigh-Bénard convection.

Open shear flows are known to be extremely sensitive to perturbations, i.e. they are known to act as *noise amplifiers*. A beautiful example of this behavior is the ‘singing flame’, first described by Leconte in 1858, who noticed a gaslight exhibit pulsations that were synchronous with the audible beats of music. Tyndall (1867) later found that the fluid of the jet itself was sensitive to sound.

The basic physical mechanisms underlying this highly unstable nature of free shear flows were uncovered during the second half of the 19th century in the seminal works of Helmholtz (1868), Kelvin (1871) and Rayleigh (1880). Since then, many efforts have been devoted to improving our understanding of their dynamics both in the linear and non-linear regimes. Despite the existence of several universal features, their detailed spatiotemporal development is affected by a variety of physical effects, whose study has been the focus of a considerable number of works (see for instance the reviews Ho & Huerre, 1985; Huerre, 2000, and references therein).

Most of the early work on the stability of free shear flows was aimed at obtaining the curves of neutral stability, using *temporal stability theory*, where the instability is represented as a wave with a given spatial periodicity of infinite extent (a given wavenumber k) that evolves in time with an unknown frequency and is either amplified or damped (unknown complex frequency ω). This approach, although successful in predicting sta-

bility characteristics of closed flows, resulted unsatisfactory in the study of open shear flows. It was found that a *spatial stability analysis* yields much more reliable results (see for example Michalke, 1965). Here, the downstream development of vortical structures as responses to small perturbations is modeled as a collection of spatially evolving instability waves of various frequencies. In the stability calculations a complex wavenumber k is thus obtained for a given real frequency ω . In the case of small growth rates, Gaster (1962) showed that the temporal and spatial analyses are related through an appropriate change of reference frame (Gaster's transformation). However, in highly unstable situations like high-Reynolds free shear flows there is no such simple relationship between both approaches, which must be considered separately.

The stability analyses of the type described above assume the base flow to be strictly parallel. For open shear flows, this is a reasonable approximation if their spatial development is slow or, in other words, if they are slender flows. In general, this happens when the associated Reynolds number is sufficiently high, while remaining smaller than the critical Reynolds number above which the flow becomes turbulent. However, the critical Reynolds numbers of free shear flows happen to be far smaller than those encountered in most applications. Nevertheless, large-scale coherent structures are present in open shear flows at high Reynolds numbers, as discovered by Crow & Champagne (1971) for the shear-layer of a jet and by Brown & Roshko (1974) for the turbulent mixing layer. These large-scale vortical structures still exhibit some of the characteristics of spatially evolving instability waves, originating from the amplification of upstream disturbances. The separation of scales between the small-scale turbulence and the large-scale vortical coherent structures can then be exploited to perform a spatial stability analysis on the time-averaged flow. This procedure gives reasonable results in predicting the dynamics of open shear flows in the turbulent regime.

In contrast to the noise amplifying flows described above, some open shear flows such as low-density jets and bluff-body wakes can behave as *oscillators*. They exhibit *intrinsic* dynamics similar to closed-flow systems, where global instability modes can be observed that are synchronized in the streamwise direction. To explain this behavior, the concepts of *absolute* and *convective instability*, theoretically founded by plasma physicists in the 1950's (Twiss, 1951*b,a*, 1952; Landau & Lifschitz, 1954, 1959; Sturrock, 1958), were introduced to the field of fluid mechanics almost twenty years later (see for instance Gaster, 1968; Tam, 1971; Huerre & Monkewitz, 1985). In contrast to temporal and spatial stability analyses, in a *spatiotemporal* analysis, instability waves are permitted to grow or decay both in space and in time. In other words, both the wavenumber k and the frequency ω are complex. An observer moving along the flow at a certain velocity can then see the instability waves growing or decaying. If the disturbance is seen to be damped for all possible velocities of the observer, the flow is *stable*. However, if there exist at least one reference frame moving at a certain velocity in which the perturbation

grows, the flow is *unstable*. Furthermore, if in the latter case the disturbance grows in time in the laboratory frame (zero velocity), the flow is called *absolutely unstable*. This means that the disturbances grow at the place where they are introduced. In the opposite case, the flow is *convectively unstable*, as the perturbations are convected away faster than they are amplified at the source.

The concepts of absolute and convective instability are *local* concepts, rigorously defined for strictly parallel base flows. In spatially developing shear flows, the local convective/absolute instability is thus a function of the streamwise coordinate. However, given the spatial development of the flow is slow enough, a close relation exists between the distribution of the local instability properties and the *global* stability of the flow (see Huerre & Monkewitz, 1990; Chomaz, 2005). In particular, a global self-sustained instability mode may be triggered by a region of absolute instability in the flow. This justifies the use of local stability theory to explain experimental observations of self-sustained oscillations in spatially developing open shear flows, in this way avoiding the huge increase in computational complexity and the reduced physical transparency that a global linear stability analysis (Theofilis, 2003) would imply.

Absolute instability of low-density jets

Among the various open shear flows, free jets were found to be of growing interest since jet propulsion became feasible. The instability of jets was related to laminar-turbulent transition and the generation of noise in jet engines.

The instability of constant-density jets to small perturbations has been studied in numerous theoretical and experimental works (see for instance Batchelor & Gill, 1962; Reynolds, 1962; Kambe, 1969; Lessen & Singh, 1973; Mollendorf & Gebhart, 1973; Mattingly & Chang, 1974; Morris, 1976; Cohen & Wygnanski, 1987).

The distinguished stability features of jets with a density smaller than the ambient value were first noticed by Michalke (1970). When studying the inviscid stability of a compressible cylindrical vortex sheet, he found that the spatial stability theory failed when the jet-to-ambient density ratio became smaller than a certain critical value. Huerre & Monkewitz (1985) associated this failure with a transition from convective to absolute instability of the underlying parallel base flow, opening the path for a variety of studies whose main objective is the prediction of the critical density ratio at which this transition occurs as a function of other control parameters such as the Reynolds, Mach, and Richardson numbers or the presence of ambient coflow or counterflow. (Monkewitz & Sohn, 1988; Yu & Monkewitz, 1990; Jendoubi & Strykowski, 1994; Sevilla *et al.*, 2002; Lesshafft & Huerre, 2007; Hallberg *et al.*, 2007; Nichols *et al.*, 2007; Srinivasan *et al.*, 2010). It is common practice in these studies to model the downstream evolution of the jet base flow with a family of velocity and density profiles of presumed shape. For

circular jets emerging from nozzles a hyperbolic tangent profile is seen to give a good fit with experimental velocity measurements (Monkewitz & Sohn, 1988). The profiles are parametric in the sense that the momentum thickness is introduced to adjust the thickness of the jet shear layer.

Experimental evidence of the intense self-sustained oscillations in light jets at low jet-to-ambient density ratios were given by Sreenivasan *et al.* (1989); Kyle & Sreenivasan (1993); Hallberg & Strykowski (2006) using helium/air mixtures and by Monkewitz *et al.* (1990); Raghu & Monkewitz (1991) using heated air jets.

As mentioned above, the downstream evolution of the local spatiotemporal stability characteristics is related to the actual behavior of the jet in the nonlinear regime. Numerical simulations by Lesshafft *et al.* (2006, 2007) show that the global mode, leading to the self-excited behavior of the jet, can be triggered by a pocket of absolute instability. A detailed study of the local stability characteristics in the near field of the jet is thus essential when studying the appearance of self-sustained oscillations in low-density jets. It is at this point that the question arises as to what extent the parametric representations of the base flow can account for the actual stability properties of low-density jets.

The question above directly motivates the main objective of this dissertation: using realistic base flow profiles, calculated with numerical simulations, to study the local spatiotemporal stability properties in the near field of low-density jets. Furthermore, we do not restrict ourselves to the study of nozzle jets, but treat the more general case of jets emerging from circular injector tubes with variable length.

In the remainder this introductory chapter, we give a brief overview of the theoretical background that is needed in the subsequent chapters, followed by the outline of the dissertation.

1.2 Outline of the dissertation

The present dissertation is organized as follows. Chapter 2 presents the inviscid stability analysis of low-density jets emerging from circular injector tubes. The transition from convective to absolute instability is calculated as a function of the nondimensional tube length and the jet-to-ambient density ratio. The results of this chapter can also be found in Coenen *et al.* (2008). In chapter 3 we describe how discontinuous base flow profiles can be used to study the viscous stability properties of variable-density flows with very thin shear layers. Chapter 4 is a natural extension of chapter 2, treating the absolute instability of low-density jets, but retaining the effect of the viscosity in the stability analysis. Furthermore, attention is given to effect of the mixing properties by treating the cases of heated jets and jets with variable molecular weight separately. Finally, in appendix A, the finite difference method that is employed to solve the jet flow field is

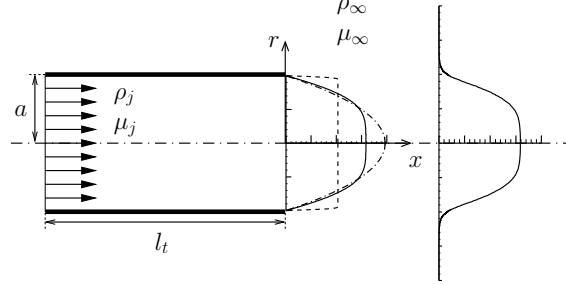


Figure 1.1: Sketch of the flow configuration considered in the present work. Numerical results for the velocity profiles at the jet exit for injector tube lengths $L_t = 10^{-4}$ (dashed line), $L_t = 0.04$ (solid line), and $L_t = 0.2$ (dot-dashed line), and the hot jet profile at a downstream position $x = 10^{-3}$ for $L_t = 0.04$ and $S = 0.8$.

described, as well as the spectral method to solve the eigenvalue problem involved in the viscous stability problem, together with a root-finding method to locate saddle points in the complex frequency plane.

1.3 Theoretical background

1.3.1 Conservation equations for slender low-density jets

We consider a jet of density ρ_j and viscosity μ_j discharging with a flow rate Q from a circular injector tube of radius a and length l_t into an infinite atmosphere of a heavier fluid of density ρ_j . Buoyancy effects are neglected, as corresponds to a small Richardson number $Ri = (\rho_\infty - \rho_j)ga/(\rho_j U_j^2) \ll 1$. The Reynolds number $Re = \rho_j U_j a / \mu_j \gg 1$ based on the average velocity $U_j = Q/(\pi a^2)$ is assumed to be large, so that the corresponding steady solution is a jet flow of characteristic length $Re a \gg 1$, which is sketched in figure 1.1, where r and x denote the radial and axial coordinates scaled with their characteristic values a and $Re a$, respectively. We will see later that the local stability characteristics of the jet at each axial location x are functions of the local velocity and density profiles $U(r)$ and $\rho(r)$, nondimensionalized with their characteristic values U_j and ρ_j .

The initial velocity profile $U_e(r)$ at the jet exit depends on the upstream axisymmetric laminar flow along the injector tube, the fluid entering the latter with uniform velocity U_j . The density will remain constant along the tube provided that heat conduction from the injector wall is negligible and that the Mach number $Ma = U_j/c_0$ is small, with c_0 denoting the speed of sound in the fluid. Furthermore, if the Reynolds number Re associated with this *entry flow* is smaller than a critical value, the flow along

the tube remains steady. As $Re \gg 1$, we can use the boundary-layer approximation to solve the flow field in the injector tube, reducing the problem to that of integrating the continuity and momentum equations

$$\frac{\partial}{\partial x}(rU) + \frac{\partial}{\partial r}(rV) = 0, \quad (1.1a)$$

and

$$U \frac{\partial U}{\partial x} + V \frac{\partial U}{\partial r} = -P_l + \frac{1}{r} \frac{\partial}{\partial r} \left(r \frac{\partial U}{\partial r} \right), \quad (1.1b)$$

with initial conditions $U = 1$ at $x = -L_t$, and boundary conditions $\partial U/\partial r = V = 0$ at $r = 0$ and $U = V = 0$ at $r = 1$ for $x > -L_t$. Here, $L_t = l_t/(Re a)$ is the rescaled injector length, V represents the radial velocity component scaled with its characteristic value $\mu_j/(\rho_j a)$ and $P_l(x)$ is a rescaled pressure gradient, to be determined at each x location along the injector as part of the computation. To integrate the problem numerically, the method of lines Holmes (2007) can be employed. To that end, the equations of motion are discretized in the radial direction r with a centered second-order scheme and then written as a system of ordinary differential equations in the axial direction x , that can be integrated numerically with a fourth-order Runge-Kutta method. In figure 1.1 we show sample velocity profiles for $L_t = (10^{-4}, 0.04, 0.2)$. As explained in Kucheman *et al.* (1963), for short injectors with $L_t \ll 1$, the velocity remains nearly uniform, except in the vicinity of the injector wall, where there exists a thin annular boundary layer of characteristic thickness $L_t^{1/2} a$. This Blasius boundary layer is not restricted to straight tubular injectors, but also appears in the initial velocity profile of a jet emerging from a convergent nozzle at a finite Reynolds number. We can thus anticipate that for short injector tubes, our results will be equivalent to those for nozzle jets, given the thickness of the boundary layer is the same. However, for longer injectors of rescaled length $L_t \sim O(1)$ viscous shear stresses act all across the tube, modifying the velocity profile $U_e(r)$, which approaches the parabolic Poiseuille profile $U_e(r) = 2(1 - r^2)$ for $L_t \gg 1$.

When describing the jet flow field, we have to take into account the mixing of the jet with the ambient, which determines the distributions of density and transport properties in the jet development region as a function of the local temperature and composition. For simplicity, the effects of temperature and composition will be treated separately below by considering two particular configurations: the case of a hot jet of temperature T_j emerging into a colder ambient of the same fluid at a temperature T_∞ and the case of an isothermal jet with molecular weight \bar{W}_j emerging into an ambient fluid with a higher molecular weight \bar{W}_∞ . The jet-to-ambient density ratio for these two cases is given by $S = T_\infty/T_j$ and $S = \bar{W}_j/\bar{W}_\infty$, respectively. As seen below, both the equation

of state and the expressions for the transport properties take also different forms for each of the two cases.

The steady solutions for these slender flows can be calculated with small relative errors of order Re^{-2} by integrating numerically the axisymmetric boundary-layer equations written in a dimensionless form independent of the Reynolds number, which, for mass and momentum conservation, take the form

$$\frac{\partial}{\partial x}(\rho r U) + \frac{\partial}{\partial r}(\rho r V) = 0, \quad (1.2)$$

and

$$\rho \left(U \frac{\partial U}{\partial x} + V \frac{\partial U}{\partial r} \right) = \frac{1}{r} \frac{\partial}{\partial r} \left(\mu r \frac{\partial U}{\partial r} \right), \quad (1.3)$$

where the viscosity μ is nondimensionalized with its value μ_j at the jet exit. These equations need to be integrated with initial conditions at $x = 0$ given by $U = U_e(r)$ for $r \leq 1$ and $U = 0$ for $r > 1$, and with boundary conditions for $x > 0$ given by $\partial U / \partial r = V = 0$ at $r = 0$ and $U = 0$ as $r \rightarrow \infty$.

For the hot jet we also need to consider the energy equation, written in the boundary-layer low-Mach-number form

$$\rho \left(U \frac{\partial T}{\partial x} + V \frac{\partial T}{\partial r} \right) = \frac{1}{Pr} \frac{1}{r} \frac{\partial}{\partial r} \left(\mu r \frac{\partial T}{\partial r} \right). \quad (1.4)$$

This equation is to be integrated with initial conditions $T = 1$ for $r \leq 1$ and $T = S$ for $r > 1$ at $x = 0$, and with boundary conditions for $x > 0$ given by $\partial T / \partial r = 0$ at $r = 0$ and $T = S$ as $r \rightarrow \infty$. Here, the temperature T and thermal conductivity κ are scaled with the jet values T_j and κ_j , and the Prandtl number is defined as $Pr = c_p \mu_j / \kappa_j$. The conservation equations need to be supplemented with the equation of state written in the quasi-isobaric approximation

$$\rho T = 1, \quad (1.5)$$

and with the presumed power-law temperature dependence

$$\mu = \kappa = T^\sigma \quad (1.6)$$

for the transport properties. In writing the latter, we have further assumed that both the Prandtl number Pr and the specific heat at constant pressure c_p take constant values throughout the flow field, an assumption that yields $\mu = \kappa$. Typical values for Pr and for σ in non-ionized gases are $Pr \simeq 0.7$ and $0.5 < \sigma < 0.7$.

The description of the discharge of a jet into an ambient with the same temperature

does not need the employment the energy equation, in that the flow remains isothermal everywhere for the low Mach number flows considered here. In this case, the density and transport properties are a function of the composition, to be determined by integration of the species conservation equations. For a binary mixture, the problem is simpler, in that a single equation, written for instance for the mass fraction Y of the lighter species, needs to be considered, with the mass fraction of the heavier species being obtained as the difference $1 - Y$. Consider for instance a jet composed of a mixture of helium and nitrogen emerging into a nitrogen atmosphere, an arrangement often encountered in experiments (extension to other binary flow configurations would be straightforward). The mean molecular weight \bar{W}_j at the jet exit is related to the molecular weights W_{He} and W_{N_2} of the two species through the jet-exit value of the mass fraction $Y = Y_j$ of the lighter component, in this case helium:

$$\bar{W}_j = \left(\frac{Y_j}{W_{\text{He}}} + \frac{1 - Y_j}{W_{\text{N}_2}} \right)^{-1}. \quad (1.7)$$

The jet-to-ambient density ratio, defined as $S = \bar{W}_j / \bar{W}_\infty = \bar{W}_j / \bar{W}_{\text{N}_2} = \rho_j / \rho_\infty = \rho_j / \rho_{\text{N}_2}$, is then related to Y_j by

$$Y_j = \frac{1/S - 1}{W_{\text{N}_2}/W_{\text{He}} - 1}. \quad (1.8)$$

Note that at each location in the jet the density ρ , scaled with its value ρ_j at the jet exit, can be expressed as

$$\rho = \frac{1}{(1 - S)Y/Y_j + S}. \quad (1.9)$$

The corresponding conservation equation for helium

$$\rho \left(U \frac{\partial Y}{\partial x} + V \frac{\partial Y}{\partial r} \right) = \frac{1}{Sc} \frac{1}{r} \frac{\partial}{\partial r} \left(\rho r \frac{\partial Y}{\partial r} \right), \quad (1.10)$$

is to be integrated with initial conditions at $x = 0$ given by $Y = Y_j$ for $r \leq 1$ and $Y = 0$ for $r > 1$, and with boundary conditions for $x > 0$ given by $\partial Y / \partial r = 0$ at $r = 0$ and $Y = 0$ as $r \rightarrow \infty$. In the formulation, the Schmidt number $Sc = \mu_j / (\rho_j D)$ is based on the values of the viscosity and density at the jet exit, and can be written as

$$Sc = \frac{1}{S} \frac{W_{\text{N}_2}}{W_{\text{He}}} \frac{\mu_j}{\mu_{\text{He}}} Sc_{\text{He-N}_2}, \quad (1.11)$$

where $Sc_{\text{He-N}_2} = \mu_{\text{He}} / (\rho_{\text{He}} D)$ is the Schmidt number based on the fluid properties of pure helium and the binary diffusion coefficient D of helium into nitrogen. Note that, since D is only function of the pressure and temperature, it is a constant for the isothermal jet flow considered here, giving for atmospheric normal conditions $Sc_{\text{He-N}_2} = 1.69$.

To complete the formulation, the composition dependence $\mu(Y)$ of the viscosity needs to be specified. For this purpose, the law proposed by Hirschfelder *et al.* (1954),

$$\frac{\mu^*}{\mu_{\text{He}}} = \left(1 + 1.385 S_{\text{CHe-N}_2} \frac{W_{\text{He}}}{W_{\text{N}_2}} \frac{1-Y}{Y}\right)^{-1} + \left(\frac{\mu_{\text{He}}}{\mu_{\text{N}_2}} + 1.385 S_{\text{CHe-N}_2} \frac{Y}{1-Y}\right)^{-1}, \quad (1.12)$$

is used, with $\mu_{\text{He}}/\mu_{\text{N}_2} = 1.11$. In particular, at the jet exit, μ_j/μ_0 is determined by setting $Y = Y_j$ in (1.12). At any position in the jet, the viscosity μ , nondimensionalized with μ_j , is then given by

$$\mu = \left(\frac{\mu_j}{\mu_{\text{He}}}\right)^{-1} \left(\frac{\mu^*}{\mu_{\text{He}}}\right). \quad (1.13)$$

The numerical integration of the boundary-layer equations can be performed with a finite difference method that is described in appendix A.1. In figure 1.1 a sample velocity profile at a downstream position $x = 10^{-3}$ is shown for the hot jet with $S = 0.8$ for a nondimensional injector tube length $L_t = 0.04$.

1.3.2 Linear stability equations

The classical linear stability theory describes the development in space and time of infinitesimal perturbations around a basic flow $U(r; Re, S, \dots)$. This basic flow is a solution of the equations of motion of the problem, i.e. the Navier-Stokes equations for the variable-density jet under the low-Mach number approximation, coupled with appropriate boundary conditions. To nondimensionalize the stability problem, we use the same scales as in the description of the jet flow field hereabove, except for the axial coordinate x , which characteristic length now is the jet radius a , and for the time t , which is scaled with a/U_j . To allow for azimuthal disturbances in the stability analysis, we will use the coordinates (x, r, θ) in the formulation. The equations of motion then become

$$\frac{\partial \rho}{\partial t} + \nabla \cdot (\rho \mathbf{u}) = 0, \quad (1.14a)$$

$$\rho \left(\frac{\partial \mathbf{u}}{\partial t} + \mathbf{u} \cdot \nabla \mathbf{u} \right) = -\nabla p + \frac{1}{Re} \left\{ \nabla \cdot [\mu (\nabla \mathbf{u} + \nabla \mathbf{u}^T)] - \frac{2}{3} \nabla (\mu \nabla \cdot \mathbf{u}) \right\}, \quad (1.14b)$$

and either

$$\rho \left(\frac{\partial T}{\partial t} + \mathbf{u} \cdot \nabla T \right) = \frac{1}{Re Pr} \nabla \cdot (\kappa \nabla T), \quad (1.14c)$$

or

$$\rho \left(\frac{\partial Y}{\partial t} + \mathbf{u} \cdot \nabla Y \right) = \frac{1}{Re Sc} \nabla \cdot (\rho \nabla Y). \quad (1.14d)$$

Small perturbations around a basic steady parallel flow are then introduced by setting

$$\begin{aligned} \mathbf{u} &= U \mathbf{e}_x + \tilde{\mathbf{u}}, & p &= \tilde{p}, \\ \rho &= \bar{\rho} + \tilde{\rho}, & T &= \bar{T} + \tilde{T}, \\ \mu &= \bar{\mu} + \tilde{\mu}, & Y &= \bar{Y} + \tilde{Y}, \\ \kappa &= \bar{\kappa} + \tilde{\kappa}, \end{aligned}$$

where $(U, \bar{\rho}, \bar{\mu}, \dots)$ do not depend on the streamwise coordinate x , but may vary with a collection of control parameters such as the Reynolds number Re , the jet-to-ambient density ratio S , and the Prandtl or Schmidt numbers Pr or Sc . Substituting the disturbances in the equations of motions yields the following system of linear equations:

$$\frac{\partial \tilde{\rho}}{\partial t} + U \frac{\partial \tilde{\rho}}{\partial x} + \bar{\rho} \nabla \cdot \tilde{\mathbf{u}} + \tilde{\rho}' v = 0, \quad (1.15a)$$

$$\begin{aligned} \bar{\rho} \left(\frac{\partial \tilde{\mathbf{u}}}{\partial t} + U \frac{\partial \tilde{\mathbf{u}}}{\partial x} + U' v \mathbf{e}_x \right) &= -\nabla p + \frac{1}{Re} \left[\bar{\mu} \nabla^2 \tilde{\mathbf{u}} + \frac{1}{3} \bar{\mu} \nabla (\nabla \cdot \tilde{\mathbf{u}}) - \frac{2}{3} \bar{\mu}' (\nabla \cdot \tilde{\mathbf{u}}) \mathbf{e}_r \right. \\ &\quad \left. + \tilde{\mu}' (\nabla \tilde{\mathbf{u}} + \nabla \tilde{\mathbf{u}}^T) \cdot \mathbf{e}_r + \left(U' \tilde{\mu}' \mathbf{e}_x + U' \frac{\partial \tilde{\mu}}{\partial x} \mathbf{e}_r \right) + \left(U'' + \frac{U'}{r} \right) \mu \mathbf{e}_x \right], \end{aligned} \quad (1.15b)$$

and either

$$\bar{\rho} \left(\frac{\partial \tilde{T}}{\partial t} + U \frac{\partial \tilde{T}}{\partial x} + \tilde{T}' v \right) = \frac{1}{Re Pr} \left[\bar{\kappa} \nabla^2 \tilde{T} + \bar{\kappa}' \tilde{T}' + \tilde{T}' \kappa' + \left(\tilde{T}'' + \frac{\tilde{T}'}{r} \right) \kappa \right], \quad (1.15c)$$

or

$$\bar{\rho} \left(\frac{\partial \tilde{Y}}{\partial t} + U \frac{\partial \tilde{Y}}{\partial x} + \tilde{Y}' v \right) = \frac{1}{Re Sc} \left[\bar{\rho} \nabla^2 \tilde{Y} + \bar{\rho}' \tilde{Y}' + \tilde{Y}' \rho' + \left(\tilde{Y}'' + \frac{\tilde{Y}'}{r} \right) \rho \right], \quad (1.15d)$$

where the prime $'$ denotes differentiation with respect to r and ∇ is the dimensionless nabla operator. Note that the tildes on the perturbed variables have been omitted from here on.

The fluctuations of the basic flow can be decomposed in *normal modes* in the form of elementary instability waves

$$(\rho, T, \mu, u, v, w, p) = (\hat{\rho}, \hat{T}, \hat{\mu}, \hat{u}, i\hat{v}, \hat{w}, \hat{p}) e^{i(kx + m\theta - \omega t)}, \quad (1.16)$$

of complex streamwise wavenumber k , integer azimuthal wave number m and complex angular frequency ω . Substitution of these normal modes in equations (1.15a)–(1.15d) then yields a system of ordinary differential equations for the cross-stream perturbation distributions,

$$(kU - \omega)\hat{\rho} + k\bar{\rho}\hat{u} + \frac{(r\bar{\rho}\hat{v})'}{r} + \frac{m\bar{\rho}\hat{w}}{r} = 0, \quad (1.17a)$$

$$\begin{aligned} \bar{\mu}\hat{\nabla}_{\beta,m}^2\hat{u} - iReU'\bar{\rho}\hat{v} - iRek\hat{p} - \frac{\bar{\mu}}{3}k\left[k\hat{u} + \frac{(r\hat{v})'}{r} + \frac{m\hat{w}}{r}\right] \\ + \bar{\mu}'(\hat{u}' - k\hat{v}) + U'\bar{\mu}' + \frac{(rU')'\hat{\mu}}{r} = 0, \end{aligned} \quad (1.17b)$$

$$\begin{aligned} \bar{\mu}\left[\hat{\nabla}_{\beta,m}^2\hat{v} - \frac{(\hat{v} + 2m\hat{w})}{r^2}\right] + iRe\hat{p}' + \frac{\bar{\mu}}{3}\left[k\hat{u}' + \left(\frac{(r\hat{v})'}{r}\right)' + m\left(\frac{\hat{w}}{r}\right)'\right] \\ - \frac{2\bar{\mu}'}{3}\left[k\hat{u} + \frac{(r\hat{v})'}{r} + \frac{m\hat{w}}{r}\right] + 2\bar{\mu}'\hat{v}' + kU'\hat{\mu} = 0, \end{aligned} \quad (1.17c)$$

$$\begin{aligned} \bar{\mu}\left[\hat{\nabla}_{\beta,m}^2\hat{w} - \frac{(\hat{w} + 2m\hat{v})}{r^2}\right] - \frac{iRem\hat{p}}{r} - \frac{\bar{\mu}}{3}\frac{m}{r}\left[k\hat{u} + \frac{(r\hat{v})'}{r} + \frac{m\hat{w}}{r}\right] \\ + \bar{\mu}'\left[r\left(\frac{\hat{w}}{r}\right)' - \frac{m\hat{v}}{r}\right] = 0, \end{aligned} \quad (1.17d)$$

and either

$$\bar{\kappa}\hat{\nabla}_{\gamma,m}^2\hat{T} - iRePr\bar{\rho}\hat{T}'\hat{v} + \bar{\kappa}'\hat{T}' + \bar{T}'\hat{\kappa}' + \frac{(r\bar{T}')'\hat{\kappa}}{r} = 0, \quad (1.17e)$$

or

$$\bar{\rho}\hat{\nabla}_{\zeta,m}^2\hat{Y} - iReSc\bar{\rho}\hat{Y}'\hat{v} + \bar{\rho}'\hat{Y}' + \bar{Y}'\hat{\rho}' + \frac{(r\bar{Y}')'\hat{\rho}}{r} = 0, \quad (1.17f)$$

where the reduced Laplacian operator

$$\hat{\nabla}_{\phi,m}^2 = \frac{1}{r}\frac{d}{dr}\left(r\frac{d}{dr}\right) - \left(\phi^2 + \frac{m^2}{r^2}\right), \quad (1.18)$$

has been introduced for convenience. The quantity ϕ takes the values $\phi = \beta$, $\phi = \gamma$ and $\phi = \zeta$ in the momentum, energy and species equations, respectively, with

$$\beta = [k^2 + iRe(kU - \omega)\bar{\rho}/\bar{\mu}]^{1/2}, \quad (1.19a)$$

$$\gamma = [k^2 + iRePr(kU - \omega)\bar{\rho}/\bar{\kappa}]^{1/2}, \quad (1.19b)$$

$$\zeta = [k^2 + iReSc(kU - \omega)]^{1/2}, \quad (1.19c)$$

defined with a non-negative real part for definiteness.

The stability equations must be accompanied with suitable boundary conditions. In infinite or semi-infinite domains, all perturbations must vanish in the far field, yielding

$$(\hat{\rho}, \hat{T}, \hat{\mu}, \hat{\kappa}, \hat{u}, \hat{v}, \hat{w}, \hat{p}) \rightarrow 0 \quad \text{as } r \rightarrow \infty. \quad (1.20)$$

The boundary conditions at the centerline $r = 0$ depend on the symmetry of the problem. In axisymmetric flows, we have to impose a vanishing azimuthal dependence of the velocity vector as the axis $r = 0$ is approached (see Batchelor & Gill, 1962), i.e. $\lim_{r \rightarrow 0} \frac{\partial}{\partial \theta} (u \mathbf{e}_x + v \mathbf{e}_r + w \mathbf{e}_\theta) = 0$. This leads to boundary conditions at the axis that take the form

$$r = 0 : \begin{cases} \hat{v} = \hat{w} = \hat{u}' = 0 \text{ and } (\hat{\rho}, \hat{T}, \hat{\mu}, \hat{\kappa}, \hat{u}, \hat{p}) \text{ finite} & (m = 0), \\ (\hat{\rho}, \hat{T}, \hat{\mu}, \hat{\kappa}, \hat{u}, \hat{p}) = \hat{v} \pm \hat{w} = \hat{v}' = 0 & (m = \pm 1), \\ (\hat{\rho}, \hat{T}, \hat{\mu}, \hat{\kappa}, \hat{u}, \hat{v}, \hat{w}, \hat{p}) = 0 & (|m| > 1), \end{cases} \quad (1.21)$$

different for different azimuthal modes.

1.3.3 Local absolute/convective instability

Dispersion relation

In the previous section, we have seen that substitution of the perturbations in the equations of motion of the flow yields a system of ordinary differential equations for the cross-stream perturbation distributions. After imposing appropriate boundary conditions, these stability equations turn into an eigenvalue problem whereby eigenfunctions $(\hat{\rho}, \hat{T}, \hat{\mu}, \hat{\kappa}, \hat{u}, \hat{v}, \hat{w}, \hat{p})(r)$, from here on shortened as $\hat{\psi}(r)$, exist only if k and ω satisfy a dispersion relation

$$D[k, \omega; R]. \quad (1.22)$$

Here, R represents the collection of control parameters Re, Pr, S, \dots the base flow depends on. The dispersion relation $D[k, \omega; R]$ is the equivalent in spectral space of the differential operator $D[-i\partial/\partial x, i\partial/\partial t; R]$ in physical space, originating from the governing equations of motion, so that fluctuations $\psi(x, t)$ satisfy

$$D\left(-i\frac{\partial}{\partial x}, i\frac{\partial}{\partial t}; R\right)\psi(x, t) = 0. \quad (1.23)$$

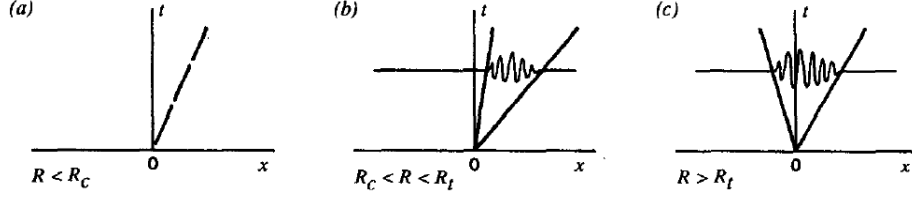


Figure 1.2: Typical impulse responses. (a) Stable, (b) Convectively unstable, (c) absolutely unstable. Figure taken from Huerre & Monkewitz (1990).

Linear instability

We introduce the Green's function $G(x, t)$ as the impulse response of the flow defined by

$$D\left(-i\frac{\partial}{\partial x}, i\frac{\partial}{\partial t}; R\right)G(x, t) = \delta(x)\delta(t), \quad (1.24)$$

where δ is the Diract delta function. The basic flow is then said to be *linearly stable* if

$$\lim_{t \rightarrow \infty} G(x, t) = 0 \quad \text{along all rays } x/t = \text{constant}, \quad (1.25)$$

and it is *linearly unstable* if

$$\lim_{t \rightarrow \infty} G(x, t) = \infty \quad \text{along at least one ray } x/t = \text{constant}. \quad (1.26)$$

In the latter case, we can further distinguish between a *linearly convectively unstable* flow, when its impulse response is ultimately advected away from the source so that

$$\lim_{t \rightarrow \infty} G(x, t) = 0 \quad \text{along the ray } x/t = 0, \quad (1.27)$$

and a *linearly absolutely unstable* flow, when the impulse response grows at the source and gradually contaminates the entire medium:

$$\lim_{t \rightarrow \infty} G(x, t) = \infty \quad \text{along the ray } x/t = 0. \quad (1.28)$$

Figure 1.2 illustrates the different scenarios explained above.

The distinction between absolute and convective instabilities seems to depend entirely on the selected frame of reference. However, it is precisely when Galilean invariance is broken, and the pertinent reference frame is unambiguously defined, that these notions acquire physical significance. This is the case for flows that are weakly spatially developing, or when the flow is continuously forced at a specific spatial location.

Temporal and spatial instability modes

Going back to spectral space, we can take up different approaches in solving the dispersion relation (1.22), mimicking the nature and dynamics of the instabilities that occur in different flows. When the complex frequency $\omega = \omega_r + i\omega_i$ is determined as a function of real wave number k , we talk about *temporal modes* $\omega(k; R)$. For involved basic flows, there will be an infinite but discrete number of solutions for each k . These freely evolving waves are spatially periodic disturbances of infinite extent which travel with phase velocity $c_r = \omega_r/k$ and grow or decrease in amplitude with a *temporal growth rate* ω_i . If there exists a real wavenumber k_a for which $\omega_i(k_a; R) > 0$, the basic flow is linearly unstable. On the contrary, when all temporal modes are damped, the flow is linearly stable. Temporal stability analysis is particularly useful to describe the *intrinsic* instabilities that appear in closed flows, as we implicitly assume that the flow evolves from some given initial state.

On the other hand, the instabilities in open shear flows display *extrinsic* dynamics, i.e. their spatial evolution is determined by the character—think frequency—of excitation. It is said that open shear flows act as *noise amplifiers*, and controlled experiments can characterize how the flow responds to different excitation frequencies. To model these instabilities, we consider them as a collection of spatially growing instability waves of different frequency. These *spatial branches* $k(\omega; R)$ can be obtained by solving the dispersion relation (1.22) for complex $k = k_r + ik_i$ given a real frequency ω .

Let us now examine how the temporal modes $\omega(k; R)$ and spatial mode $k(\omega; R)$ emerge from the general solution of (1.24). We can express the Green's function $G(x, t)$ as the Fourier superposition

$$G(x, t) = \frac{1}{(2\pi)^2} \int_{L_\omega} \int_{F_k} \frac{e^{i(kx - \omega t)}}{D[k, \omega; R]} dk d\omega, \quad (1.29)$$

where we have used that in Fourier space, equation (1.24) turns into the algebraic equation

$$D[k, \omega; R]G(k, \omega) = 1. \quad (1.30)$$

The integrations in (1.29) are performed along the path $F_k(L_\omega)$ in the complex k -plane (ω -plane). Such contours cannot be chosen arbitrarily since both the convergence of (1.29) as the *causality condition*, $G(x, t) = 0$ for $t \leq 0$, should be ensured. The solution $G(x, t)$ is assumed to be well-behaved when $x \rightarrow \pm\infty$, so that its Fourier transform

$$G(k, t) = \int_{-\infty}^{+\infty} G(x, t) e^{-ikx} dx \quad (1.31)$$

is properly defined in a strip of the complex k -plane including the real axis. In particular, we choose F_k to lie on the real k -axis. The contour L_ω is then taken as a straight

horizontal line located above all the singularities of the integrand. Note that the latter singularities are the zeros of the dispersion relation, and because of our choice of F_k on the real k -axis, they coincide with the *temporal modes* mentioned earlier. The chosen location of L_ω in the complex ω -plane guarantees that the integral

$$G(x, \omega) = \int_{-\infty}^{+\infty} G(x, t) e^{i\omega t} dt \quad (1.32)$$

is well-defined at $t = \infty$ since $e^{i\omega t}$ decays faster at $t = \infty$ than the temporal mode with the highest growth rate ω_i . We will denote this choice for the contour pair F_k and L_ω as C_0 .

Let us now evaluate the inverse Fourier transform with respect to ω

$$G(k, t) = \frac{1}{2\pi} \int_{L_\omega} \frac{e^{i(-\omega t)}}{D[k, \omega; R]} d\omega. \quad (1.33)$$

When $t < 0$, the L_ω contour can be closed at infinity by an upper semi-circle. Since the L_ω contour is located above all temporal branches, there are no residue contributions, so $G(k, t) = 0$ for $t < 0$ as required by the causality condition. When $t > 0$, the L_ω contour can be closed at infinity by a lower semi-circle. If poles are assumed to be all simple applying the residue theorem yields

$$G(k, t) = -i \sum_j \frac{e^{i(-\omega_j(k)t)}}{\frac{\partial D}{\partial \omega}[k, \omega_j(k); R]}, \quad (1.34)$$

where we sum over all temporal modes j . The explicit solution of the problem thus reads

$$G(x, t) = -\frac{i}{2\pi} \sum_j \frac{e^{i(kx - \omega_j(k)t)}}{\frac{\partial D}{\partial \omega}[k, \omega_j(k); R]} dk. \quad (1.35)$$

We can recognize a wave packet composed of freely evolving temporal modes generated by the impulse. Let us define the *maximum temporal growth rate* $\omega_{i,\max}$ as

$$\omega_{i,\max} = \max\{\omega_{j,i}(k) \text{ for all real } k \text{ and indices } j\}. \quad (1.36)$$

The temporal evolution of the impulse response $G(x, t)$, characterized by equation (1.35) provides the following *stability/instability* criterion.

- If $\omega_{i,\max} < 0$, the basic state is *linearly stable*, as all temporal modes possess a negative growth rate and the integrand decreases exponentially.
- If $\omega_{i,\max} > 0$, the basic state is *unstable*, since for some bandwidth of real wavenumbers k , a temporal branch $\omega_j(k)$ lies above the real axis in the complex ω -plane

and the integral for $G(x, t)$ blows up.

- If $\omega_{i,\max} = 0$, the basic state is *neutrally stable*, and a nonlinear study should be performed to determine the ultimate evolution of infinitesimal perturbations.

Spatiotemporal stability analysis

In the previous paragraphs, we have defined temporal and spatial modes, for real values of k and ω , respectively, i.e. for contours F_k and L_ω lying on the real axis in their respective complex plane. It was said that temporal stability analysis is typically performed in closed flows, while for open flows a spatial stability point of view is more appropriate. However, application of these concepts to other open flows such as bluff-body wakes and hot or low-density jets leads to the conclusion that local spatial theory in the strict sense (real frequency) is not sufficient. That is, these flows exhibit a transition in which their extrinsic dynamics as noise amplifiers change to an intrinsic dynamical behavior as oscillators. The evolution of vortices does not rely any more on the spatial amplification of external disturbances but rather on the growth of initial disturbances in time. To formally describe this transition from *convective* to *absolute* instability, we have to take on a *spatiotemporal* point of view. We start with introducing *generalized temporal (spatial) modes* as solutions of the dispersion relation $D[k, \omega; R]$ when the contour F_k (L_ω) differs from the real axis. There is no problem in deforming the initial contour pair C_0 introduced above as long as we avoid crossing the corresponding generalized temporal (spatial) modes. If L_ω stands above $\omega_{i,\max}$ in the complex ω -plane, as in the case of C_0 , the general spatial modes can be partitioned into two disconnected sets $k_j^+(\omega)$ and $k_j^-(\omega)$ located respectively above and below the real axis in the complex k -plane.

Let us now examine if the partition of generalized spatial branches into two disconnected sets $k_j^+(\omega)$ and $k_j^-(\omega)$ is preserved as the L_ω contour is gradually displaced downward from its C_0 location. This process is illustrated in figure 1.3. The initial configuration C_0 is depicted in figure 1.3(a). As long as the partition of $k_j^+(\omega)$ and $k_j^-(\omega)$ is preserved (figure 1.3(a) and (b)), it is possible to deform the F_k contour so that it separates the two sets of spatial branches, and causality remains enforced as result of the integration does not change. However, if the two sets $k_j^+(\omega)$ and $k_j^-(\omega)$ connect at a particular point k_0 , *pinching* of the F_k contour by two generalized spatial branches takes place. Further lowering of L_ω is then illegal as any additional deformation of F_k will cross a generalized spatial branch and violate causality.

If we denote ω_0 the value $\omega(k_0)$, we can distinguish two sub-classes according to the sign of $\omega_{0,i}$ at pinching. If $\omega_{0,i} < 0$, purely spatial branches associated with L_ω lying on the real axis *do have physical meaning*. To show this, we need to consider the signaling problem where, instead of the impulse response, we analyze the response of the flow to localized harmonic forcing $\delta(x)H(t)e^{i\omega_j t}$. The reader is referred to Huerre & Rossi

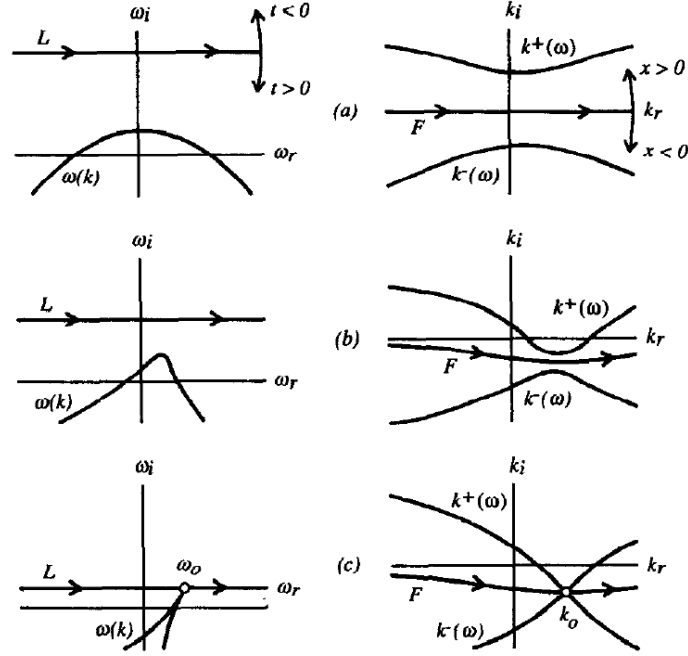


Figure 1.3: Loci of spatial branches $k^+(\omega)$ and $k^-(\omega)$ as the L -contour is displaced downward in the complex ω -plane. (a), (b), and (c) refer to different stages in the pinching process. (Figure taken from Huerre & Monkewitz (1990).)

(1998) for a detailed treatment of the signalling problem. Conversely, if $\omega_{0,i} > 0$, these same spatial branches cannot be continuously connected to their C_0 brethren, and the signalling problem will be shown to be ill-defined. The spatial branches are said to be *unphysical*. This is a first sign that there are flows for which a purely spatial stability analysis will not provide us with any physically relevant information. In what follows we will see that the distinction between the cases $\omega_{0,i} < 0$ and $\omega_{0,i} > 0$ or, in other words, flows for which spatial branches do or do not have physical meaning, can be related with the absolute/convective nature of the instability.

Asymptotic impulse response

Let us consider the asymptotic behavior of the impulse response $G(x, t)$ given by equation (1.35) at a fixed location x as $t \rightarrow \infty$. For simplicity, only one generalized temporal mode is considered. Let F_k be a pinched contour as sketched in figure 1.3(c). The *pinching point* k_0 is a double zero of the dispersion relation $D[k, \omega; R]$ at $\omega = \omega_0$, so

$$D[k_0, \omega_0; R] = 0 \quad \text{and} \quad \frac{\partial D}{\partial k}[k_0, \omega_0; R] = 0, \quad (1.37)$$

Consequently, $\partial\omega/\partial k(k_0) = 0$, so k_0 is also a *stationary point* of the function $\omega(k)$. More specifically, the point k_0 is a global maximum of the function $\omega_i(k)$ as k travels along F_k (see figure 1.3(c)). This feature can be exploited to evaluate $G(x, t)$ for large time by a *steepest descent method*. That is, in the limit $t \rightarrow \infty$, the integrand in equation (1.35) is controlled by the exponential factor $e^{\omega_i(k)t}$. To inspect the shape of the surface $\omega_i(k_r, k_i)$ the complex function $\omega(k)$ can be approximated by its Taylor expansion, and it can be shown (Huerre & Rossi, 1998, p. 135) that the local topology of $\omega_i(k)$ is that of a *saddle* as sketched in figure 1.4. The point k_0 is henceforth referred to as a *saddle point*. It can be seen that two important mutually orthogonal directions emerge from the saddle point k_0 , corresponding to the *steepest ascent path* and the *steepest descent path*. Selecting as a particular pinched contour in (1.35) the steepest descent path of the surface $\omega_i(k_r, k_i)$, one can determine the *asymptotic impulse response along the ray $x/t = 0$* as (Huerre & Rossi, 1998, p. 136)

$$G(x, t) \sim \frac{e^{i\pi/4}}{\sqrt{2\pi}} \frac{e^{i(k_0 x - \omega_0 t)}}{\frac{\partial D}{\partial \omega}[k_0, \omega_0; R] \left[t \frac{\partial^2 \omega}{\partial k^2}(k_0) \right]^{1/2}}. \quad (1.38)$$

In the laboratory frame, i.e. along the ray $x/t = 0$, the impulse response is dominated by the so-called complex *absolute wavenumber* k_0 and complex *absolute frequency* ω_0 of zero group velocity. The quantity $\omega_{0,i}$, commonly referred to as the *absolute growth rate*, characterizes the asymptotic growth of disturbances in the laboratory frame, and readily provides an *absolute/convective instability criterion*:

- If the basic state is unstable ($\omega_{i,\max} > 0$) and $\omega_{0,i} < 0$, the system eventually goes back to rest at any fixed point in the laboratory frame. A packet of unstable waves increases in amplitude but is washed downstream, so that at any fixed station, perturbations grow initially, but, as the tail of the wave packet passes by, ultimately decrease exponentially in amplitude. This is the situation sketched in figure 1.2(b). The instability is *convective*. We have seen before that in this case, spatial modes are pertinent to describe the response of the flow to external perturbations.
- If the basic state is unstable ($\omega_{i,\max} > 0$) and $\omega_{0,i} > 0$, perturbations exponentially increase in time at any fixed station in the laboratory frame. The instability is then said to be *absolute* (see figure 1.2(c)).

We can now extend this previous result to the case of a reference frame moving at a velocity v . We thus consider the *asymptotic impulse response along an arbitrary fixed spatiotemporal ray $x/t = v$* , as $t \rightarrow \infty$. Similar to the case of zero group velocity, one can

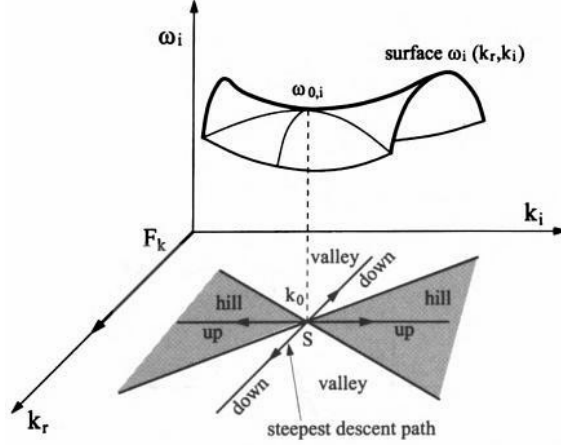


Figure 1.4: Local topology of surface $\omega_i(k_r, k_i)$ around a saddle point k_0 . Figure from Huerre & Rossi (1998).

obtain that pinching takes places at k_* and ω_* such that

$$\omega_* = \omega(k_*) \quad \text{and} \quad \frac{\partial \omega}{\partial k}(k_*) = v, \quad (1.39)$$

and that

$$G(x, t) \sim \frac{e^{i\pi/4}}{\sqrt{2\pi}} \frac{e^{i(k_*x - \omega_*t)}}{\frac{\partial D}{\partial \omega}[k_*, \omega_*; R] \left[t \frac{\partial^2 \omega}{\partial k^2}(k_*) \right]^{1/2}}. \quad (1.40)$$

Doppler-shifting the frequency ω , an observer moving at the velocity $x/t = v$ perceives a temporal growth rate $\sigma = \omega_{*,i} - k_{*,i}v$, which is by construction less than the maximum temporal growth rate $\omega_{i,\max}$. When $\sigma < 0$ ($\sigma > 0$), perturbations decay (increase) exponentially in time along the ray $x/t = v$. For a single wave packet, three particular ray velocities stand out, as can be seen in figure 1.5

- The real group velocity $v_{\max} = \partial \omega / \partial k(k_{\max})$ at the real wavenumber of highest temporal growth rate $\omega_{i,\max}$. For an observer moving along the ray $x/t = v_{\max}$, the wave packet amplitude is maximum.
- Two front velocities v_- and v_+ with $v_- < v_{\max} < v_+$ such that $\sigma = 0$. These velocities delineate two moving fronts in the $x - t$ plane within which the wave packet amplitude increases exponentially in time. Two distinct behaviors are then possible for the impulse response.
 - Whenever $v_- < 0 < v_+$ the system is *absolutely unstable* since the absolute growth rate $\omega_{0,i}$ observed along the ray $v_-x/t = 0 < v_+$ is necessarily positive. This case is illustrated in figure 1.5(a).

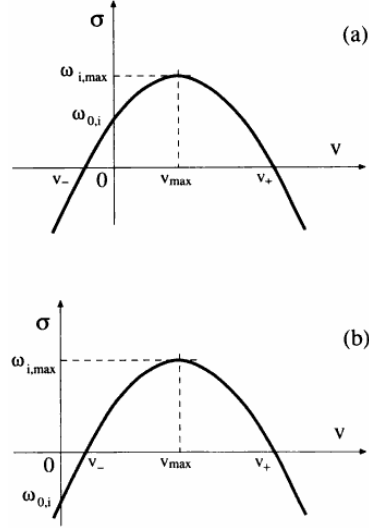


Figure 1.5: Temporal growth rate $\sigma = \omega_{*,i} - k_{*,i}v$ as a function of observer velocity $x/t = v$; (a) absolute instability, (b) convective instability. Figure from Huerre & Rossi (1998).

- In the opposite case where the front velocities are of the same sign (figure 1.5(b) the system is *convectively unstable*. At a fixed station $x/t = 0$, an observer first perceives a growing wave packet as the first front of velocity v_+ passes by. Once the second front of velocity v_- reaches the same location, the system returns to the rest state, dictated by the asymptotic decay rate $\omega_{0,i} < 0$.

1.3.4 Relation between local and global instability

In the previous section we introduced the concepts of absolute/convective instability for strictly parallel base flows. However, most open shear flows, such as the variable-density jets considered in this dissertation, are spatially developing, and the local stability characteristics are functions of the streamwise coordinate x . However, if the spatial development of the flow is slow compared to a typical instability wavelength, it can be shown (see Huerre & Monkewitz, 1990) that there exists a relationship between the global instability of the flow and the evolution of the local instability characteristics along the streamwise direction x . The spatial development of the basic flow can be characterised by a length scale L defined as

$$\frac{1}{L} \simeq \frac{1}{\theta} \frac{d\theta}{dx}, \quad (1.41)$$

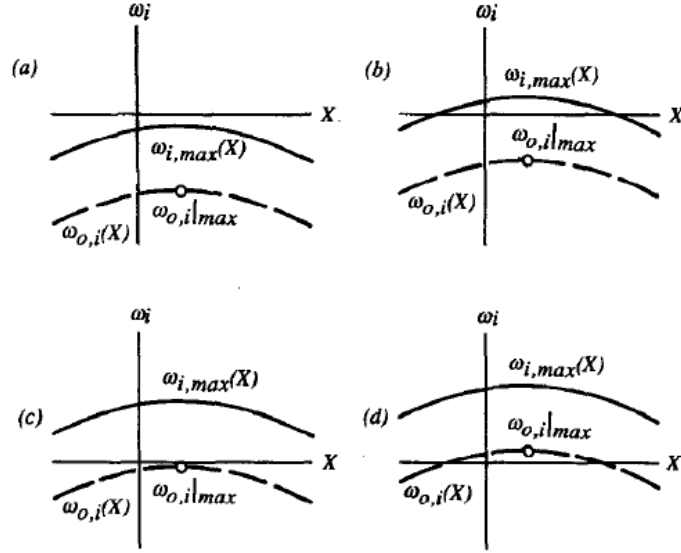


Figure 1.6: Classification of spatially developing flows according to the streamwise distribution of local instability. (a) uniformly locally stable; (b) locally convectively unstable; (c) almost absolutely unstable; (d) pocket of absolute instability. Figure from Huerre & Monkewitz (1990).

where θ is the local momentum or vorticity thickness. The connection between global and local instability then formally holds when

$$\frac{\lambda}{L} \ll 1, \quad (1.42)$$

where λ is a typical instability wavelength.

Based on the streamwise distribution of local instability, we can classify spatially developing shear flows into four broad categories, illustrated in figure 1.6. When $\omega_{i,\max}(x) < \omega_{0,i}(x) < 0$ for all x , the flow is said to be *uniformly locally stable* (figure 1.6(a)). If a region of local convective instability is present where $\omega_{i,\max} > 0$ but $\omega_{0,i} < 0$ (figure 1.6(b)), the flow is *locally convectively unstable*. These flows behave as noise amplifiers, but are “globally stable” in the sense that no self-sustained resonant states may arise. In the third category of flows, depicted in figure 1.6(c), the maximum absolute growth rate $\omega_{0,i}|_{\max} \lesssim 0$. These flows are *almost absolutely unstable* and may admit weakly damped global modes. Finally, when $\omega_{0,i}|_{\max} > 0$ in a *pocket of absolute instability*, the flow may exhibit self-excited global modes. They then are *globally unstable*.

With respect to the last category, it was found by Pier & Huerre (2001) that the fully nonlinear periodic regime of weakly non-parallel shear flows, having a pocket of local absolute instability away from boundaries, is controlled by the station at which the local

linear instability changes from convective to absolute (C/A transition), which acts as a wavemaker triggering the response of the entire flow. In addition, they found that this wavemaker determines the global frequency of the non-linear wake oscillations, which happens to be the real part of the absolute frequency at that distinguished point of the flow. The non-linear global mode structure found by Pier & Huerre (2001) is a sharp front located at the C/A transition station, which separates the convectively unstable region located upstream and the fully non-linear self-excited region downstream of the front, and is generally referred to as an *elephant global mode*.

References

- BATCHELOR, G. K. & GILL, A. E. 1962 Analysis of the stability of axisymmetric jets. *J. Fluid Mech.* **14**, 529–551.
- BROWN, G. L. & ROSHKO, A. 1974 On density effects and large structure in turbulent mixing layers. *J. Fluid Mech.* **64**, 775–816.
- CHOMAZ, J. M. 2005 Global instabilities in spatially developing flows: Non-normality and nonlinearity. *Ann. Rev. Fluid Mech.* **37**, 357–392.
- COENEN, W., SEVILLA, A. & SÁNCHEZ, A. 2008 Absolute instability of light jets emerging from circular injector tubes. *Phys. Fluids* **20**, 074104.
- COHEN, J. & WYGNANSKI, I. 1987 The evolution of instabilities in the axisymmetrical jet. Part 1. The linear growth of disturbances near the nozzle. *J. Fluid Mech.* **176**, 191–219.
- CROW, S. C. & CHAMPAGNE, F. H. 1971 Orderly structure in jet turbulence. *J. Fluid Mech.* **48**, 547–591.
- GASTER, M. 1962 A note on the relation between temporally increasing and spatially increasing disturbances in hydrodynamic stability. *J. Fluid Mech.* **14**, 222–224.
- GASTER, M. 1968 Growth of disturbances in both space and time. *Phys. Fluids* **11**, 723–727.
- HALLBERG, M. P., SRINIVASAN, V., GORSE, P. & STRYKOWSKI, P. J. 2007 Suppression of global modes in low-density axisymmetric jets using coflow. *Phys. Fluids* **19** (1), 014102.
- HALLBERG, M. P. & STRYKOWSKI, P. J. 2006 On the universality of global modes in low-density axisymmetric jets. *J. Fluid Mech.* **569**, 493–507.
- HELMHOLTZ, H. VON 1868 Über discontinuirliche Flüssigkeitsbewegungen. *Monats. Königl. Preuss. Akad. Wiss. Berlin* **23**, 215–228.

- HIRSCHFELDER, J. O., CURTISS, C. F & BIRD, R. B. 1954 *Molecular theory of gases and liquids*. J. Wiley, New York.
- HO, C.-M. & HUERRE, P. 1985 Perturbed free shear layers. *Annu. Rev. Fluid Mech.* **16**, 365–424.
- HOLMES, M. H. 2007 *Introduction to Numerical Methods in Differential Equations*. Springer, New York.
- HUERRE, P. 2000 Open shear flow instabilities. In *Perspectives in fluid dynamics* (ed. G. Batchelor, K. Moffatt & G. Worster), pp. 159–229. Cambridge.
- HUERRE, P. & MONKEWITZ, P. A. 1985 Absolute and convective instabilities in free shear layers. *J. Fluid Mech.* **159**, 151–168.
- HUERRE, P. & MONKEWITZ, P. A. 1990 Local and global instabilities in spatially developing flows. *Annu. Rev. Fluid Mech.* **22**, 473–537.
- HUERRE, P. & ROSSI, M. 1998 Hydrodynamic instabilities in open flows. In *Hydrodynamics and nonlinear instabilities* (ed. C. Godrèche & P. Manneville), pp. 81–294. Cambridge.
- JENDOUBI, S. & STRYKOWSKI, P. J. 1994 Absolute and convective instability of axisymmetric jets with external flow. *Phys. Fluids* **6**, 3000–3009.
- KAMBE, T. 1969 The stability of an axisymmetric jet with parabolic profile. *J. Phys. Soc. Jpn.* **26** (2), 566–575.
- KELVIN, LORD 1871 Hydrokinetic solutions and observations. *Phil Mag.* (4) **42**, 362–377.
- KUCHEMAN, D., CRABTREE, L. F. & SOWERBY, L. 1963 Three-dimensional boundary layers. In *Laminar Boundary Layers* (ed. L. Rosenhead), pp. 439–446. Oxford University Press.
- KYLE, D. M. & SREENIVASAN, K. R. 1993 The instability and breakdown of a round variable-density jet. *J. Fluid Mech.* **249**, 619–664.
- LANDAU, L. & LIFSCHITZ, E. M. 1954 *Mechanics of Continuous Media*. Moscow: Fizmatgiz (In Russian).
- LANDAU, L. & LIFSCHITZ, E. M. 1959 *Fluid Mechanics*. London: Pergamon.
- LECONTE, J. 1858 On the influence of musical sounds on the flame of a jet of coal-gas. *Phil. Mag.* **15**, 235–239.

- LESSEN, M. & SINGH, P. J. 1973 The stability of axisymmetric free shear layers. *J. Fluid Mech.* **60** (3), 433–457.
- LESSHAFFT, L. & HUERRE, P. 2007 Linear impulse response in hot round jets. *Phys. Fluids* **19** (2), 024102.
- LESSHAFFT, L., HUERRE, P. & SAGAUT, P. 2007 Frequency selection in globally unstable round jets. *Phys. Fluids* **19** (5), 054108.
- LESSHAFFT, L., HUERRE, P., SAGAUT, P. & TERRACOL, M. 2006 Nonlinear global modes in hot jets. *J. Fluid Mech.* **554**, 393–409.
- MATTINGLY, G. E. & CHANG, C. C. 1974 Unstable waves on an axisymmetric jet column. *J. Fluid Mech.* **65** (3), 541–560.
- MICHALKE, A. 1965 On spatially growing disturbances in an inviscid shear layer. *J. Fluid Mech.* **23**, 521–544.
- MICHALKE, A. 1970 A note on the spatial jet-instability of the compressible cylindrical vortex sheet. *DLR research rep.* pp. FB–70–51.
- MOLLENDORF, J. C. & GEBHART, B. 1973 An experimental and numerical study of the viscous stability of a round laminar vertical jet with and without thermal buoyancy for symmetric and asymmetric disturbances. *J. Fluid Mech.* **61** (2), 367–399.
- MONKEWITZ, P. A., BECHERT, D. W., BARSIKOW, B. & LEHMANN, B. 1990 Self-excited oscillations and mixing in a heated round jet. *J. Fluid Mech.* **213**, 611–639.
- MONKEWITZ, P. A. & SOHN, K. D. 1988 Absolute instability in hot jets. *AIAA J.* **28**, 911–916.
- MORRIS, P. J. 1976 The spatial viscous instability of axisymmetric jets. *J. Fluid Mech.* **77** (3), 511–529.
- NICHOLS, J. W., SCHMID, P. J. & RILEY, J. J. 2007 Self-sustained oscillations in variable-density round jets. *J. Fluid Mech.* **582**, 341–376.
- PIER, B. & HUERRE, P. 2001 Nonlinear self-sustained structures and fronts in spatially developing wake flows. *J. Fluid Mech.* **145**, 145–174.
- RAGHU, S. & MONKEWITZ, P. A. 1991 The bifurcation of a hot round jet to limit-cycle oscillations. *Phys. Fluids* **3** (4), 501–503.
- RAYLEIGH, LORD 1880 On the stability, or instability, of certain fluid motions. *Proc. London Math. Soc.* **11**, 57–70.

- REYNOLDS, A. J. 1962 Observations of a liquid-into-liquid jet. *J. Fluid Mech.* **14**, 552–556.
- SEVILLA, A., GORDILLO, J. M. & MARTÍNEZ-BAZÁN, C. 2002 The effect of the diameter ratio on the absolute and convective instability of free coflowing jets. *Phys. Fluids* **14**, 3028–3038.
- SREENIVASAN, K. R., RAGHU, S. & KYLE, D. 1989 Absolute instability in variable density round jets. *Exps. Fluids* **7**, 309–317.
- SRINIVASAN, K., HALLBERG, M. P. & STRYKOWSKI, P. J. 2010 Viscous linear stability of axisymmetric low-density jets: Parameters influencing absolute instability. *Phys. Fluids* **22**, 024103.
- STURROCK, P. A. 1958 Kinematics of growing waves. *Phys. Rev.* **112**, 1488–1503.
- TAM, C. K. W. 1971 Directional acoustic radiation from a supersonic jet generated by shear layer instability. *J. Fluid Mechanics* **46**, 757–768.
- THEOFILIS, V. 2003 Advances in global linear instability analysis of nonparallel and three-dimensional flows. *Prog. Aerosp. Sci.* **39**, 249.
- TWISS, Q. 1951a On bailey's theory of amplified circulating polarized waves in an ionized medium. *Phys. Rev.* **84**, 448–457.
- TWISS, Q. 1951b On oscillations in electron streams. *Proc. Phys. Soc. (London)* **B64**, 654–669.
- TWISS, Q. 1952 Propagation in electron-ion streams. *Phys. Rev.* **88**, 1392–1407.
- TYNDALL, J. 1867 On the action of sonorous vibrations on gaseous and liquid jets. *Phil. Mag.* **33**, 375–391.
- YU, M.-H. & MONKEWITZ, P. A. 1990 The effect of nonuniform density on the absolute instability of two-dimensional inertial wakes and jets. *Phys. Fluids A* **2**, 611–639.

Inviscid absolute instability of light jets emerging from circular injector tubes

This chapter is a slightly modified version of the article “Absolute instability of light jets emerging from circular injector tubes” by W. Coenen, A. Sevilla and A.L. Sánchez, published in the journal Physics of Fluids (Coenen et al., 2008).

In this chapter, we present a numerical study of the spatiotemporal, inviscid linear instability of light jets emerging from round tubes for values of the Reynolds number, $Re = \rho_j Q / (\pi a \mu_j) \gg 1$, where Q is the volumetric flow rate, ρ_j , μ_j are, respectively, the jet density and viscosity, and a is the injection tube radius. The analysis focuses on the influence of the injector length l_t on the stability characteristics of the resulting jet, whose base velocity profile at the exit is computed in terms of the dimensionless tube length $L_t = l_t / (Re a)$ by integrating the boundary-layer equations along the injector. Both axisymmetric ($m = 0$) and helical ($|m| = 1$) modes of instability are investigated for different values of the jet-to-ambient density ratio $S = \rho_j / \rho_\infty < 1$. For short tubes $L_t \ll 1$ the base velocity profile at the tube exit is uniform except in a thin surrounding boundary layer. Correspondingly, the stability analysis reproduces previous results of uniform velocity jets, according to which the jet becomes absolutely unstable to axisymmetric modes for a critical density ratio $S_c \simeq 0.66$, and to helical modes for $S_c \simeq 0.35$. For tubes of increasing length the analysis reveals that both modes exhibit absolutely unstable regions for all values of L_t and small enough values of the density ratio. In the case of the helical mode, we find that S_c increases monotonically with L_t , reaching its maximum value $S_c \simeq 0.5$ as the exit velocity approaches the Poiseuille profile for $L_t \gg 1$. Concerning the axisymmetric mode, its associated value of S_c achieves a maximum value $S_c \simeq 0.9$ for $L_t \simeq 0.04$ and then decreases to approach $S_c \simeq 0.7$ for $L_t \gg 1$. The absolute growth rates in this limiting case of near-Poiseuille jet profiles are however extremely small for $m = 0$, in agreement with the fact that axisymmetric disturbances of a jet with parabolic profile are neutrally stable. As a result, for $S < 0.5$ the

absolute growth rate of the helical mode becomes larger than that of the axisymmetric mode for sufficiently large values of L_t , suggesting that the helical mode may prevail in the instability development of very light jets issuing from long injectors.

2.1 Introduction

The stability properties of round jets have been studied extensively in the past due to their relevance in many applications. In their pioneering work, Batchelor & Gill (1962) studied the local inviscid stability properties of incompressible, constant-density circular jets. Jets with top-hat velocity profiles were found to be unstable to both axisymmetric and non-axisymmetric perturbations, whereas jets with velocity profiles with distributed vorticity—such as the parabolic Poiseuille profile and the far-field Schlichting solution—are only unstable to non-axisymmetric instability modes. In particular, the Schlichting solution was shown to be unstable only for the mode with azimuthal number $|m| = 1$, in qualitative agreement with early experimental observations by Reynolds (1962). The particular case of a jet with parabolic velocity profile with stagnant fluid outside was later studied in detail by Kambe (1969), who performed a temporal stability analysis for both inviscid and viscous disturbances, showing that viscous, temporal, axisymmetric ($m = 0$) modes are stable, and become neutrally stable in the limit of infinitely large Reynolds number $Re \rightarrow \infty$, in agreement with the inviscid theory. The analysis also revealed that there exists inviscid instability for all non-axisymmetric modes $m \neq 0$, which become neutrally stable only for infinitely large wave numbers $k \rightarrow \infty$, a behavior associated with the discontinuous derivative of the velocity profile at the edge of the jet. The effect of viscosity on the parallel, temporal stability of the far-field self-similar region of both jets and wakes was considered by Lessen & Singh (1973), while the investigation of the corresponding spatial stability is due to Mollendorf & Gebhart (1973), who also considered buoyancy effects. Also of interest is the work of Morris (1976), who studied the spatial viscous instability of a nozzle-generated jet by considering three different types of velocity profiles representing, respectively, the near field of the jet, an intermediate region, and the far-field self-similar flow. The neutral stability curves, which were computed for the three types of velocity profiles, show how the inviscid approach becomes a uniformly good approximation to the viscous results for increasing values of jet Reynolds number.

Jets with density smaller than the ambient value show distinguished stability features that were first noticed by Michalke (1970) when studying the inviscid stability of a compressible cylindrical vortex sheet. Michalke found that the spatial stability theory failed for the axisymmetric mode when the jet-to-ambient density ratio, S , became smaller than a certain critical value S_c . This failure is associated with a transition from

a convective to an absolute instability of the underlying parallel flow, as explained by Huerre & Monkewitz (1985), who computed the critical density ratio $S_c \simeq 0.66$ for the incompressible, inviscid vortex sheet. The effects of the Mach number and of the velocity ratio between the jet and an ambient co-flow on the value of S_c for inertia-dominated, high-Reynolds-number round jets discharging from nozzles were investigated by Monkewitz & Sohn (1988). In their study, they introduced a family of velocity and density profiles of presumed shape to model the downstream evolution of the jet from the initial top-hat profiles at the exit plane. The parameters defining the profiles, including the centerline-to-ambient velocity ratio, the dimensionless mixing-layer momentum thickness and the turbulent Prandtl number, were adjusted at each downstream location to fit experimental data available at the time for turbulent jets. The analysis revealed in particular that the critical density ratio decreases when either the Mach number or the co-flow velocity increases. For the zero-Mach-number jet in the absence of co-flow, they found a critical density ratio $S_c \simeq 0.72$ corresponding to the flow becoming locally absolutely unstable downstream from the jet exit at a distance given approximately by 0.8 times the nozzle radius, a prediction that was later verified experimentally by Monkewitz *et al.* (1990). The stability of light plane jets has also been investigated, (see for instance Yu & Monkewitz, 1990; Raynal *et al.*, 1996), showing a behavior in qualitative agreement with that of the round jet.

It is noteworthy that the plane mixing layer happens to be convectively unstable regardless of the value of the density ratio between the mixing streams. In this case, a minimum ambient counterflow is necessary for the flow to become absolutely unstable (see Huerre & Monkewitz, 1985; Pavithran & Redekopp, 1989; Strykowski & Niccum, 1991). The effect of ambient counterflow on the stability of round jets was considered by Jendoubi & Strykowski (1994), who identified the presence of two different instability modes in the jet instability problem. The first one, a columnar mode which scales with the jet diameter, corresponds to that considered by Monkewitz & Sohn (1988), while the other one scales with the thickness of the shear layer and can be identified with the one found by Pavithran & Redekopp (1989) for the plane case. The critical value of density ratio, S_c , is strongly affected by the presence of an external co-flowing or counterflowing stream (see Strykowski & Niccum, 1991; Jendoubi & Strykowski, 1994; Hallberg *et al.*, 2007), as well as by its cross-stream extent (Sevilla *et al.*, 2002).

The full linear impulse response of a round jet of hot gas has been recently studied by Lesshafft & Huerre (2007), yielding results in good agreement with both experimental (Monkewitz *et al.*, 1990; Kyle & Sreenivasan, 1993; Hallberg & Strykowski, 2006; Hallberg *et al.*, 2007) and numerical (Lesshafft *et al.*, 2006, 2007; Nichols *et al.*, 2007) studies. As in Monkewitz & Sohn (1988), presumed forms are introduced for the velocity and density profiles, which incorporate the shear-layer momentum thickness θ as a parameter to characterize the jet downstream evolution from the initial top-hat profiles. The

analysis, which includes both viscous and compressibility effects, shows that, depending on the value of the group velocity, Green's function associated with the jet is dominated by either the columnar mode from Monkewitz & Sohn (1988) or the shear-layer mode from Pavithran & Redekopp (1989). For low values of the group velocity the columnar mode becomes dominant, so that the absolute/convective (A/C) transition, which corresponds to modes with zero group velocity, is determined by this mode. The investigation performed by Lesshafft & Huerre (2007) also revealed that the key physical mechanism responsible for the appearance of absolute instability in low density jets is the action of the baroclinic torque.

The previous stability studies of light jets apply to configurations in which the velocity profile at the exit displays a top-hat shape, as occurs when the jet issues from a nozzle. The transition to absolute instability is then dominated by the axisymmetric mode ($m = 0$), in that non-axisymmetric modes ($m \neq 0$) become absolutely unstable for smaller values of the density ratio S , and exhibit absolute growth rates that are smaller than those of the $m = 0$ mode irrespective of the value of S . This is for instance the case for the inviscid axisymmetric vortex sheet (see Monkewitz & Sohn, 1988), for which the transition takes place at a critical density ratio $S_c \simeq 0.66$ for $m = 0$, while the transition value for the first azimuthal mode, $|m| = 1$, is $S_c \simeq 0.35$. The prevalence of the axisymmetric mode is also observed as the jet develops downstream, when the initially uniform jet is surrounded by a relatively thin shear layer. This was ascertained in previous stability analyses by Jendoubi & Strykowski (1994); Lesshafft & Huerre (2007), which employ a prescribed hyperbolic-tangent profile for the velocity near the jet exit, a sufficiently good approximation to the actual velocity profiles observed close to well-designed nozzles (see Cohen & Wagnanski, 1987). These analyses explored the variation of S_c with the shear-layer thickness θ , revealing that the axisymmetric mode always dominates for increasing values of θ and that, for large enough values of $\theta \gtrsim 0.17$ times the nozzle radius, the instability is convective for both $m = 0$ and $|m| = 1$ for $S > 0.1$. The existing experimental evidence of round jets discharging from short nozzles seems to confirm the dominance of the axisymmetric mode (see for instance Mattingly & Chang, 1974; Crighton & Gaster, 1976; Cohen & Wagnanski, 1987). Axisymmetric self-excitations were also found in the recent experimental work of Hallberg & Strykowski (2006), who employed injectors of various lengths to explore the effect of the momentum thickness θ on the global instability.

Clearly, the previous stability analyses of light jets do not apply to jets issuing from long injectors, when the velocity profile at the jet exit differs considerably from the top-hat shape. The objective of the present chapter is to ascertain the influence of the injector tube length on the absolute or convective character of the instability of light jets, using in the development numerical integrations of the spatiotemporal, inviscid linear stability problem. At this point, we would like to emphasize the limitations inherent to using

the concepts of absolute (A) and convective (C) instability to non-parallel flows, a topic which is still being intensively investigated. The A/C character of a linear instability is rigorously defined only in the case of strictly parallel flows, which unfortunately represent a very small fraction of the actual engineering flows. In the case of non-parallel flows, only the *global* linear stability analysis (see for instance Theofilis, 2003) can be rigorously applied in principle, leading to a huge increase in the computational complexity of the problem, together with a reduced physical transparency. For these reasons, a considerable effort has been devoted in the past to extend the concepts of A/C instability to the much more common situation of slowly-diverging, non-parallel shear flows, (see for instance the excellent reviews by Huerre & Monkewitz, 1990; Chomaz, 2005). As a result of these studies, it is now well known that relevant and useful information about the spatiotemporal evolution of slender flows can be deduced by considering the downstream coordinate as a parameter, and solving at each station the eigenvalue problem associated to the fictitious parallel shear flow corresponding to the local velocity profile, which is the approach we will follow in the present work. In particular, a clear link has been established between the onset of global oscillations in a non-parallel flow, generically referred to as *global modes*, and the existence of streamwise regions of local absolute instability in the underlying parallel flow. In section 2.4 we will provide a more detailed discussion, based on previous results, about the conclusions that may be extracted from our analysis with respect to the expected global behavior of the flow under study.

2.2 Formulation

We consider here a jet of density ρ_j and viscosity μ_j discharging with a flow rate Q from a circular injector tube of radius a and length l_i into an infinite atmosphere of a heavier fluid. The Reynolds number $Re = \rho_j U_j a / \mu_j \gg 1$ based on the average velocity $U_j = Q / (\pi a^2)$ is assumed to be moderately large, so that the corresponding steady solution is a jet flow of characteristic length $Rea \gg 1$, which is sketched in figure 2.1, where r and x denote the radial and axial coordinates scaled with their characteristic values a and Rea , respectively. The steady solution for this slender flow can be calculated with small relative errors of order Re^{-2} by integrating numerically the axisymmetric boundary layer equations, thereby leading to a Reynolds-number-independent description of the base flow whose local, inviscid, spatiotemporal stability is then studied. As can be seen below in Eq. (2.6), the resulting stability problem is a function of the local velocity and density profiles at each x location, $U(r)$ and $\rho(r)$, which are nondimensionalized with their characteristic values U_j and ρ_j . We investigate, in particular, the influence of the injector length on the stability of configurations with moderately long injectors

$l_t \sim Rea$, for which the velocity profile at the jet exit $U_e(r)$ differs significantly from the top-hat profile $U_e = 1$ analyzed previously by Monkewitz & Sohn (1988).

To determine $U_e(r)$ one needs to compute the axisymmetric laminar flow along the injector, which remains steady provided Re is smaller than a certain critical value. In the boundary-layer approximation, the problem reduces to that of integrating the continuity and momentum equations

$$\frac{\partial}{\partial x}(rU) + \frac{\partial}{\partial r}(rV) = 0, \quad (2.1)$$

and

$$U \frac{\partial U}{\partial x} + V \frac{\partial U}{\partial r} = -P_1 + \frac{1}{r} \frac{\partial}{\partial r} \left(r \frac{\partial U}{\partial r} \right), \quad (2.2)$$

with initial conditions $U = 1$ at $x = -L_t$, and boundary conditions $\partial U/\partial r = V = 0$ at $r = 0$ and $U = V = 0$ at $r = 1$ for $x > -L_t$. Here, V represents the radial velocity component scaled with its characteristic value $\mu_j/(\rho_j a)$ and $P_1(x)$ is a rescaled pressure gradient, to be determined at each x location along the injector as part of the computation. The method of lines (see for instance Holmes, 2007) was employed to integrate the problem numerically. To that end, the equations of motion were discretized in the radial direction r with a centered second-order scheme and then written as a system of ordinary differential equations in the axial direction x , that was integrated numerically with a fourth-order Runge-Kutta method. The integration was extended up to the jet exit $x = 0$, thereby providing the velocity at the outlet $U_e(r)$ as a function of $L_t = l_t/(Rea)$. Sample velocity profiles are shown in figure 2.1 for $L_t = (10^{-4}, 0.04, 0.2)$. As explained in Kucheman *et al.* (1963), for short injectors with $L_t \ll 1$, the velocity remains nearly uniform, except in the vicinity of the injector wall, where there exists a thin annular boundary layer of characteristic thickness $L_t^{1/2} a$. For longer injectors of rescaled length $L_t \sim O(1)$ viscous shear stresses act all across the tube, modifying the velocity profile $U_e(r)$, which approaches the parabolic Poiseuille profile $U_e(r) = 2(1 - r^2)$ for $L_t \gg 1$.

As previously mentioned, the boundary-layer approximation describes the velocity profile along the injector with relative errors of order Re^{-2} . At the injector rim, however, there exists a small non-slender region, of characteristic size $\delta \ll a$, where the boundary-layer equations fail to describe the flow, and must be replaced with the full Navier-Stokes equations. The value of δ is determined by the condition that the convective terms in the momentum equation, of order $\rho_j U_\delta^2/\delta$, become comparable to the viscous terms, of order $\mu_j U_\delta/\delta^2$, with U_δ representing the characteristic velocity in the Navier-Stokes region. The value of $U_\delta \sim A\delta$ depends on the velocity gradient at the wall, A , which is of order $A \sim U_j/a$ for $L_t \sim O(1)$, thereby yielding $\delta \sim Re^{-1/2} a$ for the characteristic size of the Navier-Stokes region. In gases, where the Prandtl and Schmidt

numbers are of order unity, molecular transport of species and energy is also significant in this region, thereby modifying the density profile at distances from the injector rim of order δ . In the case of a submerged liquid jet, on the other hand, the Schmidt number Sc is typically very large, and departures of the density from the jet value are restricted to a small region of characteristic size $Sc^{-1/2}\delta \ll \delta$. Note that the estimate for δ has to be modified for very short injectors, when the velocity found near the wall is of order $U_\delta \sim U_j$, promoting convection and limiting the failure of the boundary-layer approximation to a small Navier-Stokes region of size $\delta \sim Re^{-1}a$. In view of the above discussion, it is clear that in the limit $Re \gg 1$ considered here, the near-wall region where our boundary-layer description fails becomes asymptotically small, and its effect can be correspondingly neglected in the first approximation in the following development.

The description of the flow in the injector, which assumes constant-density motion, is applicable to liquids and also to gases, provided that the associated Mach number is small and heat conduction from the injector wall is negligible. The boundary-layer approximation therefore provides a universal description for $U_e(r)$ in terms of the single parameter $L_t = l_t/(Rea)$ that can be employed to describe the local stability character at the jet exit for both liquid and gas jets. On the other hand, the jet evolution downstream from the exit depends on the mixing of the jet with the ambient, which must be described with account taken of the variation with composition and temperature of the density and transport properties, yielding descriptions that are different for submerged liquid and gas jets. As an example, we give below the solution for a non-buoyant heated gas jet discharging at low Mach number into a cold ambient of the same gas, which involves the integration of the continuity, momentum and energy equations

$$\frac{\partial}{\partial x}(\rho r U) + \frac{\partial}{\partial r}(\rho r V) = 0, \quad (2.3)$$

$$\rho \left(U \frac{\partial U}{\partial x} + V \frac{\partial U}{\partial r} \right) = \frac{1}{r} \frac{\partial}{\partial r} \left(\mu r \frac{\partial U}{\partial r} \right), \quad (2.4)$$

$$\rho \left(U \frac{\partial T}{\partial x} + V \frac{\partial T}{\partial r} \right) = \frac{1}{Pr} \frac{1}{r} \frac{\partial}{\partial r} \left(\mu r \frac{\partial T}{\partial r} \right), \quad (2.5)$$

with initial conditions at $x = 0$ given by $U = U_e(r)$ and $T = 1$ for $r \leq 1$ and $U = 0$ and $T = S$ for $r > 1$, and with boundary conditions for $x > 0$ given by $\partial U/\partial r = V = \partial T/\partial r = 0$ at $r = 0$ and $U = T - S = 0$ as $r \rightarrow \infty$. The conservation equations are supplemented with the equation of state written in the quasi-isobaric approximation $\rho T = 1$ and the presumed power-law temperature dependence of the viscosity and thermal conductivity $\mu = T^{0.7}$. In the formulation, T and μ represent the temperature and viscosity scaled with the jet values, Pr denotes the constant Prandtl number, taken to be $Pr = 0.7$ in the computations, and $S = \rho_j/\rho_\infty$ is the jet-to-ambient density ratio. An implicit finite difference scheme, second-order accurate in x and in r , was used in the computations

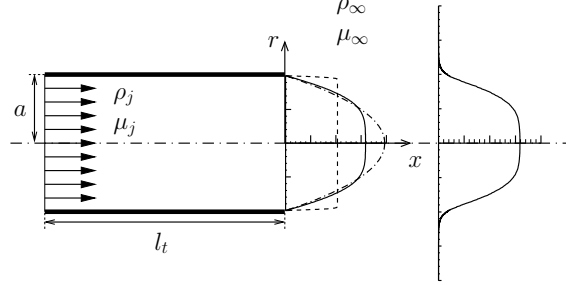


Figure 2.1: Sketch of the flow configuration considered in the present work. Numerical results for the velocity profiles at the jet exit for injector tube lengths $L_t = 10^{-4}$ (dashed line), $L_t = 0.04$ (solid line), and $L_t = 0.2$ (dot-dashed line), and the jet profile at a downstream position $x = 10^{-3}$ for $L_t = 0.04$ and $S = 0.8$.

of the velocity and density profiles $U(x, r)$ and $\rho(x, r)$ for $x > 0$. To ensure a correct calculation near the injector outlet, and in particular in the thin mixing layer that forms near the injector rim, grid points were clustered in the axial direction near $x = 0$, and in the radial direction around $r = 1$. This provided us with a minimum grid spacing $\delta x = 6 \times 10^{-6}$ at the jet outlet $x = 0$, and $\delta r = 1.5 \times 10^{-5}$ at the jet edge $r = 1$. The numerical code was validated, in the case $U_e(r) = 1$, by comparing the resulting velocity and density profiles with the self-similar solution by Chapman (1949) that appears for $x \ll 1$. A detailed description of the numerical method can be found in appendix A.1.

Following the standard procedure, the stability analysis introduces small perturbations to the steady axisymmetric base flow calculated previously. The perturbations are expressed as normal modes of complex axial wave number k , complex angular frequency ω , and integer azimuthal wave number m , yielding for instance $\hat{p} = P(r) \exp[i(k\bar{x} - \omega t + m\theta)]$ for the pressure perturbation, where k , ω , \bar{x} , and t are scaled with a^{-1} , U_j/a , a , and a/U_j , respectively. Linearizing about the base flow the mass, momentum, and energy conservation equations written in the low-Mach-number approximation, neglecting both viscous diffusion and heat conduction in the perturbation field, as corresponds to the limit $Re \rightarrow \infty$ with Pr of order unity, and substituting the normal modes indicated above, yields the eigenvalue problem

$$P'' + \left(\frac{1}{r} - \frac{2kU'}{kU - \omega} - \frac{\rho'}{\rho} \right) P' - \left(k^2 + \frac{m^2}{r^2} \right) P = 0, \quad P(0) \neq \infty, P(\infty) = 0 \quad (2.6)$$

for the pressure perturbation amplitude $P(r)$, where the prime $'$ denotes differentiation with respect to r . Notice that the above problem is the axisymmetric version of Eq. (A4) in Yu & Monkewitz (1990), which has also been recently used to investigate the stability of variable-density axisymmetric wakes by Sevilla & Martínez-Bazán (2006).

The eigenvalue problem (2.6) was solved with a shooting method which makes use of a Runge-Kutta-Fehlberg integration procedure, combined with a Newton-Raphson iterative scheme. In the shooting method, Eq. (2.6) was integrated outwards from a point near the axis, $r \ll 1$, and inwards from a point sufficiently far away from the axis, $r \gg 1$, where the velocity and density profiles are almost uniform. Both integrations were matched at an intermediate location, selected to be the inflection point of the velocity profile, by imposing that the value of P/P' be equal. The values of the pressure perturbation at the starting points were obtained using the solutions of Eq. (2.6) in the limit of uniform profiles. A more detailed discussion of the shooting technique applied to Eq. (2.6) can be found in Sevilla *et al.* (2002).

2.3 Linear instability of the jet flow

The local stability properties of the jet profiles at each downstream station can be obtained by studying the dispersion relation associated with (2.6). The local velocity and density profiles $U(r)$ and $\rho(r)$ depend on the axial position downstream from the injector exit, x , the density ratio, S , and the scaled injector length, $L_t = l_t/(Rea)$, and, thus, the dispersion relation takes the form

$$D(k, \omega; x, m, S, L_t) = 0. \quad (2.7)$$

Temporal modes are obtained by solving (2.7) for the complex frequency $\omega = \omega_r + i\omega_i = \omega(k; x, m, S, L_t)$ as a function of the real wave number k . The local flow is linearly unstable if and only if $\omega_i > 0$ for some real k , which is always the case here except in the limit $L_t \rightarrow \infty$, for which the jet velocity and density profiles at $x = 0$ become $U = 2(1 - r^2)$, $0 \leq r \leq 1$; $U = 0$, $r \geq 1$ and $\rho = 1$, $0 \leq r \leq 1$; $\rho = S^{-1}$, $r \geq 1$. This particular case of developed flow is found to be neutrally stable, as can be shown by straightforward extension of the necessary condition for instability of jet flows of uniform density, derived by Batchelor & Gill (1962), to jet flows with arbitrary density profiles. Spatial instability modes can be obtained by solving the dispersion relation (2.7) for the complex wave number $k = k_r + ik_i = k(\omega; x, m, S, L_t)$ as a function of the real frequency, ω , yielding spatially unstable flows if $k_i < 0$ for some real ω . For unforced open flows, spatial modes are known to give better agreement with experiments than temporal ones. Moreover, they provide the linear response of the flow to forcing, a result that is meaningful only for convectively unstable flows, which behave as amplifiers of upstream perturbations. On the contrary, absolutely unstable flows develop intrinsic behavior and generally give rise to markedly periodic dynamics in the fully non-linear regime (see Huerre, 2000). To determine the A/C character of the local instability, the physical modes with zero group velocity, i.e., such that $d\omega/dk = 0$, must be found,

along with their growth rate, $\omega_i^{(0)}$. This last quantity, usually called absolute growth rate, takes a maximum value that determines whether the local instability is absolute, $\omega_i^{(0)} > 0$, or convective, $\omega_i^{(0)} < 0$. Notice that the condition $d\omega/dk = 0$ is equivalent to the existence of a double root, or saddle point, of the dispersion relation in the complex k -plane, $\partial D/\partial k = 0$. In realistic dispersion relations there are usually many saddle points, but it is the one with the largest value of ω_i which determines the large-time impulse response of the flow, and, in particular, the convective or absolute nature of the local instability. To be physically meaningful, the saddle point must also satisfy the so-called *Briggs-Bers criterion* (see Briggs, 1964; Bers, 1975; Huerre, 2000), which implies that the two branches of the dispersion relation interacting in the double root must be located in opposite halves of the complex k -plane when $\omega_i > \omega_{i_{\max}}$, where $\omega_{i_{\max}}$ is the maximum temporal growth rate given by the temporal instability analysis.

Figure 2.2 shows the spatial branches of the dispersion relation, i.e. curves of constant ω_i in the complex wave number plane, corresponding to the first two modes $m = (0, \pm 1)$ for a density ratio $S = 0.8$, and two different tube lengths $L_t = 0.04$ and $L_t = 0.2$, at a small distance $x = 10^{-5}$ downstream from the injector outlet. Although, for clarity, only the region $1 \leq k_r \leq 10$, $-10 \leq k_i \leq 0$ of the plane is shown, it will be seen that all of the relevant information of the dispersion relation can be obtained within this region. Each spatial branch represents the solution of (2.7) for increasing values of ω_r at a fixed value of ω_i . A given spatial branch is classified as a *downstream* (k^+) or an *upstream* (k^-) branch, depending on its location in the complex k -plane when $\omega_i > \omega_{i_{\max}}$: downstream (resp. upstream) branches are those entirely located within the $k_i > 0$ (resp. $k_i < 0$) half-plane.

In the particular flow under study here there is only one k^+ branch, represented in each plot of figure 2.2 with a thick solid line for the particular case with $\omega_i = 0$, as well as an infinite sequence k_n^- , $n = 1, 2, \dots$ of upstream branches for increasing values of $-k_i$. In particular, several isolines of ω_i are represented in figure 2.2 for the first three upstream branches. As discussed above, the absolute/convective nature of the local instability can be established by studying the double roots, or saddle points, of the dispersion relation in the complex k -plane. These double roots result from the interaction of two simple roots, which are precisely the spatial branches defined above. Consequently, the Briggs-Bers criterion states that only those double roots which result from the coalescence of a k^+ and a k^- branch contribute to the linear impulse response of the flow.

Each of the complex wave number planes in figure 2.2 shows the presence of three saddle points, denoted by numbers 1 to 3, which are the beginning of an infinite sequence of double roots that emerge for increasing values of $-k_i > 10$. However, only the first double root, SP1, is seen to satisfy the Briggs-Bers criterion, since it is the only one which involves the k^+ branch of the dispersion relation. This can be concluded from

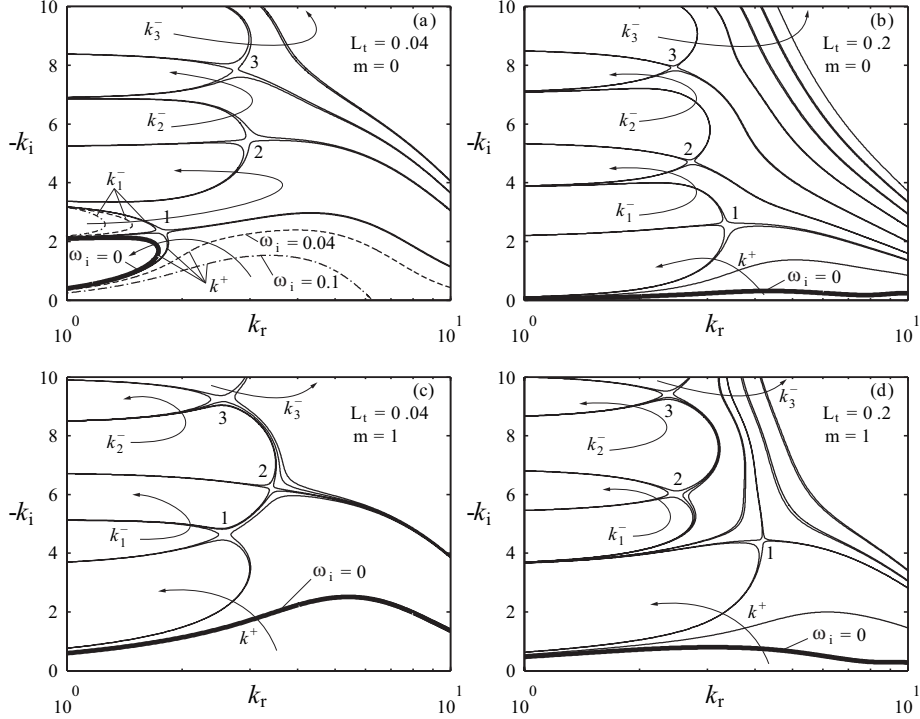


Figure 2.2: Structure of the complex k -plane for a density ratio $S = 0.8$ and scaled tube lengths $L_t = 0.04$ (left column) and $L_t = 0.2$ (right column), calculated at a small distance $x = 10^{-5}$ downstream from the jet outlet. Top and bottom rows correspond to axisymmetric, $m = 0$, and first azimuthal, $|m| = 1$, instability modes, respectively. The arrows indicate the displacement of the spatial branches as ω_i decreases. The dashed and dot-dashed lines in figure (a) represent, respectively, the isovalues $\omega_i = 0.04$ and $\omega_i = 0.1$ of the spatial branches k^+ and k_1^- which interact at the saddle point SP1.

figure 2.2 by carefully checking the path followed by the k^+ branch as ω_i decreases. Focusing on the particular case of figure 2.2(a), for which $L_t = 0.04$ and $m = 0$, notice from the first isoline of k^+ , $\omega_i = 0.1$ (dot-dashed curve), that this branch has partially emerged into the $k_i < 0$ half-plane since $\omega_i < \omega_{i_{\max}}$. Notice also, from figure 2.2(a), that the k_1^- branch corresponding to the same value of $\omega_i = 0.1$ is entirely contained in the $k_i < 0$ half-plane. For a lower value $\omega_i = 0.04$, the k^+ and k_1^- branches approach each other, as indicated with the arrows, eventually coalescing for a particular value of $\omega_i = \omega_i^{(0)} \simeq 0.01$, which is, thus, the *absolute growth rate* for the particular combination of parameters corresponding to figure 2.2(a). Moreover, since $\omega_i^{(0)} > 0$, it can be concluded that the parallel flow associated to the parameter values of figure 2.2(a) is absolutely unstable or, more concisely expressed, that the flow is *locally absolutely un-*

stable at the downstream station $x = 10^{-5}$. The character of the *local* linear instability in the case of figure 2.2(b)-(d) can be obtained by performing a similar analysis, which shows, in particular, that the interaction of the k^+ and the k_1^- branches takes place for a value of $\omega_i^{(0)} < 0$ in these three cases. Consequently, the $|m| = 1$ mode for an injector of length $L_t = 0.04$, as well as both the axisymmetric and helical modes when $L_t = 0.2$, are all *locally convectively unstable* at the station $x = 10^{-5}$.

A similar study for the remaining saddle points, i.e., SP2, SP3 and those located for $-k_i > 10$, immediately discards them as spurious, since they result from the interaction of two k^- branches, as can be seen by carefully following the evolution of the involved branches in the complex k -plane. We therefore conclude that SP1 is the only saddle point of interest, and, in what follows, its behavior will be studied by varying the parameters L_t , S , and x for $m = 0$ and $|m| = 1$.

For given values of L_t , S and m , varying the axial position x in the jet flow field was seen to change the complex k -plane, and in particular the locations of the saddle points, in a continuous manner. In order to determine the critical conditions for the appearance of local absolute instability in the jet, which is the main objective of the present work, it is necessary to compute the axial evolution of the absolute growth rate $\omega_i^{(0)}(x)$ associated with the most unstable local mode of zero group velocity, corresponding to SP1 in figure 2.2. The results of the analysis, as well as the evolution of the *local* Strouhal number based on the injector diameter, defined at each downstream position as $St^{(0)}(x) = \omega_r(x)/\pi$, are shown in figure 2.3 for $m = 0$ and for two illustrative values of the injector tube length, $L_t = 10^{-4}$ and $L_t = 0.04$, corresponding to very short and moderately long injector tubes, respectively. Three different values of the density ratio are considered in each case, including subcritical, nearly critical, and supercritical values of S .

In all cases, $\omega_i^{(0)}$ and $St^{(0)}$ are seen to approach finite values as $x \rightarrow 0$, corresponding to the flow at the jet exit, where the profiles of velocity and density are given by

$$\begin{cases} 0 < r < 1: & U = U_e(r), \rho = S \\ r > 1: & U = 0, \rho = 1. \end{cases} \quad (2.8)$$

The stability problem admits in this particular case the simplified form

$$P'' + \left(\frac{1}{r} - \frac{2kU'_e}{kU_e - \omega} \right) P' - \left(k^2 + \frac{m^2}{r^2} \right) P = 0, \quad P(0) \neq \infty, \quad P'(1) = S P(1) kK'_m(k)/K_m(k), \quad (2.9)$$

as follows from neglecting in (2.6) the derivative of the density and replacing the boundary condition as $r \rightarrow \infty$ with the condition $P' = P S kK'_m(k)/K_m(k)$ at the injector rim. This last equation is derived with use made of the analytical solution $P = CK_m(kr)$ for $r > 1$, where C is an arbitrary constant, together with the kinematical condition that the

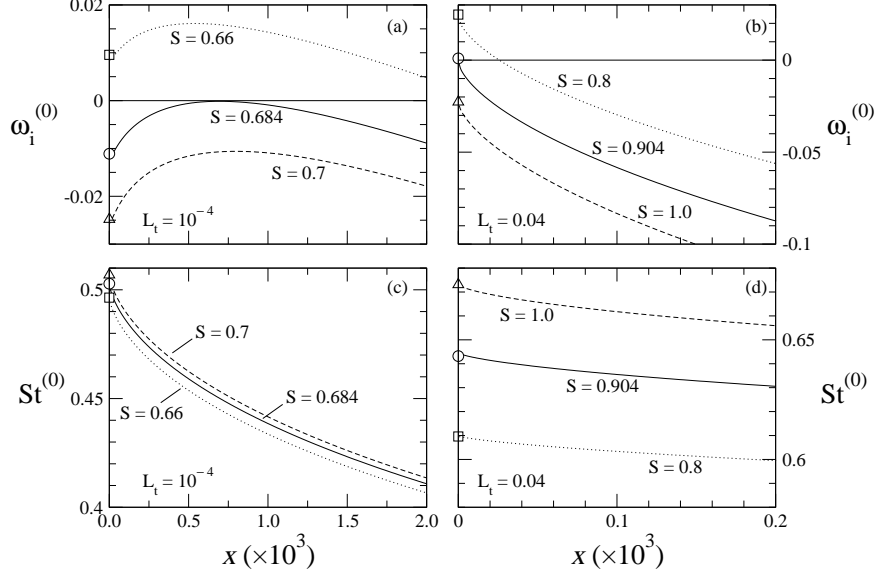


Figure 2.3: Spatiotemporal analysis for saddle point SP1 along the jet for the axisymmetric mode, $m = 0$. Top and bottom rows correspond to the absolute growth rate $\omega_1^{(0)}$ and the Strouhal number $St^{(0)}$, respectively. Left and right columns represent $L_t = 10^{-4}$ and $L_t = 0.04$, respectively. Symbols are the corresponding solutions of the stability problem (2.9) at the injector outlet $x = 0$.

boundary is a material surface and the dynamical condition that the pressure is continuous across the boundary. Here, K_m represents the m -th order modified Bessel function of the second kind. As expected, the solutions of this modified eigenvalue problem, plotted in figure 2.3 as symbols at $x = 0$, match with the solutions obtained from (2.6) as $x \rightarrow 0$.

As seen in figure 2.3, for the different cases considered the Strouhal number achieves values of order unity that decay with the downstream distance, and, for $L_t = 10^{-4}$, are consistent with previous experimental observations of light jets issuing from nozzles by Kyle & Sreenivasan (1993). The downstream evolution of $\omega_1^{(0)}$ is seen to be qualitatively different for the two injector lengths considered. Thus, for $L_t = 10^{-4}$ the curves of absolute growth rate have positive slopes at the jet exit $x = 0$, reaching their maximum values at a certain intermediate location, and then decreasing farther downstream. This non-monotonic behavior is directly related to previous investigations on jet stability by Monkewitz & Sohn (1988); Jendoubi & Strykowski (1994); Lesshafft & Huerre (2007), which revealed that for quasi-top-hat velocity profiles the flow is most unstable when the shear layer momentum thickness reaches a given non-zero value that is much smaller than the jet radius. The evolution is different for $L_t = 0.04$, when the absolute growth

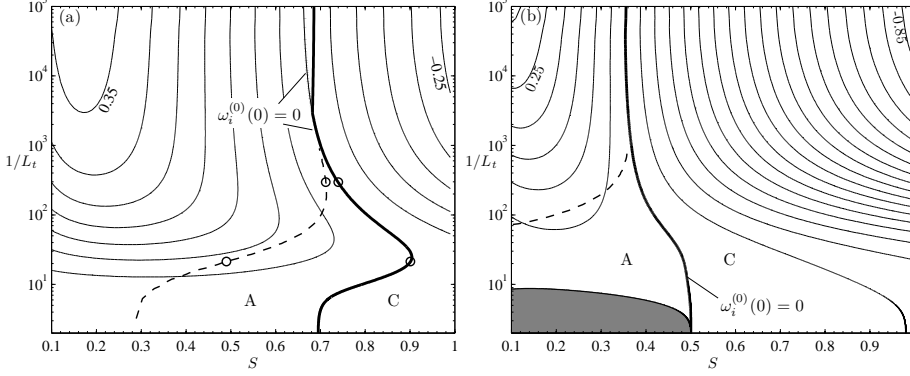


Figure 2.4: Curves of constant absolute growth rate $\omega_i^{(0)}(0)$ in the $S-L_t^{-1}$ parameter plane for axisymmetric (a) and helical (b) modes, with the isolines corresponding to incremental values of $\omega_i^{(0)}(0)$ equal to 0.05. The thick lines represent the transition curve between convective (C) and absolute (A) instabilities. The shaded region in (b) represents the region where helical modes are dominant. The dashed line represents the value of S_c obtained by Lesshafft & Huerre (2007) with the profiles given by Eq. (2.11), where the value θ/a is related to L_t through figure 2.5. The circles in (a) denote the conditions compared in the insets of figure 2.5.

rate decreases monotonically from its value at the jet exit. The computations determined the limiting injector length $L_t \simeq 3.5 \times 10^{-4}$ that separates both distinct behaviors, i.e., at which $d\omega_i^{(0)}/dx = 0$ at $x = 0$.

The two different behaviors identified above have implications regarding the computation of the critical density ratio S_c . Since the existence of a region of absolute instability is determined by the sign of $\omega_i^{(0)}$ at its maximum value, for injectors with $L_t \gtrsim 3.5 \times 10^{-4}$ the condition $\omega_i^{(0)} = 0$ at the jet exit $x = 0$ suffices to determine the corresponding critical value of S , in a computation that involves the integration of the simplified eigenvalue problem (2.9). For short injectors such that $L_t \lesssim 3.5 \times 10^{-4}$ the computation of S_c is more involved, in that one needs to determine the intermediate location at which $\omega_i^{(0)}$ reaches its local maximum. In this respect, it is worth mentioning that the variation with x of the absolute growth rate for the helical instability mode $|m| = 1$, not shown in the plots, exhibits a negative slope at the injector outlet regardless of the value of L_t , giving a downstream evolution similar to that of figure 2.3(b). Consequently, the existence of a region of instability for $|m| = 1$ is thus entirely determined by the value $\omega_i^{(0)}(0)$ of $\omega_i^{(0)}$ at $x = 0$, which can be computed from the integration of (2.9).

With the above results in mind, the absolute growth rate of SPI was calculated at the jet injector outlet by solving (2.9) for both the axisymmetric and the helical mode for different values of the injector tube length L_t and density ratio S . The parametric dependence of the results is shown in figure 2.4 in the form of isolines of constant

$\omega_i^{(0)}(0)$. The figure also displays as thick lines the *transition curves*, that is, the value of the critical density ratio S_c at which the flow changes from being convectively unstable throughout the jet (region C), to supporting a finite region of absolute instability (region A), for each value of the injector length L_t . As previously explained, for the helical mode the maximum value of $\omega_i^{(0)}$ is always found at the jet exit, and the isoline $\omega_i^{(0)}(0) = 0$ provides the A/C transition curve for all values of L_t . For the axisymmetric mode, however, the condition $\omega_i^{(0)}(0) = 0$ determines the A/C transition only for tubes with $L_t \gtrsim 3.5 \times 10^{-4}$, when the maximum value of $\omega_i^{(0)}$ is found at the jet exit. For shorter tubes, the most unstable jet position is located at a certain distance downstream from the injector outlet, as shown in figure 2.3(a), and the full, x -dependent, stability problem (2.6) needs to be solved, leading to values of S_c that are slightly larger than those found with the condition $\omega_i^{(0)}(0) = 0$. As a result, the A/C transition curve in figure 2.4(a), which coincides with the isoline $\omega_i^{(0)}(0) = 0$ for $L_t \gtrsim 3.5 \times 10^{-4}$, is shifted towards higher values of S for $L_t \lesssim 3.5 \times 10^{-4}$.

As seen in figure 2.4, the critical curves for A/C transition indicate that, for a given value of L_t , there always exist critical values of S below which the jet shows a region where the flow is absolutely unstable for both the axisymmetric and helical modes. The value of S_c for $|m| = 1$ increases monotonically for increasing values of L_t to reach $S_c \simeq 0.5$ as $L_t \rightarrow \infty$. For the axisymmetric mode, on the other hand, S_c reaches a maximum value $S_c \simeq 0.9$ for $L_t \simeq 0.04$, and then decreases for increasing tube lengths to reach $S_c \simeq 0.7$ as $L_t \rightarrow \infty$. This peak critical density ratio corresponds to a velocity profile at the jet exit, shown in figure 2.1, that, although not fully developed, differs considerably from a top-hat profile.

In the limit of short injector tubes, $L_t \rightarrow 0$, the isolines $\omega_i^{(0)}(0) = 0$ tend to $S \simeq 0.66$ and $S \simeq 0.35$ for $m = 0$ and $|m| = 1$, respectively, thereby reproducing the values computed for an incompressible vortex sheet by Monkewitz & Sohn (1988). For the case of a spreading jet starting from a top-hat profile $L_t = 0$, the absolute/convective transition in our calculations is found to first arise for $m = 0$ at a critical density ratio $S_c = 0.686$, at a downstream location $x \simeq 8 \times 10^{-4}$. This value of S_c for $L_t \rightarrow 0$ is somewhat lower than the value 0.72 given by Monkewitz & Sohn (1988) for their class of base flow profiles.

For sufficiently long injectors, we have seen that the stability analysis of the flow at the jet exit given in (2.9) suffices to determine the critical condition for existence of a region of absolute instability, so that the isoline $\omega_i^{(0)}(0) = 0$ in figure 2.4 provides the critical value S_c for $L_t \gtrsim 3.5 \times 10^{-4}$. Since the density profile always shows the top-hat shape given in (2.8) regardless of the value of L_t , the significant variations of S_c with L_t , found even for small values of $L_t \ll 1$, are attributable to changes in shape of the velocity profile at the jet exit. One may characterize this shape by giving its momentum

thickness

$$\frac{\theta}{a} = \int_0^\infty \frac{U}{U_a} \left(1 - \frac{U}{U_a}\right) dr, \quad (2.10)$$

where U_a is the value of the velocity at the jet axis. The resulting variation of θ/a with L_t is given in figure 2.5. For $L_t \ll 1$, the velocity profile at the jet exit is nearly uniform, except for a thin Blasius boundary layer located at the the injector rim (see Kucheman *et al.*, 1963), thereby giving $\theta/a = 0.6641L_t^{1/2}$. For increasing L_t , the value of θ/a increases to finally approach for $L_t \rightarrow \infty$ the asymptotic value $\theta/a = 1/7.5$ corresponding to the Poiseuille velocity profile.

The momentum thickness has been the preferred parameter in defining model profiles of density and velocity in previous stability analyses. For instance, Lesshafft & Huerre (2007) employ as base profiles

$$U = \frac{\rho^{-1} - S}{1 - S} = \frac{1}{2} + \frac{1}{2} \tanh \left[\frac{1}{4} \frac{a}{\theta} \left(\frac{1}{r} - r \right) \right] \quad (2.11)$$

where \tanh denotes the hyperbolic tangent function. Although the velocity profile in (2.11) has a large potential core surrounded by a thin viscous layer of momentum thickness $\theta/a \ll 1$, as occurs with $U_e(r)$ when $L_t \ll 1$, the resulting values of S_c differ significantly. To illustrate this, we have included in figure 2.4 the predictions given in figure 6 of Lesshafft & Huerre (2007) for $m = 0$ and $|m| = 1$. In representing their results, we have used the plot in figure 2.5 to relate L_t with θ/a , thereby ensuring that the comparisons are made for velocity profiles with equal momentum thickness. As can be seen, noticeable departures arise already for $L_t^{-1} \lesssim 5 \times 10^2$, corresponding to $a/\theta = 37.9$, as the value of S_c predicted with model base profiles begins to decrease with increasing L_t , while that computed with U_e continues increasing. For instance, for $L_t^{-1} = 296.24$ ($a/\theta = 30$), the value computed with U_e is $S_c = 0.740$ and the model profiles for $a/\theta = 30$ predict $S_c = 0.712$. These two points are identified by circles in figure 2.4, and the shapes of the two profiles are compared in an inset of figure 2.5, which also includes a second inset with the profiles with $a/\theta = 10$, corresponding to a longer injector of length $L_t^{-1} = 21.374$. For this second sample case the differences in shape are substantial, as are also the corresponding values of S_c shown in figure 2.4 ($S_c = 0.490$ and $S_c = 0.901$, respectively). Note that these large differences in S_c are due not only to differences in the shape of the base velocity profiles but also to differences in density, i.e., while the density profile used by Lesshafft & Huerre (2007) is related to the velocity through $U = (\rho^{-1} - S)/(1 - S)$, at the end of the injector one finds the top-hat profile given in (2.8) regardless of the injector length. Clearly, the detailed shape of the base profiles of density and velocity has a non-negligible effect on the resulting stability response and must be correspondingly accounted for in computations if accuracy is desired.

The decrease in S_c associated with the model base profiles is in agreement with the

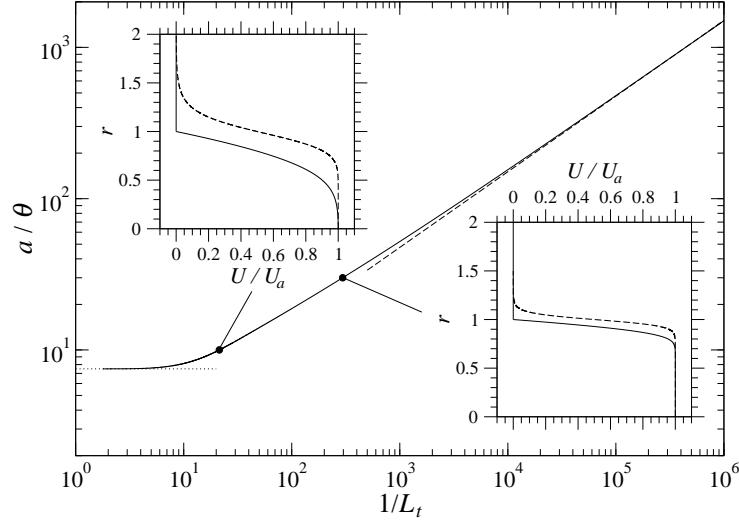


Figure 2.5: The variation of a/θ with L_t^{-1} as computed from (2.10) for the velocity profile at the jet exit (2.8) including the asymptotic behaviors $a/\theta = (0.6641L_t^{1/2})^{-1}$ for $L_t \ll 1$ (dashed line) and $a/\theta = 7.5$ for $L_t \gg 1$ (dotted line). The insets exhibit in solid lines the normalized boundary-layer velocity profiles U/U_a at $L_t^{-1} = 21.374$ ($a/\theta = 10$) and $L_t^{-1} = 296.24$ ($a/\theta = 30$) along with the model profiles of Lesshafft & Huerre (2007) computed from (2.11) with the same values of a/θ (dashed lines).

observations of Raynal *et al.* (1996) and Sevilla *et al.* (2002), who found that the radial distance between the inflection points of the base profiles of density and velocity has a profound effect on the stability response, so that when this distance increases, the flow becomes more stable, and the resulting value of S_c decreases. This is precisely the case of the profiles (2.11), whose inflection points are both located at $r = 1$ for $\theta/a = 0$, but continuously move apart from each other for increasing values of θ/a , causing the flow to become more stable and the corresponding value of S_c to decrease, as is clearly seen in figure 2.4. This simple argument of inflection-point displacement by Raynal *et al.* (1996) does not apply however to the analysis of our results, since both the velocity profile and the density profile at the jet exit, given in (2.8), have their inflection points at $r = 1$, regardless of the value of L_t . A more elaborate argument is therefore needed to explain the new results, including the emergence for $m = 0$ of a maximum of S_c at intermediate distances. In that respect, efforts to relate the effects of the shape of the velocity profile with the role of the baroclinic torque, recently found to be the basic mechanism allowing the development of the absolute instability of light jets by Lesshafft & Huerre (2007), could be of interest in future work.

The limit of long injector tubes, $L_t \rightarrow \infty$, yields critical density ratios $S_c \approx 0.7$ and

$S_c \simeq 0.5$ for $m = 0$ and $|m| = 1$, respectively. To determine the prevalence of one mode over the other in this limit of long injectors, it is of interest to plot the difference between their associated absolute growth rates $\omega_i^{(0)}(0)$. Since the values of $\omega_i^{(0)}$ for $m = 0$ are exponentially small for $L_t \rightarrow \infty$, in agreement with the neutral stability of the parabolic Poiseuille profile, while those of the helical mode remain finite, there exist a region in the $S - L_t$ plane, corresponding to the shaded area in figure 2.4(b), where the $|m| = 1$ mode becomes dominant, i.e., its associated value of $\omega_i^{(0)}(0)$ is larger than that of $m = 0$. The result suggests that for near-parabolic velocity profiles, the helical mode should prevail in the globally unstable flow expected for sufficiently small values of $S < 0.5$, a result that deserves to be investigated experimentally in future work. The experimental arrangement should consider in particular injectors longer than those employed in the recent experimental investigation of Hallberg & Strykowski (2006). According to the information given in their figure 1, the maximum value of L_t in their experiments is $L_t \simeq 0.071$, corresponding to a value $L_t^{-1} \simeq 14$, which falls above the region of dominance of the helical mode (the shaded region in figure 2.4). Correspondingly, for their family of injectors the resulting self-excitation was always axisymmetric, in agreement with our analysis.

Note that, although never observed in globally unstable light jets, this change in the prevailing mode of instability from axisymmetric to helical is known to occur in the case of uniform density jets, where the instability is always convective. For nearly uniform velocity profiles the dominant instability mode is the axisymmetric one, whereas when the initial velocity profile is sufficiently developed the helical mode dominates. This theoretical result by Batchelor & Gill (1962) has been confirmed experimentally by Ito & Seno (1979); Zaman & Seiner (1990).

2.4 Conclusions

We have studied the local, linear, spatiotemporal stability of the near field of incompressible, light jets discharging from circular injector tubes of arbitrary length, l_t , for moderately large values of the Reynolds number, Re . To obtain both the basic jet flow, as well as the initial conditions at the exit plane of the injector, we have made use of the axisymmetric boundary layer equations, providing a description independent of Re . Moreover, the local stability properties have been obtained through the inviscid formalism, thus reducing the parameter space to the density ratio, S , and the scaled injector length, $L_t = l_t/(Rea)$.

The results of the linear stability analysis are summarized in figure 2.4, which provides the critical A/C transition curves for gas jets issuing from injectors of different lengths. Clearly, the injector length has a noticeable effect on the stability response

through the shape of the velocity profile at the exit, modifying significantly the critical value of the density ratio. The analysis reveals, in particular, that for an injector length $L_t = 0.04$ the value of the critical density ratio reaches its maximum value, $S_c = 0.9$, which is much larger than those computed previously with use made of model velocity profiles by Monkewitz & Sohn (1988); Lesshafft & Huerre (2007). Also of interest is the prediction of the prevalence of the helical mode in the instability of near-parabolic light jets issuing from very long injectors when $S < 0.5$, a result which should be verified experimentally.

When considering the above results one needs to take into account the limitations of the analysis. Since laminar flow development is assumed within the injector, the analysis is limited to moderately large values of the Reynolds number, so that viscosity effects, not accounted for in the stability development, may have a non-negligible quantitative effect on the results, a point that should be addressed in the future. The extent of the effect can be anticipated from the results of the viscous spatiotemporal stability analysis of Lesshafft & Huerre (2007). Their figure 9 indicates that for $Re = 1000$ and $Re = 5000$ the value of S_c is smaller than the inviscid prediction by roughly 15% and 5%, respectively, although the relative difference becomes smaller as the momentum thickness increases. Departures of the same magnitude can be expected for our base velocity profiles, with the inviscid prediction becoming probably more accurate as the momentum thickness at the jet exit becomes larger for injectors of increasing length.

Furthermore, in view of the exponentially small values of $\omega_i^{(0)}$ associated with axisymmetric perturbations of near-Poiseuille velocity profiles, care should be taken with the interpretation of the result for the critical density ratio S_c for light jets discharging from very long injector tubes, a prediction that should be tested experimentally. Another limitation of the local stability analysis arises in connection with the downstream extent of the region $x_1 < x < x_2$ where one finds $\omega_i^{(0)}(x) > 0$. If $x_1 > 0$, as occurs for the conditions of the upper curve of figure 2.3(a), a global mode is expected to appear in the jet independently of the size of the absolutely unstable region (see Lesshafft *et al.*, 2006). However, if the upstream boundary of the absolutely unstable region is the injector outlet, i.e., $x_1 = 0$ as occurs for the conditions of the upper curve of figure 2.3(b), the global mode is known to be triggered only when $x_2 - x_1$ is sufficiently large (see Lesshafft *et al.*, 2006). Therefore, the appearance of the global mode of instability for $L_t \gtrsim 3.5 \times 10^{-4}$ might require values of S smaller than those given in the critical A/C transition curves of figure 2.4, whose accuracy should be verified experimentally in future work.

References

BACHELOR, G. K. & GILL, A. E. 1962 Analysis of the stability of axisymmetric jets. *J.*

- Fluid Mech.* **14**, 529–551.
- BERS, A. 1975 Linear waves and instabilities. In *Physique des plasmas* (ed. C. Dewitt & J. Peyraud), pp. 117–123. Gordon & Breach.
- BRIGGS, R. J. 1964 *Electron-stream interaction with plasmas (Research monograph no. 29)*. MIT Press.
- CHAPMAN, D. R. 1949 Laminar mixing of a compressible fluid. *Tech. Rep.* NACA-TN-1800. NASA Ames Research Center.
- CHOMAZ, J. M. 2005 Global instabilities in spatially developing flows: Non-normality and nonlinearity. *Ann. Rev. Fluid Mech.* **37**, 357–392.
- COENEN, W., SEVILLA, A. & SÁNCHEZ, A. 2008 Absolute instability of light jets emerging from circular injector tubes. *Phys. Fluids* **20**, 074104.
- COHEN, J. & WYGNANSKI, I. 1987 The evolution of instabilities in the axisymmetrical jet. Part 1. The linear growth of disturbances near the nozzle. *J. Fluid Mech.* **176**, 191–219.
- CRIGHTON, D. G. & GASTER, M. 1976 Stability of slowly divergent jet flow. *J. Fluid Mech.* **77**, 397–413.
- HALLBERG, M. P., SRINIVASAN, V., GORSE, P. & STRYKOWSKI, P. J. 2007 Suppression of global modes in low-density axisymmetric jets using coflow. *Phys. Fluids* **19** (1), 014102.
- HALLBERG, M. P. & STRYKOWSKI, P. J. 2006 On the universality of global modes in low-density axisymmetric jets. *J. Fluid Mech.* **569**, 493–507.
- HOLMES, M. H. 2007 *Introduction to Numerical Methods in Differential Equations*. Springer, New York.
- HUERRE, P. 2000 Open shear flow instabilities. In *Perspectives in fluid dynamics* (ed. G. Batchelor, K. Moffatt & G. Worster), pp. 159–229. Cambridge.
- HUERRE, P. & MONKEWITZ, P. A. 1985 Absolute and convective instabilities in free shear layers. *J. Fluid Mech.* **159**, 151–168.
- HUERRE, P. & MONKEWITZ, P. A. 1990 Local and global instabilities in spatially developing flows. *Annu. Rev. Fluid Mech.* **22**, 473–537.
- ITO, R. & SENO, T. 1979 Effect of exit geometry on jet behavior. *J. Chem. Eng. Jpn.* **12** (6), 430–435.

- JENDOUBI, S. & STRYKOWSKI, P. J. 1994 Absolute and convective instability of axisymmetric jets with external flow. *Phys. Fluids* **6**, 3000–3009.
- KAMBE, T. 1969 The stability of an axisymmetric jet with parabolic profile. *J. Phys. Soc. Jpn.* **26** (2), 566–575.
- KUCHEMAN, D., CRABTREE, L. F. & SOWERBY, L. 1963 Three-dimensional boundary layers. In *Laminar Boundary Layers* (ed. L. Rosenhead), pp. 439–446. Oxford University Press.
- KYLE, D. M. & SREENIVASAN, K. R. 1993 The instability and breakdown of a round variable-density jet. *J. Fluid Mech.* **249**, 619–664.
- LESSEN, M. & SINGH, P. J. 1973 The stability of axisymmetric free shear layers. *J. Fluid Mech.* **60** (3), 433–457.
- LESSHAFFT, L. & HUERRE, P. 2007 Linear impulse response in hot round jets. *Phys. Fluids* **19** (2), 024102.
- LESSHAFFT, L., HUERRE, P. & SAGAUT, P. 2007 Frequency selection in globally unstable round jets. *Phys. Fluids* **19** (5), 054108.
- LESSHAFFT, L., HUERRE, P., SAGAUT, P. & TERRACOL, M. 2006 Nonlinear global modes in hot jets. *J. Fluid Mech.* **554**, 393–409.
- MATTINGLY, G. E. & CHANG, C. C. 1974 Unstable waves on an axisymmetric jet column. *J. Fluid Mech.* **65** (3), 541–560.
- MICHALKE, A. 1970 A note on the spatial jet-instability of the compressible cylindrical vortex sheet. *DLR research rep.* pp. FB–70–51.
- MOLLENDORF, J. C. & GEBHART, B. 1973 An experimental and numerical study of the viscous stability of a round laminar vertical jet with and without thermal buoyancy for symmetric and asymmetric disturbances. *J. Fluid Mech.* **61** (2), 367–399.
- MONKEWITZ, P. A., BECHERT, D. W., BARSIKOW, B. & LEHMANN, B. 1990 Self-excited oscillations and mixing in a heated round jet. *J. Fluid Mech.* **213**, 611–639.
- MONKEWITZ, P. A. & SOHN, K. D. 1988 Absolute instability in hot jets. *AIAA J.* **28**, 911–916.
- MORRIS, P. J. 1976 The spatial viscous instability of axisymmetric jets. *J. Fluid Mech.* **77** (3), 511–529.
- NICHOLS, J. W., SCHMID, P. J. & RILEY, J. J. 2007 Self-sustained oscillations in variable-density round jets. *J. Fluid Mech.* **582**, 341–376.

- PAVITHRAN, S. & REDEKOPP, L. G. 1989 The absolute-convective transition in subsonic mixing layers. *Phys. Fluids A* **1** (10), 1736–1739.
- RAYNAL, L., J.-L., HARION, FAVRE-MARINET, M. & BINDER, G. 1996 The oscillatory instability of plane variable-density jets. *Phys. Fluids* **8**, 993–1006.
- REYNOLDS, A. J. 1962 Observations of a liquid-into-liquid jet. *J. Fluid Mech.* **14**, 552–556.
- SEVILLA, A., GORDILLO, J. M. & MARTÍNEZ-BAZÁN, C. 2002 The effect of the diameter ratio on the absolute and convective instability of free coflowing jets. *Phys. Fluids* **14**, 3028–3038.
- SEVILLA, A. & MARTÍNEZ-BAZÁN, C. 2006 A note on the stabilization of bluff-body wakes by low density base bleed. *Phys. Fluids* **18**, 098102.
- STRYKOWSKI, P. J. & NICCUM, D. L. 1991 The stability of countercurrent mixing layers in circular jets. *J. Fluid Mech.* **227**, 309–343.
- THEOFILIS, V. 2003 Advances in global linear instability analysis of nonparallel and three-dimensional flows. *Prog. Aerosp. Sci.* **39**, 249.
- YU, M.-H. & MONKEWITZ, P. A. 1990 The effect of nonuniform density on the absolute instability of two-dimensional inertial wakes and jets. *Phys. Fluids A* **2**, 611–639.
- ZAMAN, K. B. M. Q. & SEINER, J. M. 1990 Viscous effects on the instability of an axisymmetric jet. *Tech. Rep.* NASA-TM-102396. NASA Glenn Research Center.

Viscous stability analysis of parallel flows with discontinuous base profiles

The viscous linear instability of parallel gas flows with piecewise constant base profiles is considered in the limit of low Mach numbers, both for planar and axisymmetric geometries such as mixing layers, jets and wakes. Our results generalize those of Drazin (*J. Fluid Mech.* vol. 10, 1961, p. 571), by contemplating the possibility of arbitrary jumps in density and transport properties between two uniform streams separated by a vortex sheet. The eigenfunctions, obtained analytically in the regions of uniform flow, are matched through an appropriate set of jump conditions at the discontinuity of the basic flow, which are derived by repeated integration of the linearized conservation equations in their primitive variable form. The development leads to an algebraic dispersion relation that is validated through comparisons with stability calculations performed with continuous profiles and is applied, in particular, to study the effects of molecular transport on the spatiotemporal stability of parallel nonisothermal gaseous jets and wakes with very thin shear layers.

3.1 Introduction

Many of the early efforts to investigate the instability of parallel shear flows were based on simple flow configurations with discontinuous base velocity profiles, with prominent examples being the inviscid vortex-sheet investigations of Helmholtz (1868) and Kelvin (1871) and Rayleigh's stability analysis of the shear layer with piecewise linear velocity profile (Rayleigh, 1880). These inviscid analyses involve integration of Rayleigh's equation for the perturbations of the stream function with appropriate matching conditions at the discontinuities corresponding to the requirement that the pressure and the normal velocity be continuous across the material interface. Viscous effects can be taken into account in the perturbations through the use of the Orr-Sommerfeld equation, as done by Esch (1957) for the analysis of Rayleigh's piecewise linear configuration and by Drazin (1961) for base flows with discontinuous velocity profiles. As shown by Drazin

(1961), the correct set of viscous jump conditions at the discontinuities of the base velocity profile can be derived by integrating the Orr-Sommerfeld equation four times across the discontinuity, and then taking the limit of vanishing integration intervals.

As discussed by Drazin (1961), the use of discontinuous base profiles as a leading-order representation for the flow field, with the shear layers being substituted by vortex sheets, is a valid approach for the analysis of normal modes with wavelength much larger than the shear-layer thickness. The advantage of Drazin's approach is that it leads to a closed algebraic expression for the dispersion relation, thereby facilitating analytical developments and reducing computational costs. The corresponding dispersion relations for the plane mixing layer and the symmetric plane jet, obtained by Drazin (1961), were shown to be in agreement with the corresponding low-wavenumber approximations for continuous base profiles, which had been previously obtained by Tatsumi & Gotoh (1960) and by Tatsumi & Kakutani (1958), respectively, thus demonstrating the validity of the approach. In a subsequent study, Drazin (1962) extended the model to include the effects of variable density and viscosity, but only for incompressible flow and excluding heat conduction and species diffusion.

It is important to emphasize that, as pointed out by Drazin (1961), there is no contradiction in retaining viscous effects in the perturbations while neglecting them in the basic flow, as long as one keeps in mind that the validity of the approach is restricted to the study of modes with wavelength much larger than the shear-layer thickness. Two important examples satisfying this condition are the columnar modes of jets and wakes, which are known to play a relevant role in their stability (see Huerre & Monkewitz, 1990), and dominate their dynamics when self-excited by becoming locally absolutely unstable in the near field (see, for instance Huerre & Monkewitz, 1985; Monkewitz, 1988; Monkewitz & Sohn, 1988; Yu & Monkewitz, 1990). Previous viscous stability analyses of these jet and wake flows, including planar (Yu & Monkewitz, 1990) and axisymmetric (Lesshafft & Huerre, 2007) configurations, have made use of model base profiles with thin shear layers. Since the relevant wavelengths for the columnar modes are on the order of the jet or wake radius, the shear-layer thickness enters in the analysis as a secondary parameter that takes small nonzero values. The relevant limit of vanishing shear-layer thickness is difficult to investigate numerically with continuous base profiles, because the associated integrations become very costly when the shear-layer thickness takes small values. Consideration of discontinuous base profiles arises as a valid alternative in this case and serves as motivation for the present work. The required development involves an extension of Drazin's work to cylindrical geometries and non-solenoidal disturbances. The analysis needs to employ the linear stability equations in their primitive variable form. Repeated integrals of these equations provide the necessary jump conditions for the perturbations across the discontinuities of the base profiles.

The main objective of the present work is to extend the formalism introduced by Drazin (1961), providing the appropriate framework to study viscous modal solutions of planar and axisymmetric piecewise-constant parallel basic flows. The analysis focuses on non-buoyant gas flows with constant molecular weight and small values of the Mach number. The chapter is organized as follows. The formulation of the linear stability problem is presented in § 3.2 followed in § 3.3 by a detailed derivation of the general jump conditions that apply across a discontinuity. Then, in § 3.4, the stability problem is solved for the particular case of flows with piecewise constant profiles of velocity, density and transport properties giving, in particular, the eigenfunctions corresponding to regions of uniform flow. The jump conditions derived in § 3.3 will be used to obtain in § 3.4 a dispersion relation for the particular case of non-isothermal jets and wakes of ideal gases with a presumed power-law temperature dependence for the viscosity and thermal conductivity. The validity of the dispersion relation is assessed in § 3.5 by comparisons with the results obtained by integrating numerically the linearized stability equations with continuous base profiles in the limit of very thin shear layers. The dispersion relation is utilized to study the spatiotemporal stability of plane and axisymmetric jets and wakes, obtaining, in particular, the dependence on molecular transport of the critical conditions for transition between convective and absolute instability. Finally, § 3.6 is devoted to conclusions.

3.2 Stability equations for low-Mach-number parallel flows

To write the stability problem for the parallel gas flow, the velocity \mathbf{u}^* , density ρ^* , temperature T^* , shear viscosity μ^* , and thermal conductivity κ^* are scaled with their characteristic values U_0^* , ρ_0^* , T_0^* , μ_0^* , and κ_0^* , while the bulk viscosity μ_V^* is scaled with μ_0^* and the pressure variation from the reference value p^* is scaled with the characteristic dynamic pressure $\rho_0^* U_0^{*2}$, as corresponds to the low Mach number approximation used here. In the notation, dimensional quantities are denoted with an asterisk $*$; all other quantities are supposed to be nondimensional. Both cartesian and cylindrical coordinate systems will be employed, as denoted by $j = (0, 1)$ in the formulation, with a suitable characteristic length a^* introduced to give the dimensionless coordinates (x, r, z) and (x, r, θ) , respectively, with unit vectors represented by $(\mathbf{e}_1, \mathbf{e}_2, \mathbf{e}_3)$.

The stability analysis begins by assuming that the flow can be decomposed into a steady parallel basic flow in the x direction and small fluctuating disturbances according to $\mathbf{u}^*/U_0^* = \mathbf{U} + \mathbf{u}$, $\rho^*/\rho_0^* = \bar{\rho} + \rho$, $T^*/T_0^* = \bar{T} + T$, $\mu^*/\mu_0^* = \bar{\mu} + \mu$, $\mu_V^*/\mu_0^* = \bar{\mu}_V + \mu_V$, $\kappa^*/\kappa_0^* = \bar{\kappa} + \kappa$ and $p^*/(\rho_0^* U_0^{*2}) = p$, with $\mathbf{u} = (u, v, w)$. The base-flow variables, which, with the exception of the velocity $\mathbf{U} = (U, 0, 0)$, are denoted by a bar, are allowed to vary with the transverse coordinate r , except for the base pressure variation, which is

identically zero in the parallel flow approximation used here.

Following the usual methods of hydrodynamic stability, the continuity, momentum and energy conservation equations may be linearized around the base flow, yielding the following system of linear equations for the disturbances

$$\frac{\partial \rho}{\partial t} + U \frac{\partial \rho}{\partial x} + \bar{\rho} \nabla \cdot \mathbf{u} + \bar{\rho}' v = 0 \quad (3.1a)$$

$$\begin{aligned} \bar{\rho} \left(\frac{\partial \mathbf{u}}{\partial t} + U \frac{\partial \mathbf{u}}{\partial x} + U' v \mathbf{e}_1 \right) = & -\nabla p + \frac{1}{Re} \left[\bar{\mu} \nabla^2 \mathbf{u} + \left(\bar{\mu}'_v + \frac{1}{3} \bar{\mu}' \right) \nabla (\nabla \cdot \mathbf{u}) \right. \\ & + \left(\bar{\mu}'_v - \frac{2}{3} \bar{\mu}' \right) (\nabla \cdot \mathbf{u}) \mathbf{e}_2 + \bar{\mu}' (\nabla \mathbf{u} + \nabla \mathbf{u}^T) \cdot \mathbf{e}_2 + \left(U' \bar{\mu}' \mathbf{e}_1 + U' \frac{\partial \bar{\mu}}{\partial x} \mathbf{e}_2 \right) \\ & \left. + \left(U'' + j \frac{U'}{r} \right) \bar{\mu} \mathbf{e}_1 \right], \end{aligned} \quad (3.1b)$$

$$\bar{\rho} \left(\frac{\partial T}{\partial t} + U \frac{\partial T}{\partial x} + \bar{T}' v \right) = \frac{1}{Re Pr} \left[\bar{\kappa} \nabla^2 T + \bar{\kappa}' T' + \bar{T}' \kappa' + \left(\bar{T}'' + j \frac{\bar{T}'}{r} \right) \kappa \right], \quad (3.1c)$$

where the prime ' denotes differentiation with respect to r and ∇ is the dimensionless nabla operator. In the formulation, $Re = \rho_0^* U_0^* a^* / \mu_0^*$ and $Pr = c_p^* \mu_0^* / \kappa_0^*$ are the Reynolds and Prandtl numbers, with c_p^* representing the specific heat at constant pressure for the gas mixture, assumed to be constant. The effect of body forces has been neglected in (3.1b). Also, both compressibility and viscous dissipation have been discarded in (3.1c), an approximation that involves relative errors of the order of the square of the Mach number, negligibly small in the limit of low Mach numbers considered here.

The above equations are to be supplemented with the equation of state written in the low Mach number approximation, i.e., with pressure differences neglected, and with appropriate constitutive laws for the variation of the transport properties. In principle, when the flow involves a mixture of different gases, the composition enters in determining the mean molecular weight and the transport coefficients, so that the above equations should be supplemented with species conservation equations written for the mass fractions $\bar{Y}_\alpha + Y_\alpha$ of each different chemical species α . The resulting equations for the perturbations Y_α would be similar to (3.1c), with the Schmidt number of each species replacing the Prandtl number and with the product of the density times the species diffusivity replacing the thermal conductivity. For simplicity in the development, variations of molecular weight will be neglected in the equation of state and only temperature variations of transport properties will be considered, so that the descriptions of the composition field and its disturbances will not be necessary. Nevertheless, comments on the extensions of the analysis to account for changes in composition are offered below in § 3.6.

The following analysis focuses on wave-like perturbations of the form

$$(\rho, T, \mu, \mu_V, u, v, w, p) = (\hat{\rho}, \hat{T}, \hat{\mu}, \hat{\mu}_V, \hat{u}, i\hat{v}, \hat{w}, \hat{p}) \begin{cases} e^{i(kx+mz-\omega t)} & (j=0), \\ e^{i(kx+m\theta-\omega t)} & (j=1), \end{cases} \quad (3.2)$$

with k and m denoting the streamwise and spanwise/azimuthal wave numbers and ω being the angular frequency. Substituting these normal modes into (3.1a)–(3.1c) yields the following set of stability equations:

$$(kU - \omega)\hat{\rho} + k\bar{\rho}\hat{u} + \frac{(r^j\bar{\rho}\hat{v})'}{r^j} + \frac{m\bar{\rho}\hat{w}}{r^j} = 0, \quad (3.3a)$$

$$\begin{aligned} \bar{\mu}\hat{\nabla}_{\beta,m}^2\hat{u} - i\text{Re}U'\bar{\rho}\hat{v} - i\text{Re}k\hat{p} - \left(\bar{\mu}_V + \frac{\bar{\mu}}{3}\right)k\left[k\hat{u} + \frac{(r^j\hat{v})'}{r^j} + \frac{m\hat{w}}{r^j}\right] \\ + \bar{\mu}'(\hat{u}' - k\hat{v}) + U'\hat{\mu}' + \frac{(r^jU')'\hat{\mu}}{r^j} = 0, \end{aligned} \quad (3.3b)$$

$$\begin{aligned} \bar{\mu}\left[\hat{\nabla}_{\beta,m}^2\hat{v} - \frac{j(\hat{v} + 2m\hat{w})}{r^2}\right] + i\text{Re}\hat{p}' + \left(\bar{\mu}_V + \frac{\bar{\mu}}{3}\right)\left[k\hat{u}' + \left(\frac{(r^j\hat{v})'}{r^j}\right)'\right] + m\left(\frac{\hat{w}}{r^j}\right)' \\ + \left(\bar{\mu}'_V - \frac{2\bar{\mu}'}{3}\right)\left[k\hat{u} + \frac{(r^j\hat{v})'}{r^j} + \frac{m\hat{w}}{r^j}\right] + 2\bar{\mu}'\hat{v}' + kU'\hat{\mu} = 0, \end{aligned} \quad (3.3c)$$

$$\begin{aligned} \bar{\mu}\left[\hat{\nabla}_{\beta,m}^2\hat{w} - \frac{j(\hat{w} + 2m\hat{v})}{r^2}\right] - \frac{i\text{Re}m\hat{p}}{r^j} - \left(\bar{\mu}_V + \frac{\bar{\mu}}{3}\right)\frac{m}{r^j}\left[k\hat{u} + \frac{(r^j\hat{v})'}{r^j} + \frac{m\hat{w}}{r^j}\right] \\ + \bar{\mu}'\left[r^j\left(\frac{\hat{w}}{r^j}\right)' - \frac{m\hat{v}}{r^j}\right] = 0, \end{aligned} \quad (3.3d)$$

$$\bar{\kappa}\hat{\nabla}_{\gamma,m}^2\hat{T} - i\text{Re}Pr\bar{\rho}\bar{T}'\hat{v} + \bar{\kappa}'\hat{T}' + \bar{T}'\hat{\kappa}' + \frac{(r^j\bar{T}')'\hat{\kappa}}{r^j} = 0, \quad (3.3e)$$

where the reduced Laplacian operator

$$\hat{\nabla}_{\phi,m}^2 = \frac{1}{r^j} \frac{d}{dr} \left(r^j \frac{d}{dr} \right) - \left(\phi^2 + \frac{m^2}{r^{2j}} \right), \quad (3.4)$$

has been introduced for convenience. The quantity ϕ takes the values $\phi = \beta$ and $\phi = \gamma$ in the momentum and energy equations, respectively, with

$$\beta = [k^2 + i\text{Re}(kU - \omega)\bar{\rho}/\bar{\mu}]^{1/2}, \quad (3.5a)$$

$$\gamma = [k^2 + i\text{Re}Pr(kU - \omega)\bar{\rho}/\bar{\kappa}]^{1/2}, \quad (3.5b)$$

defined with a non-negative real part for definiteness.

The stability equations must be accompanied with suitable boundary conditions. In infinite or semi-infinite domains, all perturbations must vanish in the far field, yielding

$$(\hat{\rho}, \hat{T}, \hat{\mu}, \hat{\mu}_V, \hat{\kappa}, \hat{u}, \hat{v}, \hat{w}, \hat{p}) \rightarrow 0 \quad \text{as } r \rightarrow \infty. \quad (3.6)$$

The boundary conditions at the centerline $r = 0$ depend on the symmetry of the problem. In planar flows with symmetric base profiles, we can impose either symmetry or antisymmetry for the perturbations at $r = 0$, yielding two different sets of solutions, referred to as varicose and sinuous modes of instability, respectively. For the symmetric mode, the transverse perturbation velocity \hat{v} is an odd function of r . Conversely, \hat{v} is an even function for the antisymmetric or sinuous mode. For reasons that will become clear later, and following Yu & Monkewitz (1990), we will distinguish between both modes of instability through a parameter s defined according to

$$s = \begin{cases} +1: & \text{sinuous mode} \\ -1: & \text{varicose mode.} \end{cases}$$

The boundary conditions at $r = 0$ for planar flows, $j = 0$, can then be written as

$$r = 0 : \begin{cases} \hat{\rho}' = \hat{T}' = \hat{\mu}' = \hat{\mu}'_V = \hat{\kappa}' = \hat{u}' = \hat{w}' = \hat{p}' = 0 \text{ and } \hat{v} = 0 & (s = -1), \\ \hat{\rho} = \hat{T} = \hat{\mu} = \hat{\mu}_V = \hat{\kappa} = \hat{u} = \hat{w} = \hat{p} = 0 \text{ and } \hat{v}' = 0 & (s = +1). \end{cases} \quad (3.7)$$

In axisymmetric flows, on the other hand, we have to impose a vanishing azimuthal dependence of the velocity vector as the axis $r = 0$ is approached (see Batchelor & Gill, 1962), i.e. $\lim_{r \rightarrow 0} \frac{\partial}{\partial \theta} (u\mathbf{e}_1 + v\mathbf{e}_2 + w\mathbf{e}_3) = 0$. This leads to boundary conditions at the axis that take the form

$$r = 0 : \begin{cases} \hat{v} = \hat{w} = \hat{u}' = 0 \text{ and } (\hat{\rho}, \hat{T}, \hat{\mu}, \hat{\mu}_V, \hat{\kappa}, \hat{u}, \hat{p}) \text{ finite} & (m = 0), \\ (\hat{\rho}, \hat{T}, \hat{\mu}, \hat{\mu}_V, \hat{\kappa}, \hat{u}, \hat{p}) = \hat{v} \pm \hat{w} = \hat{v}' = 0 & (m = \pm 1), \\ (\hat{\rho}, \hat{T}, \hat{\mu}, \hat{\mu}_V, \hat{\kappa}, \hat{u}, \hat{v}, \hat{w}, \hat{p}) = 0 & (|m| > 1), \end{cases} \quad (3.8)$$

different for different azimuthal modes.

3.3 Boundary conditions for the disturbances at a discontinuity of the base flow

When solving the stability problem in the presence of discontinuities of either the base profiles or their derivatives, separate domains need to be considered for the integration of the stability equations (3.3a)–(3.3e). The resulting solutions are then matched at the surfaces of discontinuity through appropriate jump conditions, which can be derived from repeated integrals of the conservation equations (3.3a)–(3.3e) across the discon-

tinuity, as shown below. In the analysis, the surface of discontinuity, separating two regions denoted by I and II, is assumed to be located at an arbitrary radial location $r = r_o$. The resulting integrals are evaluated in the range $r = r_o \pm \varepsilon$, with the jump conditions arising as the limiting forms of the resulting integrals when the limit $\varepsilon \rightarrow 0$ is taken for the semithickness of the integration domain. The methodology follows that employed by Drazin (1961) in deriving jump conditions for the Orr-Sommerfeld equation, although the necessary analysis is somewhat more elaborate here because of the presence of a larger number of equations and variables, which in turn leads to a number of intricacies in the development that are worth explaining in some detail, thereby justifying the derivation given below.

The derivation begins by integrating once the stability equations (3.3a)–(3.3e) after multiplication by r^j to yield

$$r^j \bar{\rho} \hat{v} = - \int r^j (kU - \omega) \hat{\rho} \, dr - k \int r^j \bar{\rho} \hat{u} \, dr - m \int \bar{\rho} \hat{w} \, dr, \quad (3.9a)$$

$$\begin{aligned} r^j \left(\bar{\mu} \hat{u}' + U' \hat{\mu} + k \bar{\mu} \hat{v} - i \operatorname{Re} U \bar{\rho} \hat{v} - 2k \bar{\rho} \hat{v} \int \frac{\bar{\mu}'}{\bar{\rho}} \, dr \right) &= \int r^j \left(\beta^2 + \frac{m^2}{r^{2j}} \right) \bar{\mu} \hat{u} \, dr \\ &+ k \int r^j \left[\frac{2\bar{\mu}(r^j \hat{v})'}{r^j} + \left(\bar{\mu}_V - \frac{2\bar{\mu}}{3} \right) \frac{(r^j \hat{v})'}{r^j} + i \operatorname{Re} \hat{p} \right] \, dr - i \operatorname{Re} \int U (r^j \bar{\rho} \hat{v})' \, dr \\ &+ k \int \left(\bar{\mu}_V + \frac{\bar{\mu}}{3} \right) (r^j k \hat{u} + m \hat{w}) \, dr - 2k \int (r^j \bar{\rho} \hat{v})' \int \frac{\bar{\mu}'}{\bar{\rho}} \, dr \, dr, \end{aligned} \quad (3.9b)$$

$$\begin{aligned} r^j \left[\frac{2\bar{\mu}(r^j \hat{v})'}{r^j} + \left(\bar{\mu}_V - \frac{2\bar{\mu}}{3} \right) \left(k \hat{u} + \frac{(r^j \hat{v})'}{r^j} + \frac{m \hat{w}}{r^j} \right) + i \operatorname{Re} \hat{p} \right] &- 2j \bar{\rho} \hat{v} \int \frac{\bar{\mu}'}{\bar{\rho}} \, dr \\ &= \int r^j \left(\beta^2 + \frac{m^2}{r^{2j}} \right) \bar{\mu} \hat{v} \, dr - \int r^j k (\bar{\mu} \hat{u}' + U' \hat{\mu}) \, dr \\ &+ j \int \left[\frac{2\bar{\mu}(r^j \hat{v})'}{r^j} + \left(\bar{\mu}_V - \frac{2\bar{\mu}}{3} \right) \left(k \hat{u} + \frac{(r^j \hat{v})'}{r^j} + \frac{m \hat{w}}{r^j} \right) + i \operatorname{Re} \hat{p} \right] \, dr \\ &+ 3jm \int \frac{\bar{\mu} \hat{w}}{r^j} \, dr - m \int \bar{\mu} \hat{w}' \, dr - 2j \int (\bar{\rho} \hat{v})' \int \frac{\bar{\mu}'}{\bar{\rho}} \, dr \, dr, \end{aligned} \quad (3.9c)$$

$$\begin{aligned} r^{2j} \bar{\mu} \left(\frac{\hat{w}}{r^j} \right)' + m \bar{\mu} \hat{v} - 2m \bar{\rho} \hat{v} \int \frac{\bar{\mu}'}{\bar{\rho}} \, dr &= \int r^j \left(\beta^2 + \frac{m^2}{r^{2j}} \right) \bar{\mu} \hat{w} \, dr \\ &+ j \int \frac{1}{r} \left[m \bar{\mu} \hat{v} - r^2 \bar{\mu} \left(\frac{\hat{w}}{r} \right)' \right] \, dr + m \int \left(\bar{\mu}_V + \frac{\bar{\mu}}{3} \right) \left(k \hat{u} + \frac{m \hat{w}}{r^j} \right) \, dr \\ &+ m \int \left[\frac{2\bar{\mu}(r^j \hat{v})'}{r^j} + \left(\bar{\mu}_V - \frac{2\bar{\mu}}{3} \right) \frac{(r^j \hat{v})'}{r^j} + i \operatorname{Re} \hat{p} \right] \, dr \\ &- 2m \int (\bar{\rho} \hat{v})' \int \frac{\bar{\mu}'}{\bar{\rho}} \, dr \, dr, \end{aligned} \quad (3.9d)$$

$$r^j (\bar{\kappa} \hat{T}' + \bar{T}' \hat{\kappa} - i \operatorname{Re} Pr \bar{T} \hat{\rho} \hat{v}) = \int r^j \left(\gamma^2 + \frac{m^2}{r^{2j}} \right) \bar{\kappa} \hat{T} \, dr - i \operatorname{Re} Pr \int \bar{T} (r^j \bar{\rho} \hat{v})' \, dr. \quad (3.9e)$$

Integration by parts has been used to arrange the equations so that all of the integrands appearing in the right-hand-side integrals remain finite within the discontinuity, and therefore give a vanishing contribution when the integrals are evaluated in the range $r = r_o \pm \varepsilon$ and the limit $\varepsilon \rightarrow 0$ is considered. As a consequence, the resulting jump conditions emerging from these first quadratures involve only the terms on the left-hand side. This can be clearly seen, for instance, in the first quadrature of the continuity equation, given in (3.9a), where the base profiles and the disturbances $\hat{\rho}$, \hat{u} and \hat{w} appearing in the right-hand-side integrals can be anticipated to be finite, thereby resulting in a vanishing contribution in the limit $\varepsilon \rightarrow 0$. The continuity balance (3.9a) therefore requires that the transverse mass flux $\bar{\rho}\hat{v}$ takes equal values on both sides of the discontinuity, a condition that will be indicated by $[\bar{\rho}\hat{v}]_I^{\text{II}} = 0$.

This condition of continuity of $\bar{\rho}\hat{v}$ can be used to prove that the last integral in (3.9e) also gives a vanishing contribution in the limit $\varepsilon \rightarrow 0$, so that the jump condition $[\bar{\kappa}\hat{T}' + \bar{T}'\hat{\kappa} - iRePr\bar{T}\bar{\rho}\hat{v}]_I^{\text{II}} = 0$ follows, because the second last integral also vanishes in the limit $\varepsilon \rightarrow 0$ provided \hat{T} remains finite. Since in the present approximation the thermal conductivity is only a function of the temperature, its disturbances and those of the temperature are related by the equation $\hat{\kappa}/\bar{\kappa}' = \hat{T}/\bar{T}'$, which can be used in a second quadrature of (3.9e) to give

$$\begin{aligned} \bar{\kappa}\hat{T}' &= iRePr \int \bar{T}\bar{\rho}\hat{v} dr + \int \frac{1}{r^j} \int r^j \left(\gamma^2 + \frac{m^2}{r^{2j}} \right) \bar{\kappa}\hat{T} dr \\ &\quad - iRePr \int \frac{1}{r^j} \int \bar{T}(r^j\bar{\rho}\hat{v})' dr dr, \end{aligned} \quad (3.10)$$

thereby leading naturally to the additional jump condition $[\bar{\kappa}\hat{T}]_I^{\text{II}} = 0$ when the limit $\varepsilon \rightarrow 0$ is taken.

For those terms on the right-hand sides of (3.9b)–(3.9d) that involve functions that might be expected to be singular, such as \hat{v}' , or derivatives of discontinuous functions, such as U' , proving the vanishing of the associated integrals necessitates additional information arising from second quadratures. Dividing (3.9b)–(3.9d) by $r^j\bar{\mu}$, r^j and $r^{2j}\bar{\mu}$, respectively, and integrating yields

$$\begin{aligned} \hat{u} + \int \frac{U'\hat{\mu}}{\bar{\mu}} dr &= -k \int \hat{v} dr + iRe \int \frac{U\bar{\rho}\hat{v}}{\bar{\mu}} dr + 2k \int \frac{\bar{\rho}\hat{v}}{\bar{\mu}} \int \frac{\bar{\mu}'}{\bar{\rho}} dr dr \\ &\quad + \int \frac{1}{r^j\bar{\mu}} [\text{terms on r.h.s. of equation (3.9b)}] dr, \end{aligned} \quad (3.11a)$$

$$\begin{aligned} \int \left[\frac{2\bar{\mu}(r^j\hat{v})'}{r^j} + \left(\bar{\mu}_v - \frac{2\bar{\mu}}{3} \right) \left(k\hat{u} + \frac{(r^j\hat{v})'}{r^j} + \frac{m\hat{w}}{r^j} \right) + iRe\hat{p} \right] dr \\ = \int \frac{2j\bar{\rho}\hat{v}}{r^j} \int \frac{\bar{\mu}'}{\bar{\rho}} dr dr + \int \frac{1}{r^j} [\text{terms on r.h.s. of equation (3.9c)}] dr, \end{aligned} \quad (3.11b)$$

and

$$\begin{aligned} \hat{w} = & -mr^j \int \frac{\hat{v}}{r^{2j}} dr + 2mr^j \int \frac{\bar{\rho}\hat{v}}{r^{2j}\bar{\mu}} \int \frac{\bar{\mu}'}{\bar{\rho}} dr dr \\ & + r^j \int \frac{1}{r^{2j}\bar{\mu}} [\text{terms on r.h.s. of equation (3.9d)}] dr. \end{aligned} \quad (3.11c)$$

Again, it can be seen that all of the single integrals that appear on the right-hand side vanish in the limiting procedure used here, as their integrands at most experience finite jumps across the discontinuity layer. Furthermore, all of the terms that involve double integrals of the form $\int f(r) \int g(r) dr dr$ can also be shown to vanish since both $f(r)$ and $\int g(r) dr$ at most experience finite jumps at $r = r_o$. Consequently, in the limit $\varepsilon \rightarrow 0$, (3.11a) and (3.11c) provide the jump conditions $[\hat{u}]_I^{\text{II}} = -\int_{r_o-\varepsilon}^{r_o+\varepsilon} (U' \hat{\mu} / \bar{\mu}) dr$ and $[\hat{w}]_I^{\text{II}} = 0$, respectively, while (3.11b) indicates that the integral on its left-hand side vanishes when evaluated between $r_o - \varepsilon$ and $r_o + \varepsilon$. Bearing this new information in mind it is straightforward to prove now that all of the integrals appearing on the right-hand side of (3.9b)–(3.9d) indeed vanish in the limit $\varepsilon \rightarrow 0$, so that their associated jump conditions involve only the terms on the left-hand side, as previously anticipated. This therefore completes the derivation of the set of eight jump conditions to be satisfied by the disturbances across the discontinuity of the basic flow, which are summarized below for convenience.

$$[\hat{u}]_I^{\text{II}} = -\bar{\kappa} \hat{T} \int_I^{\text{II}} \frac{U' \bar{\mu}'}{\bar{\mu} \bar{\kappa} \bar{T}'} dr, \quad (3.12a)$$

$$[\bar{\rho} \hat{v}]_I^{\text{II}} = 0, \quad (3.12b)$$

$$[\hat{w}]_I^{\text{II}} = 0, \quad (3.12c)$$

$$[\bar{\kappa} \hat{T}]_I^{\text{II}} = 0, \quad (3.12d)$$

$$[\bar{\mu} \hat{u}' + U' \hat{\mu} + k \bar{\mu} \hat{v} - i \text{Re} U \bar{\rho} \hat{v}]_I^{\text{II}} = 2k \bar{\rho} \hat{v} \int_I^{\text{II}} \frac{\bar{\mu}'}{\bar{\rho}} dr, \quad (3.12e)$$

$$\left[\frac{2\bar{\mu}(r^j \hat{v})'}{r^j} + \left(\bar{\mu}_V - \frac{2\bar{\mu}}{3} \right) \left(k \hat{u} + \frac{(r^j \hat{v})'}{r^j} + \frac{m \hat{w}}{r^j} \right) + i \text{Re} \hat{p} \right]_I^{\text{II}} = \frac{2j \bar{\rho} \hat{v}}{r^j} \int_I^{\text{II}} \frac{\bar{\mu}'}{\bar{\rho}} dr, \quad (3.12f)$$

$$\left[\bar{\mu} \left(\frac{\hat{w}}{r^j} \right)' + m \bar{\mu} \hat{v} \right]_I^{\text{II}} = 2m \bar{\rho} \hat{v} \int_I^{\text{II}} \frac{\bar{\mu}'}{\bar{\rho}} dr, \quad (3.12g)$$

$$[\bar{\kappa} \hat{T}' + \bar{T}' \hat{\kappa} - i \text{Re} Pr \bar{T} \bar{\rho} \hat{v}]_I^{\text{II}} = 0. \quad (3.12h)$$

The integral on the right-hand side of (3.12a) is obtained by integrating by parts the term $-\int_{r_o-\varepsilon}^{r_o+\varepsilon} (U' \hat{\mu} / \bar{\mu}) dr$ with $\hat{\mu} = \bar{\mu}' \hat{T} / \bar{T}'$, as corresponds to the viscosity being expressible as a function of the temperature, and with the condition that the heat flux derivative

$(\bar{\kappa}\bar{T})'$ be finite in the discontinuity, as implied by (3.12d), which is used in evaluating the resulting integral.

As can be seen, the jump conditions involve two different integrals of the base profiles across the discontinuity $\int_I^{II} [(U'\bar{\mu}')/(\bar{\mu}\bar{\kappa}\bar{T}')] dr$ and $\int_I^{II} (\bar{\mu}'/\bar{\rho}) dr$. If the molecular-weight variation is neglected in the equation of state to give $\bar{\rho} = \bar{T}^{-1}$ and with the viscosity assumed to be a function of the temperature, the latter integral can be expressed in the alternative form $\int_I^{II} (\bar{\mu}'/\bar{\rho}) dr = \int_I^{II} \bar{T} d\bar{\mu}$, which, for a given presumed temperature dependence $\bar{\mu}(\bar{T})$, is only a function of the boundary values of \bar{T} at $r = r_o \pm \varepsilon$, but it is otherwise independent of the specific form of the temperature profile across the discontinuity. The integral appearing on the right-hand side of (3.12a) involves however the derivative of the base velocity profile U' , and therefore depends in principle on the shape of the base profiles of temperature and velocity. If a suitable relationship is assumed for $U(\bar{T})$, as done in many studies by introducing Crocco-Busemann's equation for the base profiles, then the integral can be written as a function of the boundary values of the velocity and temperature on both sides of the discontinuity, without reference to the specific shapes of the profiles found inside. Note that the unexpected dependence of the jump conditions on the specific shapes of the base profiles within the discontinuity was also encountered by Drazin (1962) in his stability analysis of incompressible parallel flow with variable density and viscosity. Also of interest is that the dependence found above disappears in flows with constant viscosity such that $\bar{\mu}' = 0$.

The boundary condition (3.12h) states that the transverse transport rate of heat must be equal on both sides of the discontinuity, whereas (3.12e)–(3.12g) correspond to the equilibrium of normal and tangential stresses, and involve both the surface curvature and the variation of the base viscosity across the discontinuity. The conservation of mass flow rate across the discontinuity determines the jump of radial velocity \hat{v} according to (3.12b), while the azimuthal perturbation velocity \hat{w} does not change, as implied by (3.12c), and the streamwise disturbance \hat{u} presents a jump when variations of base viscosity are considered, as observed in (3.12a). It is also of interest that changes in thermal conductivity lead to changes in temperature across the discontinuity, as seen in (3.12d). Clearly, while some of these results could have been anticipated from the beginning, other are less intuitive and require the careful derivation given above.

To test the jump conditions given in (3.12a)–(3.12h), numerical integrations of the stability equations (3.3a)–(3.3e) were performed for base profiles including a layer of rapid radial variation, with the limit of discontinuous base profiles being approached by decreasing the thickness of this layer. In particular, the results shown in figure 3.1 correspond to the first helical stability mode ($m = 1$) of an axisymmetric jet with $Re = 50$, $Pr = 0.7$ and with base profiles defined by $U = 1 + \tanh[125(1/r - r)]$, $\bar{T} = 1/\bar{\rho} = 1 - 0.4(2 - U)$, $\bar{\mu} = \bar{\kappa} = \bar{T}^{0.7}$ and $\bar{\mu}_V = 0$, representing a hot air jet with a very thin shear layer of characteristic momentum thickness $\theta = 1/500$ as defined by Lesshaft & Huerre (2007)

(see the general expressions given below in (3.30) and (3.32)). For generality, the conditions selected are such that all terms in the jump conditions (3.12a)–(3.12h) are nonzero, including the integral contributions on the right-hand side of (3.12a) and (3.12e)–(3.12g).

Although the base profiles used in the computations are continuous, the presence of a thin shear layer at $r = 1$ produces a very rapid variation of some of the eigenfunctions, corresponding to the jumps identified in (3.12a)–(3.12h) for discontinuous base profiles. This is illustrated in the figure by representing with solid lines the radial variation of the eigenfunctions \hat{u} , \hat{v} , \hat{w}' , \hat{v}' and \hat{p} obtained for $k = 1$, for which the accompanying angular frequency is found to be $\omega = 0.314 + 0.176i$. As can be seen in figures 3.1(a) and 3.1(b), the axial and radial velocity components \hat{u} and \hat{v} exhibit rapid changes at $r = 1$, which are however not present in the functions $\hat{u} + \bar{\kappa} \hat{T} \int [(U' \bar{\mu}') / (\bar{\mu} \bar{\kappa} \bar{T}')] dr$ and $\bar{\rho} \hat{v}$, shown in the figures as dashed lines, in agreement with the jump conditions (3.12a) and (3.12b). Similarly, the radial gradient of azimuthal velocity \hat{w}' , shown in figure 3.1(c) presents a steep gradient, whereas the function $\bar{\mu} (\hat{w}/r^j)' + m \bar{\mu} \hat{v} + 2m \bar{\rho} \hat{v} \int (\bar{\mu}'/\rho) dr$, denoted in this figure by the dashed line, does not, therefore validating the jump condition (3.12g). The rapid change of \hat{v} across the shear layer, shown in figure 3.1(b), is associated with a large value of the radial viscous stress, which must be balanced by the pressure. As a result, the values of \hat{v}' and \hat{p} across the shear layer increase as its thickness decreases, and become infinitely large when the limit of discontinuous profiles is approached. This singular behavior can be observed in the plots of \hat{v}' and \hat{p} shown in figure 3.1(d), with the value of \hat{v}' being significantly larger than that of \hat{p} , as corresponds to the relatively large value of the Reynolds number $Re = 50$ used in the calculation. The plot also includes as a dashed curve the radial variation of the quantity

$$\frac{2\bar{\mu}(r^j \hat{v})'}{r^j} + \left(\bar{\mu}_v - \frac{2\bar{\mu}}{3} \right) \left(k \hat{u} + \frac{(r^j \hat{v})'}{r^j} + \frac{m \hat{w}}{r^j} \right) + i Re \hat{p} - \frac{2j \bar{\rho} \hat{v}}{r^j} \int \frac{\bar{\mu}'}{\rho} dr, \quad (3.13)$$

which remains constant across the discontinuity, in agreement with (3.12f).

3.4 Stability eigenproblem with piecewise-constant base profiles

In regions where the base profiles are uniform, the disturbances of the low-Mach-number gas flow admit analytical solutions, which after imposition of appropriate boundary conditions, including those derived above for the surfaces of discontinuity, provide an equation for the dispersion relation, as shown below. The development begins by formulating the stability equations (3.1a)–(3.1c) in a simplified form that enables the solutions for the disturbances to be obtained sequentially. The eigenfunctions corresponding to symmetric base flows in an infinite domain are determined next, and are used in par-

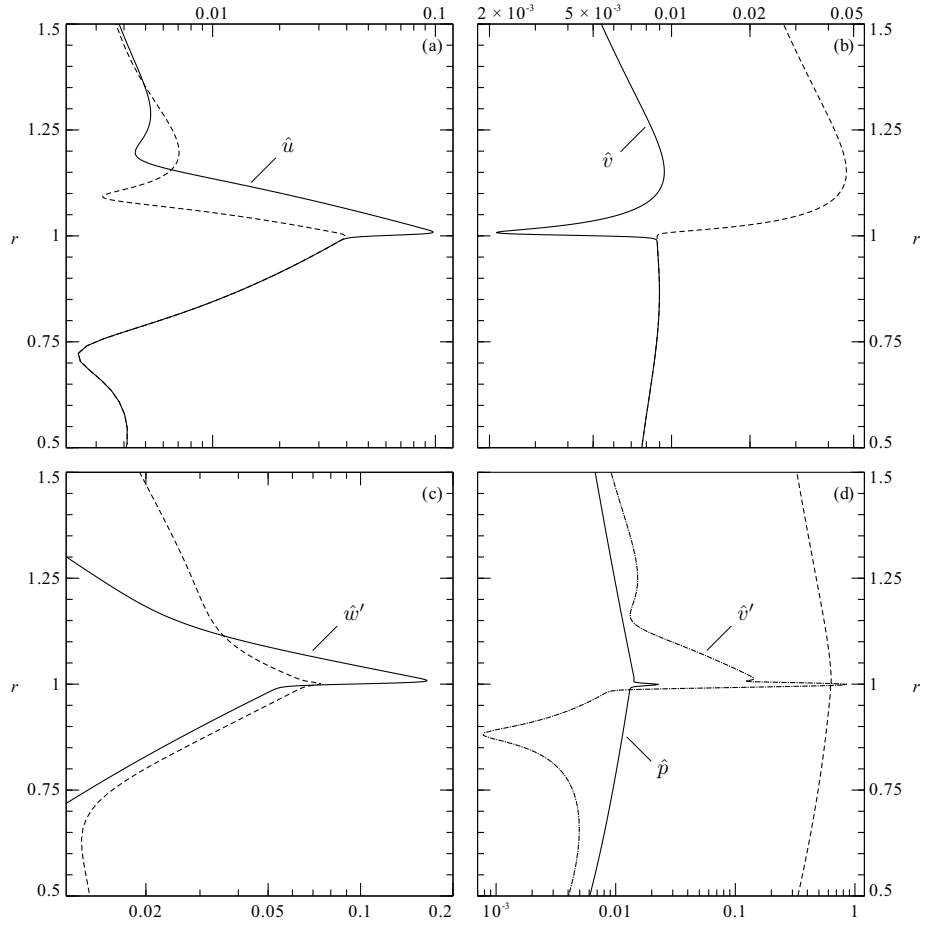


Figure 3.1: Eigenfunctions \hat{u} , \hat{v} , \hat{w}' , \hat{p} and \hat{v}' of the first helical instability mode $m = 1$ for the axisymmetric hyperbolic tangent base profiles (3.30) and (3.32) with $S = 0.2$, $R/\theta = 500$, $Re = 50$, $Pr = 0.7$ and $\sigma = 0.7$; the dashed curves represent, respectively, the functions $\hat{u} + \tilde{\kappa}\hat{T} \int [(U'\tilde{\mu}')/(\tilde{\mu}\tilde{\kappa}\hat{T}')] dr$, $\tilde{\rho}\hat{v}$, $\tilde{\mu}(\hat{w}/r^j)'$ and that defined in equation (3.13).

ticular to derive the dispersion relation corresponding to jets and wakes.

3.4.1 Stability equations for uniform base profiles

In the regions of constant base profiles, the linearized stability equations (3.1a)–(3.1c) can be simplified to

$$\frac{\partial \rho}{\partial t} + U \frac{\partial \rho}{\partial x} = -\bar{\rho} \nabla \cdot \mathbf{u}, \quad (3.14a)$$

$$\bar{\rho} \left(\frac{\partial \mathbf{u}}{\partial t} + U \frac{\partial \mathbf{u}}{\partial x} \right) = -\nabla p + \frac{1}{Re} \left[\bar{\mu} \nabla^2 \mathbf{u} + \left(\bar{\mu}_V + \frac{\bar{\mu}}{3} \right) \nabla (\nabla \cdot \mathbf{u}) \right], \quad (3.14b)$$

$$\bar{\rho} \left(\frac{\partial \rho}{\partial t} + U \frac{\partial \rho}{\partial x} \right) = \frac{1}{Re Pr} \bar{\kappa} \nabla^2 \rho. \quad (3.14c)$$

The energy equation (3.14c), which has been written for the density with use made of an equation of state $T(\rho)$, becomes, in normal modes,

$$\hat{\nabla}_{\gamma, m}^2 \hat{\rho} = 0, \quad (3.15)$$

in terms of the Laplacian operator defined in (3.4) with γ given in (3.5b). An equation for $\hat{\rho}$ can be obtained by taking the divergence of the momentum equation (3.14b) and using the continuity equation (3.14a) together with (3.15) to give

$$\hat{\nabla}_{k, m}^2 \hat{\rho} = (kU - \omega)^2 \left[\bar{\kappa}^{-1} \left(\bar{\mu}_V + 4\bar{\mu}/3 \right) Pr - 1 \right] \hat{\rho}. \quad (3.16)$$

On the other hand, substituting $\nabla \cdot \mathbf{u}$ from the continuity equation (3.14a) in the momentum equation (3.14b) yields

$$\hat{\nabla}_{\beta, m}^2 \hat{u} = \frac{iRek}{\bar{\mu}} \hat{\rho} - \frac{k(kU - \omega)}{\bar{\rho}} \left(\frac{1}{3} + \frac{\bar{\mu}_V}{\bar{\mu}} \right) \hat{\rho}, \quad (3.17a)$$

$$\hat{\nabla}_{\beta, m}^2 \hat{v} - \frac{j}{r^2} (\hat{v} + 2m\hat{w}) = -\frac{iRe}{\bar{\mu}} \hat{\rho}' + \frac{kU - \omega}{\bar{\rho}} \left(\frac{1}{3} + \frac{\bar{\mu}_V}{\bar{\mu}} \right) \hat{\rho}', \quad (3.17b)$$

$$\hat{\nabla}_{\beta, m}^2 \hat{w} - \frac{j}{r^2} (\hat{w} + 2m\hat{v}) = \frac{iRem}{r^j \bar{\mu}} \hat{\rho} - \frac{m(kU - \omega)}{r^j \bar{\rho}} \left(\frac{1}{3} + \frac{\bar{\mu}_V}{\bar{\mu}} \right) \hat{\rho}. \quad (3.17c)$$

where β is defined in (3.5a). For $j = 1$, it is useful to add and subtract the latter two equations (3.17b) and (3.17c), yielding

$$\hat{\nabla}_{\beta, m+j}^2 (\hat{v} + \hat{w}) = -\frac{iRe}{\bar{\mu}} \left(\hat{\rho}' - \frac{m}{r^j} \hat{\rho} \right) + \frac{kU - \omega}{\bar{\rho}} \left(\frac{1}{3} + \frac{\bar{\mu}_V}{\bar{\mu}} \right) \left(\hat{\rho}' - \frac{m}{r^j} \hat{\rho} \right), \quad (3.18a)$$

$$\hat{\nabla}_{\beta, m-j}^2 (\hat{v} - \hat{w}) = -\frac{iRe}{\bar{\mu}} \left(\hat{\rho}' + \frac{m}{r^j} \hat{\rho} \right) + \frac{kU - \omega}{\bar{\rho}} \left(\frac{1}{3} + \frac{\bar{\mu}_V}{\bar{\mu}} \right) \left(\hat{\rho}' + \frac{m}{r^j} \hat{\rho} \right). \quad (3.18b)$$

3.4.2 Jets and wakes with symmetric base profiles

Equations (3.15)–(3.17c) for $j = 0$ and (3.15)–(3.17a) and (3.18a)–(3.18b) for $j = 1$ enable the eigenfunctions of the disturbances to be determined sequentially. We consider in the following the solutions that exist when the base flow is planar and symmetric about the centerline $r = 0$ or axisymmetric around the axis $r = 0$, which includes the case of planar and cylindrical jets and wakes. The stability of a planar mixing layer, treated by Drazin (1961), could also be readily derived following the procedure given below but it is not specifically addressed here.

Two different regions of constant base profiles, denoted by I and II, are assumed to exist. The inner region I, centered at $r = 0$, has a radius a^* , used as scale for the problem, and is surrounded by a second region II of uniform base flow that extends radially to infinity. The properties of the inner region are used as scales for the different variables, except for the velocity, which is made nondimensional with use made of the average velocity between the two uniform streams $(u_I^* + u_{II}^*)/2$, so that the dimensionless base flow is given by

$$\begin{cases} U = 1 + \Lambda, \bar{\rho} = \bar{\mu} = \bar{\kappa} = 1, \bar{\mu}_V = \mu_{V_I} & \text{for } |r| < 1, \\ U = 1 - \Lambda, \bar{\rho} = 1/S, \bar{\mu} = M, \bar{\kappa} = K, \bar{\mu}_V = \mu_{V_{II}} & \text{for } |r| > 1, \end{cases} \quad (3.19)$$

where $\Lambda = (u_I^* - u_{II}^*)/(u_I^* + u_{II}^*)$, $S = \rho_I^*/\rho_{II}^*$, $K = \kappa_{II}^*/\kappa_I^*$, $M = \mu_{II}^*/\mu_I^*$, $\mu_{V_I} = \mu_{V_I}^*/\mu_I^*$ and $\mu_{V_{II}} = \mu_{V_{II}}^*/\mu_I^*$.

Solving the equations for $\hat{\rho}$, \hat{p} , \hat{u} , \hat{v} and \hat{w} in region I and imposing the boundary conditions (3.6) and (3.7) for $j = 0$ and (3.6) and (3.8) for $j = 1$ gives

$$\hat{\rho} = A \mathcal{F}_{\gamma_1, m}^s, \quad (3.20a)$$

$$\hat{p} = C \mathcal{F}_{k, m}^s - \frac{Ai[k(1 + \Lambda) - \omega]}{Re} \left(\mu_{V_I} + \frac{4}{3} - \frac{1}{Pr} \right) \mathcal{F}_{\gamma_1, m}^s, \quad (3.20b)$$

$$\hat{u} = E \mathcal{F}_{\beta_1, m}^s - \frac{Ck}{k(1 + \Lambda) - \omega} \mathcal{F}_{k, m}^s - \frac{Aik}{RePr} \mathcal{F}_{\gamma_1, m}^s, \quad (3.20c)$$

$$\hat{v} = \frac{1}{2} (G^+ \mathcal{F}_{\beta_1, m+j}^{-s} + G^- \mathcal{F}_{\beta_1, m-j}^{-s}) + \frac{C\bar{k}}{k(1 + \Lambda) - \omega} \dot{\mathcal{F}}_{k, m}^s + \frac{Ai\tilde{\gamma}_I}{RePr} \dot{\mathcal{F}}_{\gamma_1, m}^s, \quad (3.20d)$$

$$\hat{w} = \frac{1}{2} (G^+ \mathcal{F}_{\beta_1, m+j}^s - G^- \mathcal{F}_{\beta_1, m-j}^s) - \frac{Cm}{[k(1 + \Lambda) - \omega]rj} \mathcal{F}_{k, m}^s - \frac{Aim}{RePr rj} \mathcal{F}_{\gamma_1, m}^s, \quad (3.20e)$$

whereas the corresponding solution in region II reduces to

$$\hat{\rho} = B\mathcal{G}_{\gamma_{\text{II}},m}, \quad (3.21a)$$

$$\hat{p} = D\mathcal{G}_{k,m} - \frac{\text{Bi}S[k(1-\Lambda) - \omega]}{\text{Re}} \left(\mu_{\text{VII}} + \frac{4}{3}M - \frac{K}{\text{Pr}} \right) \mathcal{G}_{\gamma_{\text{II}},m}, \quad (3.21b)$$

$$\hat{u} = F\mathcal{G}_{\beta_{\text{II}},m} - \frac{DSk}{k(1-\Lambda) - \omega} \mathcal{G}_{k,m} - \frac{\text{Bi}KS^2k}{\text{RePr}} \mathcal{G}_{\gamma_{\text{II}},m}, \quad (3.21c)$$

$$\hat{v} = \frac{1}{2} (H^+ \mathcal{G}_{\beta_{\text{II}},m+j} + H^- \mathcal{G}_{\beta_{\text{II}},m-j}) + \frac{DS\tilde{k}}{k(1-\Lambda) - \omega} \dot{\mathcal{G}}_{k,m} + \frac{\text{Bi}KS^2\tilde{\gamma}_{\text{II}}}{\text{RePr}} \dot{\mathcal{G}}_{\gamma_{\text{II}},m}, \quad (3.21d)$$

$$\hat{w} = \frac{1}{2} (H^+ \mathcal{G}_{\beta_{\text{II}},m+j} - H^- \mathcal{G}_{\beta_{\text{II}},m-j}) - \frac{DSm}{[k(1-\Lambda) - \omega]r^j} \mathcal{G}_{k,m} - \frac{\text{Bi}KS^2m}{\text{RePr}r^j} \mathcal{G}_{\gamma_{\text{II}},m}. \quad (3.21e)$$

In the formulation,

$$\mathcal{F}_{\phi,m}^s = \begin{cases} e^{\sqrt{\phi^2+m^2}r} - se^{-\sqrt{\phi^2+m^2}r} & (j=0), \\ I_m(\phi r) & (j=1), \end{cases} \quad (3.22)$$

$$\mathcal{G}_{\phi,m} = \begin{cases} e^{-\sqrt{\phi^2+m^2}r} & (j=0), \\ K_m(\phi r) & (j=1), \end{cases} \quad (3.23)$$

where ϕ takes the values $\phi = k, \beta_{\text{I}}, \beta_{\text{II}}, \gamma_{\text{I}}, \gamma_{\text{II}}$, and I_m and K_m represent the modified Bessel functions of order m . Note that the dots in (3.20d) and (3.21d) indicate derivatives with respect to the argument of the function. In the formulation,

$$\beta_{\text{I}} = \sqrt{k^2 + i\text{Re}[k(1+\Lambda) - \omega]}, \quad \beta_{\text{II}} = \sqrt{k^2 + i\text{Re}[k(1-\Lambda) - \omega]/(SM)}, \quad (3.24)$$

$$\gamma_{\text{I}} = \sqrt{k^2 + i\text{RePr}[k(1+\Lambda) - \omega]}, \quad \gamma_{\text{II}} = \sqrt{k^2 + i\text{RePr}[k(1-\Lambda) - \omega]/(SK)}, \quad (3.25)$$

and

$$\tilde{k} = \sqrt{k^2 + (1-j)m^2}, \quad \tilde{\gamma}_{\text{I}} = \sqrt{\gamma_{\text{I}}^2 + (1-j)m^2}, \quad \tilde{\gamma}_{\text{II}} = \sqrt{\gamma_{\text{II}}^2 + (1-j)m^2}. \quad (3.26)$$

Evaluating the continuity equation (3.14a) with use made of (3.20a)–(3.21e) gives

$$kE + \beta_{\text{I}}(G^+ + G^-)/2 = 0, \quad (3.27)$$

$$kF - \beta_{\text{II}}(H^+ + H^-)/2 = 0. \quad (3.28)$$

Substituting (3.20a)–(3.21e) into the jump conditions (3.12a)–(3.12h) and using (3.27) and (3.28) to eliminate E and F provides a system of eight homogeneous linear equations for $(A, B, C, D, G^-, G^+, H^-, H^+)$. Non-trivial solutions exist if the determinant

of the associated coefficient matrix \mathbf{M} equals zero, thereby yielding the desired dispersion relation between ω and k in terms of the different parameters of the problem. The coefficient matrix can be simplified by eliminating terms through appropriate row and column linear combinations. The non-zero elements of the resulting simplified coefficient matrix \mathbf{M} are given in the Appendix. In the development, the power law

$$\bar{\mu} = \bar{\kappa} = \bar{T}^\sigma \quad (3.29)$$

is assumed for the temperature dependence of the shear layer viscosity and thermal conductivity, where the exponent σ typically takes the value $\sigma = 0.7$ for air.

3.5 Application to the stability of non-isothermal jets and wakes

To illustrate the use of the formalism introduced in §3.4, let us consider its application to the study of the viscous stability properties of unbounded non-isothermal two-dimensional and axisymmetric jets and wakes in the limit of vanishingly thin shear layers. More precisely, let u_I^* , T_I^* , ρ_I^* , μ_I^* , $\mu_{V_I}^*$ and κ_I^* be the velocity, temperature, density, dynamic viscosity, bulk viscosity and thermal conductivity at $r^* = 0$, and u_{II}^* , T_{II}^* , ρ_{II}^* , μ_{II}^* , $\mu_{V_{II}}^*$ and κ_{II}^* their corresponding values for $r^* \rightarrow \infty$. Hereafter, we will assume the gas to obey the isobaric equation of state $\rho^* T^* = \text{const.}$, and the physical properties to depend on the temperature through appropriate constitutive equations, $\mu^*(T^*)$, $\mu_V^*(T^*)$, $\kappa^*(T^*)$. Then, let a^* be the jet or wake radius, i.e. the characteristic transverse coordinate at which the local velocity and temperature profiles, u^* , T^* change values of the order of $|u_I^* - u_{II}^*|$ and $|T_I^* - T_{II}^*|$, respectively, and δ^* be the characteristic thickness of these velocity and temperature transition layers. Taking a^* , $u_m^* = (u_I^* + u_{II}^*)/2$ and T_I^* as characteristic length, velocity and temperature scales, the parallel base flow is uniquely determined by the velocity ratio, $\Lambda = (u_I^* - u_{II}^*)/(u_I^* + u_{II}^*)$, the density ratio $S = \rho_I^*/\rho_{II}^*$ and a dimensionless measure of the shear-layer thickness, $\delta = \delta^*/a^*$, together with a pair of dimensionless functions of the transverse coordinate $r = r^*/a^*$, describing the profiles of base-flow velocity, $U(r)$, and temperature, $\bar{T}(r)$. The transverse profiles of density and of the remaining physical properties are then given by the isobaric equation of state, $\bar{\rho} = 1/\bar{T}$, and the constitutive equations $\bar{\mu}(\bar{T})$, $\bar{\mu}_V(\bar{T})$ and $\bar{\kappa}(\bar{T})$.

Notice that we have also assumed that the velocity and temperature profiles share common transverse length scales a^* and δ^* as happens, for instance, in the near field of a mixing layer between two parallel streams. In this case, it is now well known that both length scales are relevant in determining the linear spatiotemporal instability proper-

ties of the flow, the normal modes being naturally divided into *shear layer* and *columnar* modes (Jendoubi & Strykowski, 1994; Lesshafft & Huerre, 2007; Juniper, 2007; Meliga *et al.*, 2008). The shear-layer modes have cut-off wavenumbers $k^* \sim 1/\delta^*$, characteristic frequencies $\omega^* \sim \delta^*/u_m^*$, and dominate the linear impulse response at group velocities $d\omega^*/dk^* \sim u_m^*$. In addition, their associated transverse eigenfunctions peak at the shear layer and decay rapidly away from it and are, thus, equivalent to the Kelvin-Helmholtz mode of a single shear layer. In contrast, columnar modes, of interest here, have characteristic wavenumbers $k^* \sim 1/a^*$, characteristic frequencies $\omega^* \sim a^*/u_m^*$, and dominate the linear impulse response for group velocities $d\omega^*/dk^* \ll u_m^*$. Moreover, the amplitude of their associated eigenfunctions is finite at the centerline and, therefore, do not have a counterpart in the case of a single shear layer.

As discussed by Drazin (1961), the formalism developed in §3.4 is expected to describe the stability properties of base flows with continuous profiles only in the case of wavelengths much larger than the shear-layer thickness, $k^*\delta^* \rightarrow 0$. This means, in particular, that the use of the discontinuous approximation is restricted to the study of the low wavenumber region of the spectrum of shear-layer modes, and is then useful to obtain approximations to the lower neutral curve, as Drazin (1961) did for the particular cases of the two-dimensional mixing layer and jet. Here, however, we are mainly interested in the study of columnar modes, for which the discontinuous approach is particularly useful, since in this case $k = k^*a^* \sim 1 \Rightarrow k^*\delta^* \sim \delta^*/a^* = \delta$. Thus, for finite values of both k and Re , the columnar eigenvalues obtained with continuous profiles are expected to converge uniformly to those associated with discontinuous profiles in the limit $\delta \rightarrow 0$.

To check the validity of the theory developed in §3.4 for discontinuous base profiles let us compare its predictions with calculations performed with two widely used parametric velocity profiles describing jets without outer coflow, $\Lambda = 1$, and which become planar and axisymmetric vortex sheets in the limit of vanishingly thin shear layers. Specifically, we will consider the axisymmetric hyperbolic tangent base profile, used for instance by Lesshafft & Huerre (2007),

$$U = 1 + \tanh \left[\frac{1}{4\theta} \left(\frac{1}{r} - r \right) \right], \quad (3.30)$$

and the planar hyperbolic sine profile, used by Yu & Monkewitz (1990),

$$U = \frac{2}{1 + \sinh^{2N} [r \operatorname{arcsinh}(1)]}. \quad (3.31)$$

In addition, following Lesshafft & Huerre (2007) and Yu & Monkewitz (1990), for the validation the temperature and density profiles will be obtained by using Crocco-Busemann's

relation together with the isobaric equation of state, written in the low-Mach-number forms

$$\tilde{T} = 1 + \frac{1-S}{2}(U-2) \quad \text{and} \quad \bar{\rho} = 1/\tilde{T}. \quad (3.32)$$

Note that the use of (3.32) together with (3.29) enables the integrals on the right-hand side of (3.12a) and (3.12e)–(3.12g) to be evaluated to give

$$\int_1^\Pi \frac{U' \bar{\mu}'}{\bar{\mu} \bar{\kappa} \tilde{T}'} dr = \frac{2(1-S^{-\sigma})}{1-S} \quad \text{and} \quad \int_1^\Pi \frac{\bar{\mu}'}{\bar{\rho}} dr = \frac{\sigma(S^{\sigma+1}-1)}{\sigma+1}. \quad (3.33)$$

The base profiles given by equations (3.30)–(3.32) depend on two parameters, namely the density ratio S , and a parameter characterizing the shear-layer thickness, which can be either the momentum thickness $\theta = \int_0^\infty (U/2)(1-U/2) dr$ in the axisymmetric jet of equation (3.30), or the parameter N used in the two-dimensional profile (3.31). Note that the limit of discontinuous profiles corresponds to $\theta \rightarrow 0$ and $N \rightarrow \infty$, and that N can be shown to be related with the momentum thickness of the plane shear layer through the simple expression $\theta \simeq 0.4011/N$, valid for $N \gtrsim 10$.

To solve the eigenvalue problem for continuous profiles, the stability equations (3.3a)–(3.3e) must be solved with the appropriate boundary conditions at $r = 0$ and as $r \rightarrow \infty$ discussed in section 3.2. To that end, we used a standard spectral collocation method similar to that employed by Lesshafft & Huerre (2007). Notice that, given the value of j specifying the planar or axial symmetry of the problem, equations (3.3a)–(3.3e) introduce (Re, Pr, σ, m, s) as additional parameters besides (S, θ) . Also of interest is that the parameter Re is based on the mean velocity u_m and, therefore, its value is half of that of the Reynolds number normally used for the case of a jet without coflow, which is based on the maximum jet velocity, $U = 2$.

3.5.1 Temporal stability analysis

To demonstrate that the limit of discontinuous base profiles is obtained as the shear-layer thickness decreases, let us begin by considering the unstable temporal stability branch of plane and axisymmetric jets without ambient coflow, $\Lambda = 1$, with a density ratio $S = 0.5$, for constant viscosity and thermal conductivity, $\sigma = 0$, as well as zero bulk viscosity $\bar{\mu}_V = 0$. The top and bottom rows of figure 3.2 display, respectively, the frequency, ω_r , and growth rate, ω_i , as functions of the real wavenumber k_r , for values of the parameters $N = (25, 50)$ and $1/\theta = (100, 200)$ (dashed and dash-dotted lines as indicated in the legend). Also shown as dotted curves are the corresponding results obtained with use made of the algebraic dispersion relation defined in the Appendix, obtained with the methodology described in §3.4 for discontinuous profiles. The left and right columns of figure 3.2 show results obtained for the sinuous mode of

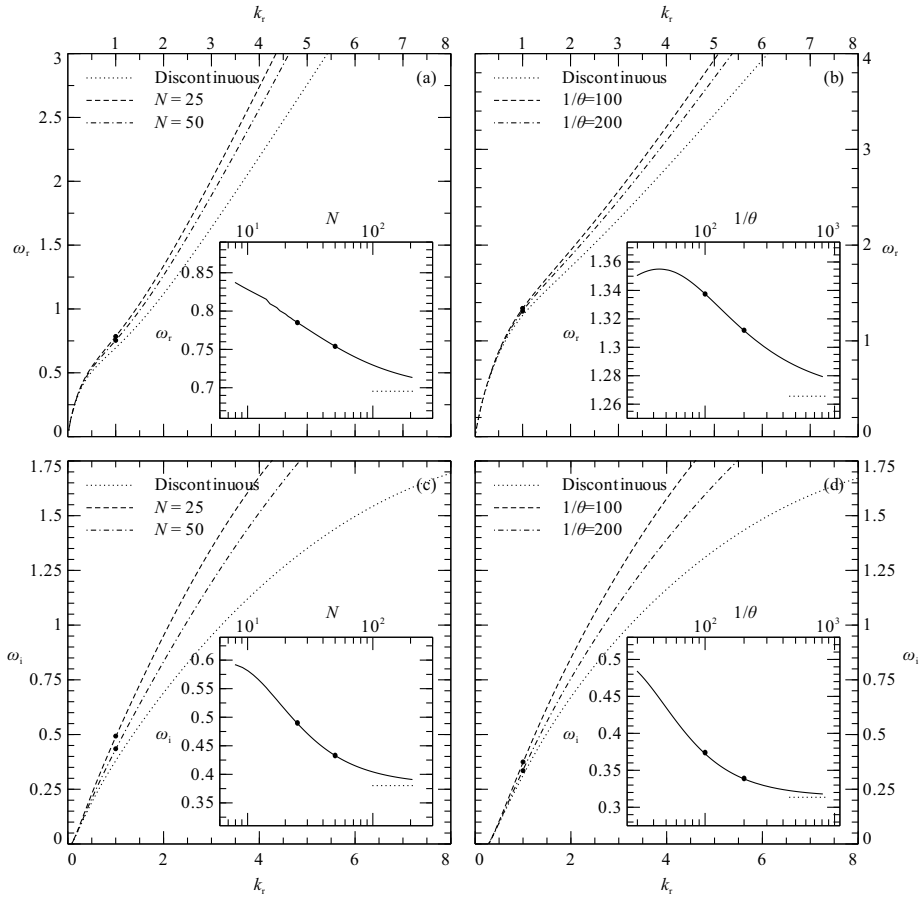


Figure 3.2: Real (upper row) and imaginary (bottom row) parts of the curves of temporal stability $\omega(k)$ calculated for the planar base profiles (3.31) and the varicose instability mode $m = 0, s = -1$ (left column), and for the axisymmetric profiles (3.30) and the axisymmetric instability mode $m = 0$ (right column), calculated for two values of the respective momentum thickness parameters N and θ (dashed and dash-dotted lines), together with their equivalents for discontinuous base profiles (dotted lines). In all the calculations values $Re = 50, S = 0.5, Pr = 1$ and $\sigma = 0$ were used. Insets: evolution of the single eigenvalue $\omega(k = 1)$ as the thickness parameter is increased (solid lines), and comparison with its limiting value calculated with discontinuous base profiles (dotted line). The dots indicate corresponding points between the main plots and the insets.

the two-dimensional jet ($j = 0, m = 0, s = -1$), and for the axisymmetric mode of the axisymmetric jet ($j = 1, m = 0$), respectively. The results shown in the four panels of figure 3.2 are consistent with the behavior expected from the discontinuous approximation. In particular, the low wavenumber end of the temporal spectra obtained with continuous profiles, $\omega(k \rightarrow 0)$, is seen to converge to the discontinuous approximation, independently of the value of N or θ . Moreover, it is also observed that the upper limit of the range of wavenumbers which can be approximated with small relative errors by means of discontinuous profiles, increases as the shear-layer thickness decreases. For instance, notice in figure 3.2(c) that the value of ω_i obtained for the two-dimensional jet with $N = 25$ ($\theta \simeq 0.016$) is approximated by the corresponding piecewise-constant base flow, with small relative errors that are less than 15% for values of the wavenumber up to $k \simeq 0.5$. This upper limit increases to $k \simeq 1$ in the case of a thinner profile with $N = 50$ ($\theta \simeq 0.008$). To illustrate the convergence process more clearly, the insets displayed in figure 3.2 show the dependence on the shear-layer thickness of the single eigenvalue $\omega(k = 1)$, together with its limiting value obtained with use made of discontinuous base profiles (dotted line), the solid circles indicating corresponding points in each subfigure. Since dominant columnar modes have values of $k \sim O(1)$, the good convergence properties observed in all of the insets of figure 3.2 for $k = 1$ indicate that for thin shear layers their viscous stability properties can be studied in the vortex-sheet limit with fairly small errors.

3.5.2 Spatiotemporal stability analysis and A/C transition

A phenomenon of special interest in the study of parallel, variable density jets and wakes is the transition from convective (C) to absolute (A) instability. It is now well established that the global dynamics observed in these flows is closely related with the absolute or convective character of the instability associated with their underlying base profiles (see for instance Chomaz, 2005, and references therein). In the particular case of jets without coflow, $\Lambda = 1$, there exists a critical value of the density ratio S_c below which this transition takes place and which, in the case of the parametric base profiles given by equations (3.30) or (3.31), is a function of the thickness parameters θ or N , respectively.

We will show below that, in the limit of vanishingly thin shear layers, the use of the theory of discontinuous base profiles developed above allows the computation of the critical density ratio S_c at which the A/C transition occurs. With this aim, we calculated transition diagrams for the base profiles given by equations (3.30) and (3.31), different instability modes, and two values of the Reynolds number, carefully decreasing the thickness parameter θ or $1/N$ down to values small enough for the limit of discontinuous profiles to be achieved, while still being computationally manageable.

The A/C transition curves were obtained by following the most unstable normal

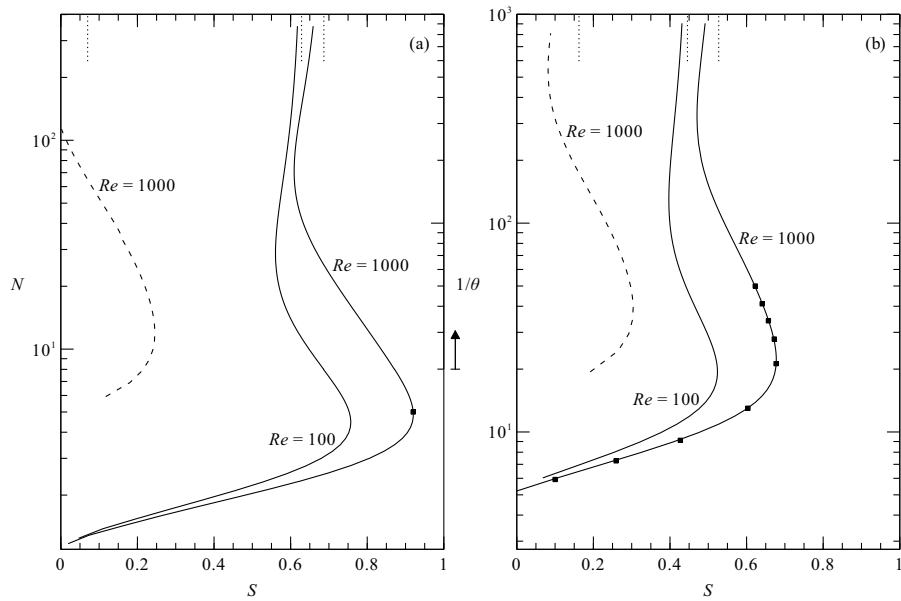


Figure 3.3: Transition curves between convective and absolute instability in the $(S, 1/\theta)$ and (S, N) planes for $Pr = 1$, $\sigma = 0$, and two different values of the Reynolds number $Re = (100, 1000)$. (a) Plane case with base profiles (3.31), (3.32) for the varicose mode $m = 0$, $s = -1$ (solid lines), and the sinuous mode $s = +1$ (dashed line). (b) Axisymmetric case with base profiles (3.30), (3.32) for the axisymmetric instability mode $m = 0$ (solid lines), and the first helical mode $m = 1$ (dashed line). The solid squares indicate the values calculated by Yu & Monkewitz (1990) (a) and Lesshafft & Huerre (2007) (b). The corresponding values of the critical density ratio obtained with the dispersion relation of the Appendix for discontinuous base profiles are indicated by the dotted lines.

mode $(k^{(0)}, \omega^{(0)})$ having zero group velocity, $d\omega/dk = 0$, and accomplishing the Briggs-Bers pinching criterion; see for instance Huerre (2000) for details. Negative values of the absolute growth rate, $\omega_i^{(0)} < 0$, are associated with a convective instability, while positive ones, $\omega_i^{(0)} > 0$, indicate an absolute instability. The transition curve $S_c(\theta)$ is then defined by the condition $\omega_i^{(0)}(S_c, \theta) = 0$, and can be easily tracked through a standard continuation method.

The results of these calculations are shown in figures 3.3(a) and 3.3(b), where the critical density ratio S_c is given as a function of the inverse thickness parameters N and $1/\theta$, for the planar and axisymmetric base profiles specified by (3.31) and (3.32), and by (3.30) and (3.32), respectively. The ticks along the right axis of figure 3.3(a) denote the values of the inverse momentum thickness $1/\theta > 20$ of the plane profile given by (3.31), computed from $1/\theta = N/0.4011$, with the corresponding scale being that of the left axis of figure 3.3(b). In the planar case of figure 3.3(a), both varicose modes, $s = +1$ (solid lines) and sinuous modes, $s = -1$ (dashed line) are considered, while the axisymmetric computations of figure 3.3(b) include the axisymmetric mode $m = 0$ (solid lines), as well as the first helical mode $m = 1$ (dashed line). The values of the critical density ratio obtained by using discontinuous base profiles are represented by the dotted lines. All calculations were performed using $Pr = 1$, $\sigma = 0$, and two different values of the Reynolds number, $Re = 100$ and $Re = 1000$, selected to enable comparisons to be made with results obtained by Lesshafft & Huerre (2007), indicated by the squares in figure 3.3(b). Similarly, in figure 3.3(a) the point $(N = 5, S = 0.92)$ corresponds to the transition conditions computed by Yu & Monkewitz (1990). The perfect agreement found in both cases provides further confidence on the accuracy of the numerical code used in the present work for continuous profiles.

Note that the transition curve shown in figure 3.3(b) for the axisymmetric mode and $Re = 1000$ (solid line) indicates in particular that the minimum value of $\theta = 1/50$ employed by Lesshafft & Huerre (2007) is not small enough to reproduce the limit of a vanishingly thin shear layer (dotted line). Thus, in order to study how this limit is approached, in the present work we have extended the computations with continuous base profiles to values of the momentum thickness as small as $\theta \simeq 10^{-3}$. The results reveal that for decreasing shear-layer thicknesses the convergence towards the vortex-sheet limiting values of $S(Re)$, i.e. the dotted lines in the figure, is faster for smaller values of Re . This finding seems to be in agreement with the approximations made in deriving the jump conditions (3.12a)–(3.12h), which in the limit of vanishing shear-layer thickness neglect the contributions of various integrals across the shear layer that are proportional to Re , appearing on the right-hand side of (3.9a)–(3.11c). For a given shear-layer thickness, the errors involved in using the vortex-sheet approximation therefore increase with the Reynolds number and lead to the slower convergence shown in figure 3.3. It is also worth remarking the non-monotonic behavior of the transition curves

as the shear-layer thickness decreases to values of $\theta < 1/50$, a range unexplored in the literature, which includes a pronounced decrease in S_c , followed by a minimum and an inflection point, before reaching the corresponding vortex-sheet limit $\theta \rightarrow 0$. This finite Reynolds number behavior is in marked contrast with its inviscid counterpart, whose corresponding curve $S_c(\theta)$ decreases monotonically towards the vortex-sheet limiting value $S_c(0)$ as θ decreases, giving negligible departures $S_c(\theta) - S_c(0)$ for values of the shear-layer thickness $\theta \lesssim 10^{-2}$ (see for instance Jendoubi & Strykowski, 1994; Lesshafft & Huerre, 2007; Coenen *et al.*, 2008).

It can be observed in figure 3.3(a) that the planar varicose mode $s = -1$ exhibits a qualitative behavior very similar to that of the axisymmetric mode $m = 0$ of figure 3.3(b), while the sinuous instability mode, $s = +1$, behaves as the planar counterpart of the first helical mode $m = 1$ of figure 3.3(b). Note, however, that the transition curve of the sinuous mode computed with continuous profiles (dashed line) disappears at a value of $N \simeq 100$. The transition curve can be anticipated to reappear at a larger value of N , to give a branch that approaches $S_c \simeq 0.07$ as $N \rightarrow \infty$, but the numerical computations were not extended to cases with sufficiently small shear-layer thickness to ascertain this asymptotic behavior. It is noteworthy that in the particular case $N = 1$, which corresponds to the Bickley jet profile, the varicose mode happens to be convectively unstable at all density ratios for large but finite values of the Reynolds number, in contrast with the inviscid result $S_c \simeq 0.145$ recently obtained by Ravier *et al.* (2006).

A compact way to summarize the spatiotemporal stability properties of jets and wakes consists in plotting for a fixed value of Re the regions of convective and absolute instability in the parameter plane (Λ, S) spanned by the velocity ratio and the density ratio. Note that the value of the velocity ratio is such that $\Lambda < -1$ corresponds to wakes with negative centerline velocity, $-1 < \Lambda < 0$ to wakes with positive centerline velocity, $0 < \Lambda < 1$ to jets in outer coflow, and $\Lambda > 1$ to jets with outer counterflow. This result is shown in figure 3.4, computed with the viscous dispersion relation obtained in §3.4 for discontinuous base profiles, in the particular case of constant viscosity and thermal conductivity, $\sigma = 0$, a Prandtl number $Pr = 1$, and two different values of the Reynolds number, $Re = 1000$ (top row) and $Re = 50$ (bottom row). The results shown in figures 3.4(a) and 3.4(c) correspond to two-dimensional modes, $m = 0$, in a planar geometry, $j = 0$, while those shown in figures 3.4(b) and 3.4(d) correspond to the axisymmetric case, $j = 1$. Figures 3.4(a) and 3.4(b) represent a generalization to the case of viscous perturbations of the corresponding inviscid results, previously obtained by Yu & Monkewitz (1990) and Juniper (2007) in the planar case, and Juniper (2008) in the axisymmetric case.

The (Λ, S) plane is divided into two regions depending on the instability being either convective (unshaded region) or absolute (shaded region). In the latter case, the light gray region corresponds to absolute instability of either the varicose mode [fig-

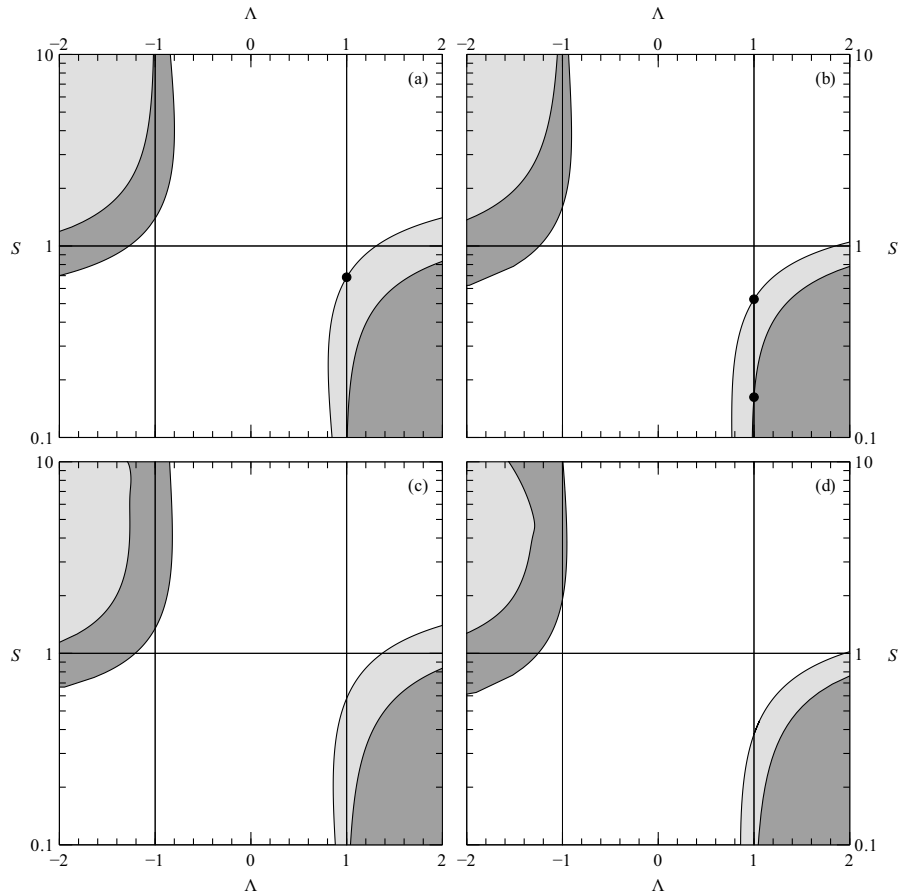


Figure 3.4: Regions of absolute and convective instability in the (Λ, S) parameter plane for (a) $j = 0, Re = 1000$, (b) $j = 1, Re = 1000$, (c) $j = 0, Re = 50$ and (d) $j = 1, Re = 50$. All the results are computed for $Pr = 1, \sigma = 0$. The filled regions indicate the existence of an absolute instability in the varicose ($j = 0, s = -1$) or axisymmetric ($j = 1, m = 0$) mode (light gray), and in the sinuous ($j = 0, s = 1$) or helical ($j = 1, m = 1$) mode (dark gray). The circles in (a) and (b) indicate the critical density ratios for the case of a jet without coflow, $\Lambda = 1$, corresponding to the asymptotes shown as dotted lines in figure 3.3.

ures 3.4(a) and 3.4(c)] or the axisymmetric mode [figures 3.4(b) and 3.4(d)], while inside the dark gray region either the sinuous [figures 3.4(a) and 3.4(c)] or the first helical mode $m = 1$ [figures 3.4(b) and 3.4(d)] are absolutely unstable. The qualitative features of these transition diagrams are the same as those observed in the inviscid stability analyzes previously presented in the literature. Thus, varicose/axisymmetric modes are seen to be dominant in jets, since they span a larger region of the $(\Lambda > 0, S)$ semi-plane; this mode becomes absolutely unstable when the density ratio is below a certain critical value which depends on the magnitude of the outer coflow or counterflow, $S < S_c(\Lambda; Re)$. One interesting result is the critical density ratio of the jet in the absence of coflow, which, for $Re = (1000, 50)$, takes values $S_c \simeq (0.687, 0.584)$ and $S_c \simeq (0.527, 0.378)$ in the planar and axisymmetric cases, respectively. Note that the values $(0.687, 0.527)$ for $Re = 1000$ correspond to the dotted lines in figures 3.3(a) and 3.3(b), respectively. Another result worth mentioning is the critical counterflow necessary for the instability to be absolute at constant density, $S = 1$, which, for $Re = (1000, 50)$, is given by $\Lambda_c = (1.308, 1.371)$ and $\Lambda_c = (1.861, 1.951)$ in planar and axisymmetric geometries, respectively. Sinuous/helical modes have smaller critical density ratios in jets than varicose/axisymmetric modes, independently of Λ .

Yu & Monkewitz (1990) pointed out the existence of a remarkable transformation, $(s, \Lambda, S) \rightarrow (-s, -\Lambda, S^{-1})$, under which the inviscid counterpart of our viscous dispersion relation for a planar geometry remains invariant. The results of figure 3.4 show that this invariance, by which the inviscid stability properties of the varicose mode of light jets coincide with those associated to the sinuous mode of heavy wakes, is lost in the presence of a finite viscosity. Note, however, that the departures from symmetry are very small at high Reynolds numbers, as can be seen in figures 3.4(a) and 3.4(c) for $Re = 1000$ and 50 , respectively. Indeed, the critical density ratio for the sinuous mode of plane wakes with zero centerline velocity, $\Lambda = -1$ takes values $S_c \simeq (1.394, 1.349)$ for $Re = (1000, 50)$. In the axisymmetric case the symmetry property does not apply under inviscid perturbations, and figures 3.4(b) and 3.4(d) show that this is also the case at large but finite values of the Reynolds number. In particular, the helical mode $m = 1$ has critical density ratios $S_c \simeq (1.596, 1.907)$ for $\Lambda = -1$ and $Re = (1000, 50)$, while the corresponding critical counterflow for absolute instability at constant density, $S = 1$, is $\Lambda_c = (-1.240, -1.253)$.

Although the results in figure 3.4 were computed with $\sigma = 0$ and $Pr = 1$ to enable comparisons with the previously published inviscid results to be readily made, additional computations using the dispersion relation given in the Appendix were performed to evaluate the influence of the variation of the transport properties on the instability behavior. In particular, the variation of S_c with Pr for $\Lambda = 1$, $Re = 1000$, $j = 1$, $m = 0$ and $\sigma = 0$ was computed, giving a monotonic variation $0.503 \leq S_c \leq 0.530$ within the range $0.1 \leq Pr \leq 2$. Similarly, fixing the values of $\Lambda = 1$, $Re = 1000$ and $Pr = 1$, the

critical density ratio was seen to vary in the range $0.527 \leq S_c \leq 0.654$ for $0 \leq \sigma \leq 2$.

3.6 Conclusions

We have presented a simple methodology appropriate to study the viscous linear stability properties of variable-density parallel flows with very thin shear layers, which provides a natural generalization of the formalism originally developed by Drazin (1961) in which the thin shear layers are substituted by vortex sheets. This discontinuous representation of the base flow, as discussed by Drazin (1961), is useful to study modal solutions with wavelengths much larger than the characteristic shear-layer thickness. The methodology includes the use of successive integrations of the stability equations across the vortex sheet to derive the jump conditions that serve to match the solutions of the stability problem on both sides of the discontinuity. In particular, we have applied the formalism to the case of jets and wakes with symmetric base profiles, that, in the limit of very thin shear layers, can be represented by piecewise constant base profiles. Analytic solutions were found for the flow perturbations in the regions of constant velocity and density. Imposing the jump conditions across the discontinuity leads to a dispersion relation in the form of a closed algebraic expression that involves all the relevant parameters of the problem, which can easily be solved with a numerical root-finding method to study the linear stability properties of the flow.

To validate the dispersion relation obtained for jets and wakes with discontinuous base profiles, we have compared its solutions with stability calculations performed for continuous thin-shear-layer base profiles. In particular, we have used in the comparisons two different sets of base profiles, commonly used in the literature to model planar and axisymmetric jets and wakes. Figures 3.2 and 3.3 show that by decreasing the shear-layer thickness of the parametric continuous base profiles, we successfully recover the limit of discontinuous base profiles, both for temporal and spatiotemporal stability analyses.

In the formalism presented in this work we have considered the case of a gas of constant molecular weight for which the density and transport properties are functions of the temperature. The formulation could be readily extended to account for molecular weight variations by describing also the composition field, as discussed in the text above equation (3.2). In the case of an isothermal binary mixture of fluids, a situation frequently encountered in experiments and applications, the formulation is very simple, in that with uniform temperature the density variations can be computed in terms of the mass fraction of one of the two species, yielding for instance $\bar{\rho} = 1/[\bar{Y} + S(1 - \bar{Y})]$, with \bar{Y} denoting the base-flow mass fraction of the gas located near the axis (region I) and $S = \rho_1^*/\rho_{II}^*$ being the molecular-weight ratio for the binary

mixture. The analysis necessitates the introduction of minor modifications to the coefficient matrix displayed in the Appendix, as required to accommodate changes in the jump conditions (3.12d) and (3.12h), which should be replaced with $[\bar{\rho} \hat{Y}]_I^{\text{II}} = 0$ and $[\bar{\rho} \hat{Y}' + \bar{Y}' \hat{\rho} - i Re Sc \bar{Y} \bar{\rho} \hat{v}]_I^{\text{II}} = 0$, respectively, and also from changes in the eigenfunctions defined in equations (3.21b)–(3.21e) and (3.25), where the thermal conductivity ratio K should be replaced with S^{-1} . The resulting modified dispersion relation could be employed, for instance, to study the viscous stability characteristics of Helium jets discharging into air, a configuration often used in experiments as a prototypical model for light jets.

The development indicates that for gaseous jets with variable viscosity the vortex-sheet limit exhibits a non-negligible dependence on the specific shape of the shear-layer profiles of velocity and density through the integrals appearing on the right-hand-sides of (3.12a) and (3.12e)–(3.12g), giving a result similar to that found by Drazin (1962). This finding suggests that, even in configurations with thin shear layers, care should be exerted when using model base profiles as those given above in (3.30) and (3.31), for the quantitative assessment of the viscous instability of gaseous jets and wakes. For instance, if accurate results are desired in the stability analysis of hot gas jets emerging from short injectors, investigated in the inviscid limit by Coenen *et al.* (2008), then the computation should account for the Blasius velocity profile found near the injector wall, which would enter in the vortex-sheet limit through the integral contribution in (3.12a).

3.7 Appendix: The dispersion relation

The non-zero elements of the simplified coefficient matrix \mathbf{M} are

$$\begin{aligned}
M_{11} &= \mathcal{H}_{\gamma_1, m}^s & M_{12} &= \mathcal{I}_{\gamma_{II}, m} \\
M_{21} &= S\tilde{\gamma}_I & M_{22} &= \tilde{\gamma}_{II} \\
M_{23} &= (S-1)\tilde{k} & M_{25} &= (S-1)\tilde{\beta}_I \\
M_{26} &= -jm(S-1)\mathcal{H}_{\beta_1, m} \\
M_{31} &= iRePr\sigma Q_1 k \mathcal{H}_{\gamma_1, m}^s & M_{33} &= k^2 \mathcal{H}_{k, m}^s \\
M_{34} &= k^2 \mathcal{I}_{k, m} & M_{35} &= \beta_I \tilde{\beta}_I \mathcal{H}_{\beta_1, m}^s \\
M_{37} &= \beta_{II} \tilde{\beta}_{II} \mathcal{I}_{\beta_{II}, m} \\
M_{41} &= 2k\tilde{\gamma}_I(iRe\Lambda + \sigma Q_2 k) & M_{43} &= 2k\tilde{k}(iRe\Lambda + \sigma Q_2 k) \\
M_{45} &= \beta_I \tilde{\beta}_I^2 - k^2 \tilde{\beta}_I + 2k\tilde{\beta}_I(iRe\Lambda + \sigma Q_2 k) & M_{46} &= jm[k^2 - 2k(iRe\Lambda + \sigma Q_2 k)] \mathcal{H}_{\beta_1, m} \\
M_{47} &= S^\sigma(\beta_{II} \tilde{\beta}_{II}^2 - k^2 \tilde{\beta}_{II}) & M_{48} &= jS^\sigma m k^2 \mathcal{I}_{\beta_{II}, m} \\
M_{53} &= \tilde{k} & M_{54} &= \tilde{k} \\
M_{55} &= \tilde{\beta}_I & M_{56} &= -jm \mathcal{H}_{\beta_1, m} \\
M_{57} &= \tilde{\beta}_{II} & M_{58} &= -jm \mathcal{I}_{\beta_{II}, m} \\
M_{61} &= (\beta_I^2 + k^2 + 2m^2) \mathcal{H}_{\gamma_1, m}^s - 2j\sigma Q_2 \gamma_I \\
M_{62} &= S^\sigma(\beta_{II}^2 + k^2 + 2m^2) \mathcal{I}_{\gamma_{II}, m} \\
M_{63} &= (\beta_I^2 + k^2 + 2m^2) \mathcal{H}_{k, m}^s - 2j\sigma Q_2 k \\
M_{64} &= S^\sigma(\beta_{II}^2 + k^2 + 2m^2) \mathcal{I}_{k, m} \\
M_{65} &= [(\mu_{V_I} + \frac{4}{3})(\beta_I^2 + m^2) - (\mu_{V_I} - \frac{2}{3})(\beta_I \tilde{\beta}_I + jm^2)] \mathcal{H}_{\beta_1, m}^s - 2j\sigma Q_2 \beta_I \\
M_{66} &= m\{[(\mu_{V_I} - \frac{2}{3})(1-j)\tilde{\beta}_I + 2j\sigma Q_2] \mathcal{H}_{\beta_1, m} - 2j\beta_I\} \\
M_{67} &= [(\mu_{V_{II}} + \frac{4}{3}S^\sigma)(\beta_{II}^2 + m^2) - (\mu_{V_{II}} - \frac{2}{3}S^\sigma)(\beta_{II} \tilde{\beta}_{II} + jm^2)] \mathcal{I}_{\beta_{II}, m} \\
M_{68} &= m[(\mu_{V_{II}} - \frac{2}{3}S^\sigma)(1-j)\tilde{\beta}_{II} - 2jS^\sigma \beta_{II}] \\
M_{73} &= m \mathcal{H}_{k, m}^s & M_{74} &= m \mathcal{I}_{k, m} \\
M_{75} &= jm \mathcal{H}_{\beta_1, m} & M_{76} &= -[j + (1-j) \mathcal{H}_{\beta_1, m}^s] \tilde{\beta}_I \\
M_{77} &= jm \mathcal{I}_{\beta_{II}, m} & M_{78} &= -\tilde{\beta}_{II} \\
M_{81} &= 2m(j \mathcal{H}_{\gamma_1, m}^s - \sigma Q_2 \tilde{\gamma}_I) & M_{82} &= 2mjS^\sigma \mathcal{I}_{\gamma_{II}, m} \\
M_{83} &= 2m(j \mathcal{H}_{k, m}^s - \sigma Q_2 \tilde{k}) & M_{84} &= 2mjS^\sigma \mathcal{I}_{k, m} \\
M_{85} &= m[2j \mathcal{H}_{\beta_1, m} - (2\sigma Q_2 + j-1)\tilde{\beta}_I] & M_{86} &= \tilde{\beta}_I^2 [j \mathcal{H}_{\beta_1, m} + (1-j)] - 2j\beta_I + 2j\sigma Q_2 m^2 \mathcal{H}_{\beta_1, m} \\
M_{87} &= S^\sigma m [2j \mathcal{I}_{\beta_{II}, m} - (j-1)\tilde{\beta}_{II}] & M_{88} &= S^\sigma (\tilde{\beta}_{II}^2 \mathcal{I}_{\beta_{II}, m} - 2j\beta_{II})
\end{aligned}$$

where

$$\begin{aligned} \mathcal{H}_{\phi,m} &= \mathcal{F}_{\phi,m} / \dot{\mathcal{F}}_{\phi,m}, & \mathcal{I}_{\phi,m} &= \mathcal{G}_{\phi,m} / \dot{\mathcal{G}}_{\phi,m}, \\ \tilde{\beta}_I &= \sqrt{\beta_I^2 + (1-j)m^2}, & \tilde{\beta}_{II} &= \sqrt{\beta_{II}^2 + (1-j)m^2}, \end{aligned} \quad (3.34)$$

and

$$Q_1 = \int_I^{II} \bar{\rho}^{1+\sigma} U' dr \quad Q_2 = \int_I^{II} \bar{\rho}' / \bar{\rho}^{2+\sigma} dr \quad (3.35)$$

References

- BATCHELOR, G. K. & GILL, A. E. 1962 Analysis of the stability of axisymmetric jets. *J. Fluid Mech.* **14**, 529–551.
- CHOMAZ, J. M. 2005 Global instabilities in spatially developing flows: Non-normality and nonlinearity. *Ann. Rev. Fluid Mech.* **37**, 357–392.
- COENEN, W., SEVILLA, A. & SÁNCHEZ, A. 2008 Absolute instability of light jets emerging from circular injector tubes. *Phys. Fluids* **20**, 074104.
- DRAZIN, P. G. 1961 Discontinuous velocity profiles for the Orr-Sommerfeld equation. *J. Fluid Mech.* **10**, 571–583.
- DRAZIN, P. G. 1962 On stability of parallel flow of an incompressible fluid of variable density and viscosity. *Proc. Cambridge Philos. Soc.* **58**, 646–661.
- ESCH, R. E. 1957 The instability of a shear layer between two parallel streams. *J. Fluid Mech.* **3**, 289–303.
- HELMHOLTZ, H. VON 1868 Über discontinuirliche Flüssigkeitsbewegungen. *Monats. Königl. Preuss. Akad. Wiss. Berlin* **23**, 215–228.
- HUERRE, P. 2000 Open shear flow instabilities. In *Perspectives in fluid dynamics* (ed. G. Batchelor, K. Moffatt & G. Worster), pp. 159–229. Cambridge.
- HUERRE, P. & MONKEWITZ, P. A. 1985 Absolute and convective instabilities in free shear layers. *J. Fluid Mech.* **159**, 151–168.
- HUERRE, P. & MONKEWITZ, P. A. 1990 Local and global instabilities in spatially developing flows. *Annu. Rev. Fluid Mech.* **22**, 473–537.

- JENDOUBI, S. & STRYKOWSKI, P. J. 1994 Absolute and convective instability of axisymmetric jets with external flow. *Phys. Fluids* **6**, 3000–3009.
- JUNIPER, M. P. 2007 The full impulse response of two-dimensional jet/wake flows and implications for confinement. *J. Fluid Mech.* **590**, 163–185.
- JUNIPER, M. P. 2008 The effect of confinement on the stability of non-swirling round jet/wake flows. *J. Fluid Mech.* **605**, 227–252.
- KELVIN, LORD 1871 Hydrokinetic solutions and observations. *Phil Mag. (4)* **42**, 362–377.
- LESSHAFFT, L. & HUERRE, P. 2007 Linear impulse response in hot round jets. *Phys. Fluids* **19** (2), 024102.
- MELIGA, P., SIPP, D. & CHOMAZ, J.-M. 2008 Absolute instability in axisymmetric wakes: compressible and density variation effects. *J. Fluid Mech.* **600**, 373–401.
- MONKEWITZ, P. A. 1988 The absolute and convective nature of instability in two-dimensional wakes at low reynolds numbers. *Phys. Fluids* **31**, 999–1006.
- MONKEWITZ, P. A. & SOHN, K. D. 1988 Absolute instability in hot jets. *AIAA J.* **28**, 911–916.
- RAVIER, S., ABID, M., AMIELH, M. & ANSELMET, F. 2006 Direct numerical simulation of variable-density plane jets. *J. Fluid Mech.* **546**, 153–191.
- RAYLEIGH, LORD 1880 On the stability, or instability, of certain fluid motions. *Proc. London Math. Soc.* **11**, 57–70.
- TATSUMI, T. & GOTOH, K. 1960 Stability of free boundary layers between two streams. *J. Fluid Mech.* **7**, 433–441.
- TATSUMI, T. & KAKUTANI, T. 1958 The stability of a two-dimensional laminar jet. *J. Fluid Mech.* **4**, 261–275.
- YU, M.-H. & MONKEWITZ, P. A. 1990 The effect of nonuniform density on the absolute instability of two-dimensional inertial wakes and jets. *Phys. Fluids A* **2**, 611–639.

Viscous absolute instability of hot and light round jets near the outlet

The viscous spatiotemporal instability of low-density axisymmetric jets emerging from circular nozzles or tubes is studied in the limit of small Mach numbers and large Reynolds numbers. We consider separately the two particular cases of a hot gas jet discharging into a colder ambient of the same gas, as well as the isothermal discharge of a jet of gas with molecular weight smaller than that of the ambient gas. In both cases, we consider the detailed downstream evolution of the local stability properties in the near field of the jet. Realistic base flows are obtained by integrating the axisymmetric boundary layer equations. The local viscous stability properties of the resulting slender jets are then addressed with the aim at establishing the convective or absolute nature of the instability in the near field of hot or light jets. We discuss the relationship of our results with those obtained in previous works with use made of parametric velocity and density profiles, and compare both approaches with the actual global transition observed in experiments performed with hot and light jets.

4.1 Introduction

The classical theory of hydrodynamic stability of parallel flows has been successfully applied to explain many features of the large-scale dynamics observed in free shear flows such as mixing layers, jets and wakes (see the reviews by Ho & Huerre, 1985; Huerre & Monkewitz, 1990; Chomaz, 2005). The particular case of free submerged jets emerging from injectors like nozzles or tubes has been widely studied due to its central role in applications involving mixing, combustion and propulsion. In this context, it was early recognized that good agreement with experiments required the application of the spatial stability theory (Michalke, 1965), in which the linearized perturbation fields are decomposed into spatially growing waves with real frequency (see for instance Mattingly & Chang, 1974; Cohen & Wygnanski, 1987). It was also concluded from these works that good quantitative predictions require the use of realistic shapes for the local

velocity profiles used as basic flow in the stability analysis.

The experiments of Sreenivasan *et al.* (1989) and Kyle & Sreenivasan (1993) with isothermal jets of helium/air mixtures, as well as those by Monkewitz *et al.* (1990) and Raghu & Monkewitz (1991) with heated air jets, clearly showed that round jets with density sufficiently smaller than that of the ambient sustain intense self-excited oscillations consistent with the existence of a supercritical Hopf bifurcation at a certain critical value of the density ratio (see also Hallberg & Strykowski, 2006; Hallberg *et al.*, 2007). It is noteworthy that these experiments were motivated by the previous theoretical finding according to which parallel models of jets with thin shear layers become absolutely unstable when the jet to ambient density ratio S becomes smaller than a certain critical value S_c , due to the direct resonance of downstream and upstream propagating axisymmetric instability waves. Since in this case perturbations grow in the frame of reference of the nozzle, the spatial stability problem is ill-defined for $S < S_c$. In the case of an incompressible inviscid vortex sheet $S_c \simeq 0.66$ (Michalke, 1970; Huerre & Monkewitz, 1985), but its particular value is known to depend on other control parameters like the shear-layer thickness and the values of the Mach, Reynolds and Richardson numbers, being also strongly affected by the presence of ambient coflow or counterflow (Monkewitz & Sohn, 1988; Jendoubi & Strykowski, 1994; Sevilla *et al.*, 2002; Lesshafft & Huerre, 2007; Hallberg *et al.*, 2007; Nichols *et al.*, 2007; Coenen *et al.*, 2008; Srinivasan *et al.*, 2010).

It is important to emphasize that the downstream evolution of the jet determines the corresponding evolution of the local spatiotemporal instability characteristics. This fact, in turn, leads to different possibilities regarding the regions of absolute instability present in the jet, which are known to affect the actual behavior observed in the non-linear regime. Thus, for instance, the numerical simulations performed by Lesshafft *et al.* (2006, 2007) clearly show that the global mode, leading to the self-excited behavior of a hot jet, is destabilized whenever a pocket of absolute instability appears in the base flow *away from boundaries*. Moreover, at criticality, the corresponding global frequency coincides in this case with the value given by the local stability analysis at the station where the character of the instability changes from convective to absolute, in agreement with the theory of non-linear global modes developed by Pier *et al.* (1998) for weakly non-parallel flows. However, it was also shown by Lesshafft *et al.* (2006, 2007) that, in cases where the pocket of absolute instability includes the upstream boundary of the flow, the global mode is destabilized only if the absolutely unstable region is sufficiently large. In addition, in this case, the saturated frequency at criticality was found to be in good agreement with the real absolute frequency computed at the *inlet* of the domain.

Most of the previous studies on the spatiotemporal stability of low-density jets use parametric model velocity and density profiles, typically hyperbolic tangents, to represent the basic parallel jet flow (for instance Jendoubi & Strykowski, 1994; Sevilla *et al.*,

2002; Lesshafft & Huerre, 2007; Hallberg *et al.*, 2007; Nichols *et al.*, 2007; Srinivasan *et al.*, 2010). In this context, the question naturally arises as to what extent do these parametric representations of the jet account for the actual stability properties associated to realistic base flows. A recent effort to fill this gap is the work of Coenen *et al.* (2008), where the basic jet is obtained by solving the axisymmetric boundary layer equations to describe its downstream evolution from given initial profiles corresponding to circular injector tubes of finite length.

The results discussed above clearly imply that, in order to account for the synchronized behavior observed in low-density jets, the application of local spatiotemporal stability theory requires a careful consideration of its downstream evolution along the jet. Thus, the objective of the present chapter is to perform a detailed analysis of the viscous spatiotemporal stability properties in the near field of low-density laminar jets emerging from circular nozzles or tubes, with the aim at establishing the local convective or absolute nature of their linear instability near the outlet. To that end, we extend our previous inviscid study (Coenen *et al.*, 2008), by retaining viscous effects in the perturbations. The chapter is structured as follows. The formulation is presented in § 4.2. In § 4.3 we present and discuss the results obtained for the particular cases of heated and isothermal light jets. Finally, § 4.4 is devoted to the conclusions.

4.2 Formulation

We will consider two particular cases of low-density jets, corresponding to hot air jets discharging into stagnant air, as well as isothermal jets of nitrogen/helium mixtures discharging into a stagnant nitrogen atmosphere. Note that the latter model also serves, with small relative errors, to describe the much more common configuration in which an air/helium mixture discharges into stagnant air. We will assume here that the jet Reynolds number $Re = \rho_j U_j a / \mu_j \gg 1$, the Mach number $Ma = U_j / c_0 \ll 1$, and the Richardson number $Ri = (\rho_\infty - \rho_j) g a / (\rho_j U_j^2) \ll 1$, where the index j indicates properties evaluated for the jet fluid at the exit. We will therefore consider the limit of negligible buoyancy and compressibility effects, and the basic jet flow can then be obtained, with small relative errors of order Re^{-2} , by means of the axisymmetric boundary layer equations presented in chapter 1. Specifically, the basic hot jet was computed by integrating equations (1.2)–(1.4), together with the power-law constitutive equations (1.5)–(1.6) and the appropriate boundary conditions, while the basic light jet was obtained by integrating equations (1.2), (1.3) and (1.10) together with the constitutive equations (1.9)–(1.13) and the appropriate boundary conditions. The finite difference method described in appendix A.1 was used to obtain all the results presented here.

The boundary condition at the jet exit was specified by solving the boundary layer

equations describing the isothermal flow inside a circular injector tube of length l_t and uniform inlet velocity, as explained in detail in chapter 2. The corresponding initial velocity profile $U_e(r)$ is then uniquely specified by the value of the scaled injector length, $L_t = l_t/(Re_j a)$ or, alternatively, by the value of the initial dimensionless momentum thickness $\theta_0/a = \int_0^\infty U/U_a(1 - U/U_a) dr$, where $U_a = U_e(0)$ is the centerline velocity at the exit. To facilitate comparisons with previous numerical and experimental works, throughout this chapter we will use the parameter θ_0/D , where $D = 2a$ is the injector diameter, to specify the initial condition. Note that the function $L_t(\theta_0/a)$ represented in figure 2.5 of chapter 2 may be used to transform the values of both variables. In the limit of short injector tubes, $L_t \rightarrow 0$, the exit velocity profile consists of a uniform core with velocity $U_a = 1 + O(L_t^{1/2})$, surrounded by a thin annular boundary layer with Blasius profile and momentum thickness $\theta_0/a = 0.6641 L_t^{1/2}$, and can also be used to describe jets discharging from nozzles.

It will be shown below that the absolute instability normally takes place within the near field of the jet at values of x for which the basic flow defined by equations (1.2)–(1.4) or (1.2), (1.3) and (1.10) in the case of hot and light jets, respectively, admits simplified self-similar descriptions. In the limit $L_t \ll 1$, the boundary layer at the injector wall, of initial dimensional momentum thickness θ_0 , develops downstream in a self-similar Goldstein layer which grows with axial distance as $\delta_G \sim (\nu/A)^{1/3} \hat{x}^{1/3}$, where $A \sim U_j/\theta_0$ is the characteristic vorticity of the initial boundary layer and \hat{x} is the dimensional downstream coordinate. The characteristic axial distance \hat{x}_G within which the initial boundary layer undergoes viscous relaxation is given by the condition $\delta_G \sim \theta_0$, giving $\hat{x}_G \sim \theta_0^3 A/\nu \sim \theta_0^2 U_j/\nu$. The jet has uniform velocity profile U_j downstream of the Goldstein wake, and interacts with the stagnant ambient through a mixing layer which grows downstream as $\delta_{ML} \sim (\nu/U_j)^{1/2} \hat{x}^{1/2}$, and which admits also a self-similar description whenever $\delta_{ML} \ll a$, giving $\hat{x} \ll U_j a^2/\nu$ as the corresponding region of validity. Note that, in terms of the dimensionless variables of the problem, the characteristic length of the Goldstein wake is $x_G \sim (\theta/a)^2$, while the mixing layer description is valid in the region $x_G \ll x \ll 1$.

These considerations imply that in the region $(\theta_0/a)^2 \ll x \ll 1$, the self-similar mixing region can be obtained, at leading order, in terms of the stream function $\psi = x^{1/2}F(\eta)$, defined such that $\rho u = \psi_r = F_\eta$ and $\rho v = -\psi_x = x^{-1/2}(\eta F_\eta - F)/2$, where $\eta = (r-1)/x^{1/2}$ is the similarity variable, and the subscripts indicate derivatives with respect to η . In the case of a hot jet, the functions $F(\eta)$, $T(\eta)$ solve the system $(T^\sigma(TF_\eta))_\eta + F/2(TF_\eta)_\eta = 0$ and $(T^\sigma T_\eta)_\eta + Pr/2FT_\eta = 0$ with boundary conditions $F_\eta - 1 = F - \eta = T - 1 = 0$ for $\eta \rightarrow -\infty$, and $F_\eta = T - S = 0$ for $\eta \rightarrow \infty$. Similarly, for the light jet the equations for the functions $F(\eta)$, $Y(\eta)$ are $(\mu(F_\eta/\rho))_\eta + F/2(F_\eta/\rho)_\eta = 0$ and $(\rho Y_\eta)_\eta + Sc/2FY_\eta = 0$ with boundary conditions $F_\eta/\rho - 1 = F - \eta = Y - Y_j = 0$ for $\eta \rightarrow -\infty$, and $F_\eta/\rho = Y = 0$ for $\eta \rightarrow \infty$, where the viscosity and density functions

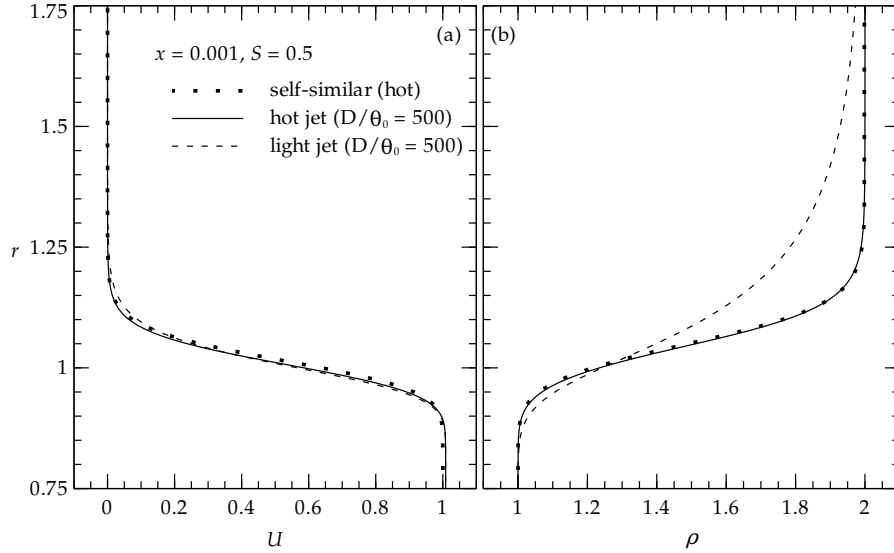


Figure 4.1: The dimensionless radial profiles of (a) velocity and (b) density for a hot jet with $Pr = \sigma = 0.7$ (solid line) and a light jet of a nitrogen/helium mixture discharging into nitrogen (dashed line) at $x = 10^{-3}$, for a density ratio $S = 0.5$, and an initial momentum thickness $D/\theta_0 = 500$. The bold dotted line represents the self-similar mixing layer solution for the hot jet.

$\mu(Y)$, $\rho(Y)$ are given in chapter 1 as equations 1.13 and 1.9, respectively.

The local spatiotemporal stability of the basic axisymmetric hot or light jet flows discussed above was studied by solving the linearized stability equations presented in chapter 1. The spectral collocation method described in appendix A.2, in combination with Deissler's method for the computation of saddle points, described in appendix A.3, were then used to obtain the most unstable normal mode (k_0, ω_0) with zero group velocity, $d\omega/dk = 0$, and accomplishing the Briggs-Bers pinching criterion. The downstream evolution of the absolute growth rate, $\omega_{i,0}(x; S, Re, D/\theta_0)$, was then obtained, allowing us to quantitatively characterize the different regions where a pocket of absolute instability exists in the $(S, Re, D/\theta_0)$ parameter space.

4.3 Results

Let us begin by showing the difference between the basic flows obtained for hot and light jets in their respective near fields. Figure 4.1 shows the radial profiles of (a) velocity and (b) density obtained by integrating the boundary layer equations (1.2)–(1.4) for a hot jet with $Pr = \sigma = 0.7$ (solid line) and the boundary layer equations (1.2), (1.3) and (1.10) for an isothermal nitrogen/helium jet discharging into nitrogen (dashed line), at $x =$

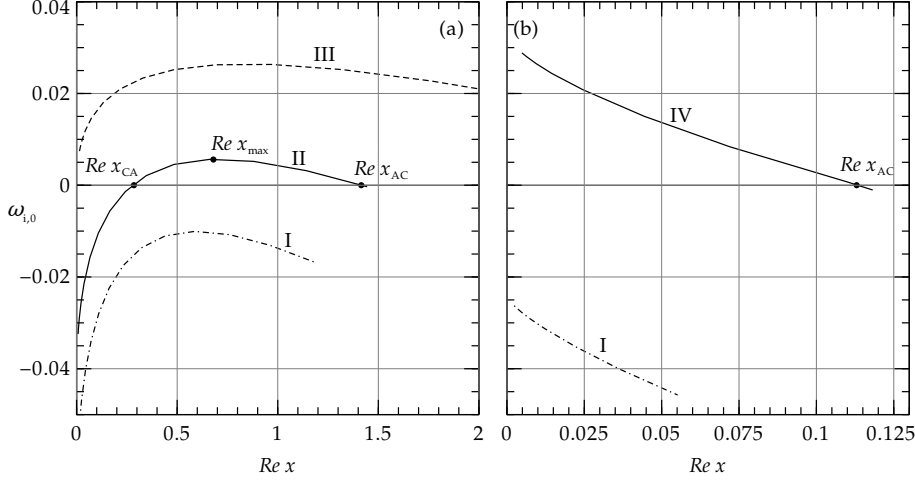


Figure 4.2: Evolution of the absolute growth rate $\omega_{i,0}$ with the axial distance, expressed in units of the injector radius, $Re x$, for a hot jet with $S = 0.6$ and five different combinations of the parameters $(Re, D/\theta_0)$ corresponding to the different regions identified in figure 4.5. In panel (a) $D/\theta \simeq 95.5$ and dash-dotted, solid and dashed lines correspond to $Re = (500, 750, 1500)$, respectively within the regions I, II and III. In panel (b), where $D/\theta \simeq 30.8$, dash-dotted and solid lines correspond to $Re = (250, 500)$, respectively within the regions I and IV.

10^{-3} for a density ratio $S = 0.5$ and an initial momentum thickness $D/\theta_0 = 500$. Also shown is the self-similar mixing layer solution obtained for the hot jet (bold dotted line), showing good agreement with the corresponding boundary layer solution (solid line). Figure 4.1 reveals that, while the velocity profiles are very similar, the density profile of the light jet is much thicker than that of the hot jet, and is also notably displaced towards the outer region due to a much stronger diffusion. The structures of laminar hot and light jets have been thoroughly studied in the works by Sánchez-Sanz *et al.* (2006) and Sánchez-Sanz *et al.* (2010), respectively, to which the reader is referred for a detailed account. The differences between the near-field structures of both kind of jets will be shown below to substantially affect the corresponding spatiotemporal stability properties.

The downstream evolution of the absolute growth rate $\omega_{i,0}(Re x)$ is shown in figure 4.2 for the particular case of a hot jet with $S = 0.6$ [see also figure 4.5 below], and two different values of $D/\theta = (95.5, 30.8)$ in figures 4.2(a) and 4.2(b), respectively. In figure 4.2(a), dash-dotted, solid and dashed lines correspond to values of $Re = (500, 750, 1500)$, while in figure 4.2(b) the dash-dotted and solid lines correspond to $Re = (250, 500)$. Note that the main difference between figures 4.2(a) and 4.2(b) is in the slope at the outlet, which is $d\omega_{i,0}/dx(0) > 0$ in the case of figure 4.2(a), while it is $d\omega_{i,0}/dx(0) < 0$ in figure 4.2(b). The results shown in figure 4.2 illustrate the different

possibilities regarding the absolute or convective nature of the instability in the near field of the hot jet, which divide the $(S, Re, D/\theta_0)$ parameter space into several regions that can be described as follows. Region I is defined by the condition that the local instability is convective everywhere along the jet, $\omega_{i,0}(x) < 0 \forall x$, and is thus expected to lead to globally stable jets in the absence of downstream disturbance feedback. Two examples of hot jets within region I correspond to the dash-dotted lines of figures 4.2(a) and 4.2(b). Jets in region II have a pocket of absolute instability within the jet inside the region $x_{CA} < x < x_{AC}$, bounded by the two critical stations $x_{CA} \simeq 0.285$ and $x_{AC} \simeq 1.415$ where $\omega_{i,0} = 0$, the instability being convective for $x < x_{CA}$ and for $x > x_{AC}$. Note, in particular, that in region II the instability is convective at the outlet, $\omega_{i,0}(0) < 0$. The solid line of figure 4.2(a) shows an example of a jet within region II, where the station with maximum absolute growth rate, $x_{max} \simeq 0.68$, is also defined. The dashed line of figure 4.2(a) corresponds to a jet within region III, defined by the double condition $\omega_{i,0}(0) > 0$ and $x_{max} > 0$ [or $d\omega_{i,0}/dx(0) > 0$], so that the outlet, although absolutely unstable, is not the position of maximum absolute growth rate. Region IV is defined by the double condition $\omega_{i,0}(0) > 0$ and $x_{max} = 0$ [or $d\omega_{i,0}/dx(0) < 0$], so that the maximum absolute growth rate takes place at the jet outlet, and is exemplified by the solid line of figure 4.2(b). Finally, region V is a subregion of region IV, defined by the condition $x_{AC} > l$, i.e. that the extent of the absolutely unstable region is larger than a certain length l . The need to consider region V separately will be discussed in detail below.

Let us begin the study of the $(S, Re, D/\theta_0)$ parameter space by considering the curves $S_c(D/\theta_0; Re)$ which separate, at a fixed value of Re , the region $S > S_c(D/\theta_0; Re)$ where the jet is convectively unstable everywhere, $\omega_{i,0} < 0 \forall x$, from those where a pocket of absolute instability exists in the jet, $S < S_c(D/\theta_0; Re)$. Notice that the condition $S > S_c(D/\theta_0; Re)$ defines a subset of region I, and thus corresponds to globally stable conditions. The marginal curves are displayed in figure 4.3, which shows that there are substantial quantitative differences between the spatiotemporal stability properties of hot and light jets, which are specifically addressed in this work for the first time. The functions $S_c(D/\theta_0; Re)$ shown in figure 4.3 were computed for three different values of the Reynolds number, namely $Re = 100$ (green solid line), $Re = 10^3$ (red solid line) and $Re = 10^4$ (blue solid line), in the cases of a hot jet (a) and of a light jet (b).

The dashed lines shown in figure 4.3 are the critical density ratios based on the outlet base profiles, which are observed to differ from the actual values of S_c in the upper region of the diagram, i.e. for large enough values of D/θ_0 , where $d\omega_{i,0}/dx(0) > 0$ and for which, correspondingly, $x_{max} > 0$. The filled circles indicate the values $(D/\theta_0)^*(Re)$, defined by $d\omega_{i,0}/dx(0) = 0$, which therefore separate the absolutely unstable region III from regions IV and V defined above. For values of $D/\theta > (D/\theta_0)^*(Re)$, for which $x_{max} > 0$, the determination of the marginal curves requires the computation of the

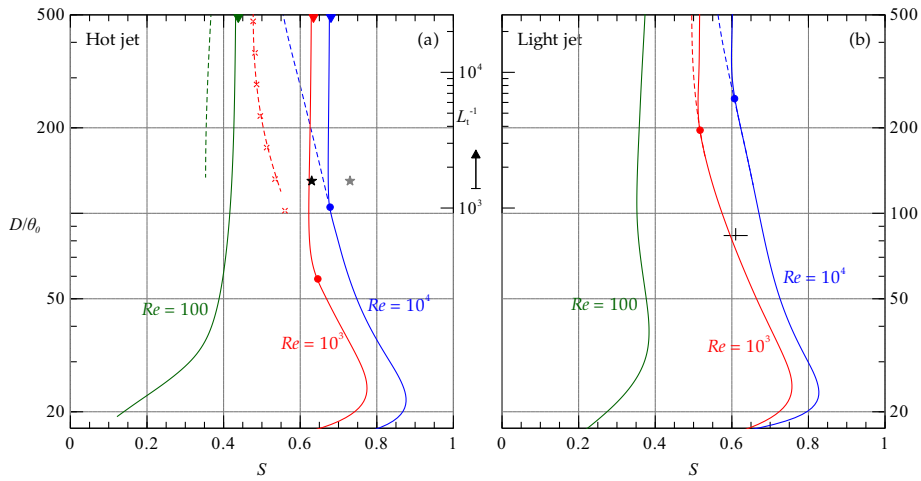


Figure 4.3: The curves $S_c(D/\theta_0)$ for $Re = (100, 10^3, 10^4)$ and (a) hot jets; (b) light jets. Filled circles indicate the values $(D/\theta_0)^*(Re)$ defined in the text. The dashed lines and the red crosses show the critical density ratios computed with outlet base profiles, and with use made of the self-similar mixing-layer solution, respectively. The stars show experimental data for the critical density ratios associated to the two transitions identified as mode I (grey star) and mode II (black star) in the experiments which Monkewitz *et al.* (1990) performed with hot air jets. The cross corresponds to the transition found by Kyle & Sreenivasan (1993) in their experiments with He/air jets.

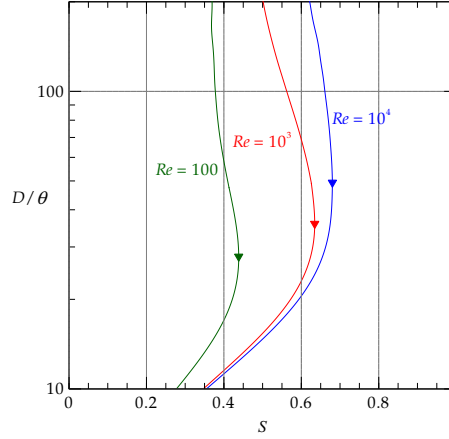


Figure 4.4: Critical density ratio S_c of the self-similar mixing layer solution for hot jets, as a function of the momentum thickness parameter D/θ , for $Re = (100, 10^3, 10^4)$ (green, red and blue solid lines, respectively). The triangles indicate the maximum value of S_c for each value of Re , and are also displayed in the upper part of figure 4.3(a).

jet, while if $D/\theta < (D/\theta_0)^*(Re)$, the marginal curve is determined by the stability properties at the outlet. Note that in the particular case of a light jet at $Re = 100$, $d\omega_{i,0}/dx(0) < 0$ independently of the value of D/θ , and the whole marginal curve is then determined by the base profiles at the exit. The red crosses shown in figure 4.3(a) were computed with use made of the self-similar mixing layer solution for the hot jet, by using the momentum thickness of the *initial profile* as the momentum thickness of the mixing layer, showing good agreement for values of $D/\theta \gtrsim 120$.

In the limit of very thin initial boundary layers, $D/\theta_0 \rightarrow \infty$, all the transition curves shown in figure 4.3 except that of the light jet at $Re = 100$, asymptote to certain critical density ratios which depend only on the Reynolds number. These limits can be explained by the fact that $d\omega_{i,0}/dx(0) > 0$ in these cases, and the value of x_{\max} is such that $(\theta_0/D)^2 \ll x_{\max} \ll 1$. Thus, the velocity and density profiles at the marginally absolutely unstable station can be described, in this case, by means of the self-similar mixing layer solution. This is confirmed by the results shown in figure 4.4, where the critical density ratio S_c associated to the self-similar mixing layer velocity and density profiles is plotted as a function of the momentum thickness for the hot jet case. As can be observed in figure 4.4, the function $S_c(D/\theta)$ has a maximum value, marked with a triangle for the three values of the Reynolds number considered, namely $Re = (100, 10^3, 10^4)$. These maxima are in agreement with the asymptotic values of $S_c(Re)$ obtained for the hot jet, as shown by the positions of the triangles in the upper part of figure 4.3(a). Moreover, although not shown here for conciseness, the values $(D/\theta)_{\max}$ at the maxima of S_c in

figure 4.4 correspond to the value of x_{\max} for each value of Re , according to the fact that $(\theta/D)_{\max} = 0.5f(S)x_{\max}^{1/2}$, where the function $f(S) = \int_{-\infty}^{\infty} F_{\eta}(1 - TF_{\eta})d\eta$ is obtained from the self-similar solution for the mixing layer.

The stars shown in figure 4.3(a) are experimental data for the critical density ratio in hot air jets at $Re \simeq 2650$ obtained by Monkewitz *et al.* (1990). These authors found the existence of two different transitions for decreasing density ratios, leading to instability modes which they called mode I, with $S_c \simeq 0.73$ (grey star), and mode II, at $S_c \simeq 0.63$ (black star). Note that their mode II is located between the red and blue lines, and is thus consistent with our stability results. However, mode I is in clear disagreement, since it is located in region I where no global mode should self-excite due to the fact that the instability is convective throughout the jet. Clearly, more experiments with hot jets are needed to test the predictions of the transition diagram shown in figure 4.3(a). The experimental transition found by Kyle & Sreenivasan (1993) for helium/air mixtures discharging into air at $Re \simeq 4600$ is represented in figure 4.3(b) with a cross which includes the experimental uncertainty. In this case, the experiment is seen to be very close to the transition curve for $Re = 10^3$, and is thus within the absolutely unstable domain corresponding to $Re = 4600$ according to our calculations. However, notice that, in this case, the point falls in region IV defined above, and the jet is thus expected to become globally unstable only when the size of the absolutely unstable domain is large enough, $x_{AC} > l$. According to the numerical simulations performed by Lesshaft *et al.* (2006) with synthetic jets, the value of $l \sim \lambda_0$ where $\lambda_0 = 2\pi/k_{r,0}$ is the wavelength associated to the absolutely unstable mode.

Figure 4.5 shows the different stability regions in the $(D/\theta_0, Re)$ parameter plane for $S = (0.5, 0.6, 0.7)$, computed for hot jets (left column) and light jets (right column). In the particular case of a hot jet with $S = 0.6$, plotted in the middle row-left column of figure 4.5, the full squares indicate the conditions corresponding to the different curves shown in figure 4.2. The globally stable region I prevails for values of $Re < Re_c(D/\theta; S)$, where $Re_c D/\theta$ is represented as a solid line, while for $Re > Re_c(D/\theta; S)$ an absolutely unstable region exists in the jet. Notice that both the value of $Re_c D/\theta$, as well as the structure of the unstable regions II-V, show substantial differences for hot and light jets.

The dashed lines of figure 4.5 are equivalent to the dots in figure 4.3, indicating the condition $d\omega_{i,0}/dx = 0$, which divides the absolutely unstable domain of the $(D/\theta_0, Re)$ -plane into region III, and regions IV and V. Notice that this boundary takes places at higher values of D/θ_0 in the case of light jets, indicating that for typical experimental values of $D/\theta_0 \lesssim 120$ pockets of absolute instability having $x_{CA} > 0$ do not appear within their near field. Furthermore, these pockets are only present within region II, which by definition is always located above the dashed line, and which is separated from region III by the dotted lines. Note that the only difference between region II and III lies

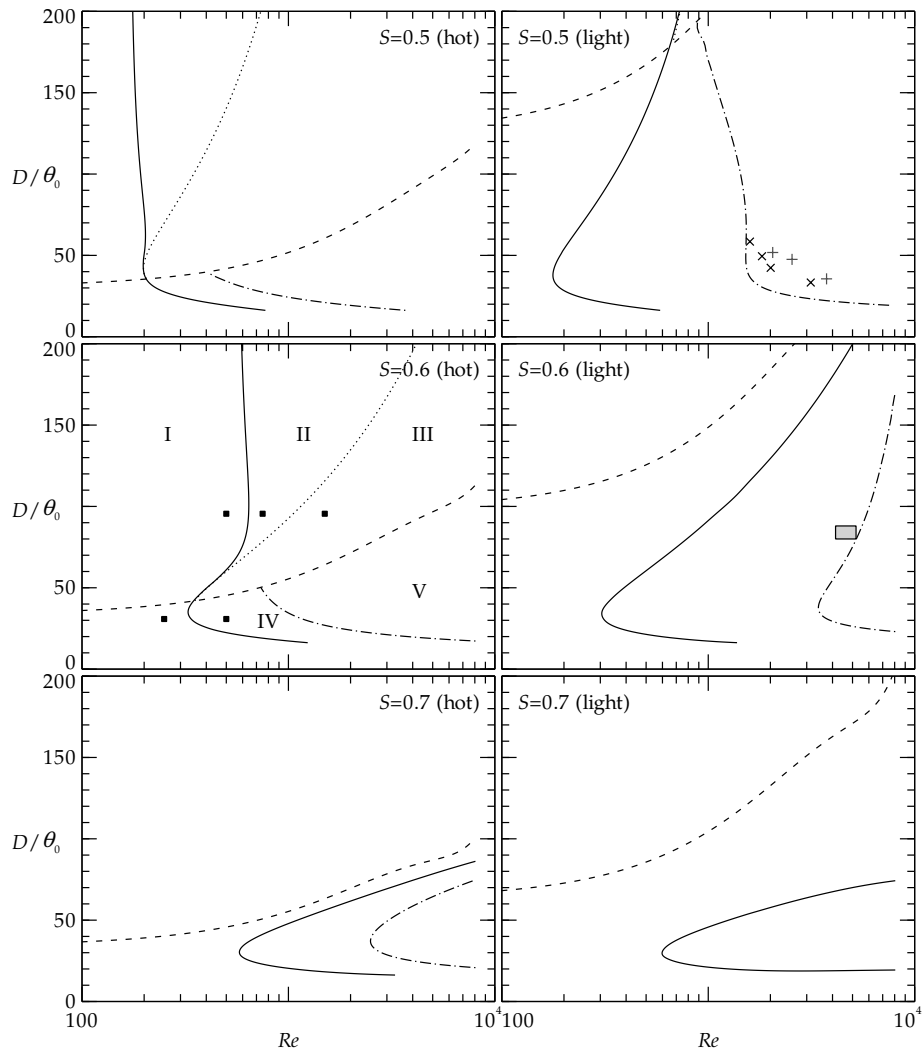


Figure 4.5: The different regions identified in the $(Re, D/\theta_0)$ parameter plane for $S = (0.5, 0.6, 0.7)$, computed for hot jets (left column) and light jets (right column). The different lines separating the regions are explained in the text.

in the positive value of the absolute growth rate at the origin in the latter case, which may have physical significance according to the non-linear global mode theory of Pier *et al.* (1998). Below the dashed lines, the pockets of absolute instability are bounded by the jet outlet, and by the marginal station x_{AC} , corresponding to regions IV and V. The boundary separating these regions is shown as the dashed-dotted lines, which have been plotted according to the above-mentioned criterion $x_{AC} > \lambda_0$, based on the numerical simulations performed by Lesshafft *et al.* (2006).

The experimental results for the transition of helium/air jets obtained by Hallberg & Strykowski (2006) at $S = 0.5$ are shown as black crosses and grey plus signs in the upper right plot of figure 4.5. These authors found that the jet be globally unstable *within* the region bounded by the symbols. Although the first transition, corresponding to the black crosses, is in good agreement with the criterion $x_{AC} = \lambda$, the second transition leading to the re-stabilization of the jet is in strong disagreement with our result, and a different approach is needed to understand this result. In addition, more experiments and/or numerical simulations are needed to have a more complete picture of the global transition in low-density jets. In particular, our stability analysis may well serve as a guide towards that goal.

4.4 Conclusions

We have studied the viscous local, linear, spatiotemporal stability of the near field of incompressible buoyancy-free low-density jets emerging from circular injector tubes of arbitrary length. The cases of a heated jet and a jet with variable molecular weight have been treated separately, showing substantial differences which are addressed for the first time in the present work. Transition diagrams have been computed in selected slices of the $(S, Re, D/\theta_0)$ parameter space governing the stability of the jet. The detailed consideration of the downstream evolution of the local stability properties allowed us to identify five different regions, and to compute their corresponding boundaries in several representative cases.

Our results highlight the importance of the individual roles played by the Reynolds number and the initial boundary layer momentum thickness, which must be treated separately in order to properly describe the instability of the jet. A few comparisons with experiments show partial agreement, and indicate that future work is needed from both the experimental and stability sides to achieve a better understanding of the appearance of global modes in low-density jets.

References

- CHOMAZ, J. M. 2005 Global instabilities in spatially developing flows: Non-normality and nonlinearity. *Ann. Rev. Fluid Mech.* **37**, 357–392.
- COENEN, W., SEVILLA, A. & SÁNCHEZ, A. 2008 Absolute instability of light jets emerging from circular injector tubes. *Phys. Fluids* **20**, 074104.
- COHEN, J. & WYGNANSKI, I. 1987 The evolution of instabilities in the axisymmetrical jet. Part 1. The linear growth of disturbances near the nozzle. *J. Fluid Mech.* **176**, 191–219.
- HALLBERG, M. P., SRINIVASAN, V., GORSE, P. & STRYKOWSKI, P. J. 2007 Suppression of global modes in low-density axisymmetric jets using coflow. *Phys. Fluids* **19** (1), 014102.
- HALLBERG, M. P. & STRYKOWSKI, P. J. 2006 On the universality of global modes in low-density axisymmetric jets. *J. Fluid Mech.* **569**, 493–507.
- HO, C.-M. & HUERRE, P. 1985 Perturbed free shear layers. *Annu. Rev. Fluid Mech.* **16**, 365–424.
- HUERRE, P. & MONKEWITZ, P. A. 1985 Absolute and convective instabilities in free shear layers. *J. Fluid Mech.* **159**, 151–168.
- HUERRE, P. & MONKEWITZ, P. A. 1990 Local and global instabilities in spatially developing flows. *Annu. Rev. Fluid Mech.* **22**, 473–537.
- JENDOUBI, S. & STRYKOWSKI, P. J. 1994 Absolute and convective instability of axisymmetric jets with external flow. *Phys. Fluids* **6**, 3000–3009.
- KYLE, D. M. & SREENIVASAN, K. R. 1993 The instability and breakdown of a round variable-density jet. *J. Fluid Mech.* **249**, 619–664.
- LESSHAFFT, L. & HUERRE, P. 2007 Linear impulse response in hot round jets. *Phys. Fluids* **19** (2), 024102.
- LESSHAFFT, L., HUERRE, P. & SAGAUT, P. 2007 Frequency selection in globally unstable round jets. *Phys. Fluids* **19** (5), 054108.
- LESSHAFFT, L., HUERRE, P., SAGAUT, P. & TERRACOL, M. 2006 Nonlinear global modes in hot jets. *J. Fluid Mech.* **554**, 393–409.
- MATTINGLY, G. E. & CHANG, C. C. 1974 Unstable waves on an axisymmetric jet column. *J. Fluid Mech.* **65** (3), 541–560.

- MICHALKE, A. 1965 On spatially growing disturbances in an inviscid shear layer. *J. Fluid Mech.* **23**, 521–544.
- MICHALKE, A. 1970 A note on the spatial jet-instability of the compressible cylindrical vortex sheet. *DLR research rep.* pp. FB–70–51.
- MONKEWITZ, P. A., BECHERT, D. W., BARSIKOW, B. & LEHMANN, B. 1990 Self-excited oscillations and mixing in a heated round jet. *J. Fluid Mech.* **213**, 611–639.
- MONKEWITZ, P. A. & SOHN, K. D. 1988 Absolute instability in hot jets. *AIAA J.* **28**, 911–916.
- NICHOLS, J. W., SCHMID, P. J. & RILEY, J. J. 2007 Self-sustained oscillations in variable-density round jets. *J. Fluid Mech.* **582**, 341–376.
- PIER, B., HUERRE, P., CHOMAZ, J.-M. & COUAIRO, A. 1998 Steep nonlinear global modes in spatially developing media. *Phys. Fluids* **10** (10), 2433–2435.
- RAGHU, S. & MONKEWITZ, P. A. 1991 The bifurcation of a hot round jet to limit-cycle oscillations. *Phys. Fluids* **3** (4), 501–503.
- SÁNCHEZ-SAN, M., ROSALES, M. & SÁNCHEZ, A.L. 2010 The hydrogen laminar jet. *Int. J. Hydrogen Energy* **35**, 3919–3927.
- SÁNCHEZ-SANZ, M., SÁNCHEZ, A.L. & LIÑÁN, A. 2006 Fronts in high-temperature laminar gas jets. *J. Fluid Mech.* **547**, 257–266.
- SEVILLA, A., GORDILLO, J. M. & MARTÍNEZ-BAZÁN, C. 2002 The effect of the diameter ratio on the absolute and convective instability of free coflowing jets. *Phys. Fluids* **14**, 3028–3038.
- SREENIVASAN, K. R., RAGHU, S. & KYLE, D. 1989 Absolute instability in variable density round jets. *Exps. Fluids* **7**, 309–317.
- SRINIVASAN, K., HALLBERG, M. P. & STRYKOWSKI, P. J. 2010 Viscous linear stability of axisymmetric low-density jets: Parameters influencing absolute instability. *Phys. Fluids* **22**, 024103.

General conclusions and future prospects

In this dissertation we have performed a detailed study of the local, linear, spatiotemporal stability of the near field of incompressible, buoyancy-free low-density jets emerging from circular injector tubes of arbitrary length, for large values of the Reynolds number. Transition diagrams for convective to absolute instability have been obtained in the parameter space spanned by the jet-to-ambient density ratio S , the Reynolds number Re and the nondimensional injector tube length L_t , directly related to the initial momentum thickness of the jet shear layer. In the development, we have taken into account the downstream evolution of the local stability characteristics in the near field of the jet. To that end, for each combination of the three parameters, the basic jet flow has been calculated using the boundary layer equations, and the most unstable normal mode with zero group velocity has been determined as a function of the downstream distance. This procedure allowed us to establish the local convective or absolute character of the instability along the near field of the jet. The use of the boundary layer equations enabled us to separate the effect of the injector tube length from that of the Reynolds number. We have to emphasize that for short injector tubes, our results encompass those for jets emerging from nozzles since in both cases the boundary layer that appears in the jet exit profile is of the Blasius type.

It has been shown that the injector tube has an important effect on the stability properties of the jet through the shape of the velocity profiles at the outlet, where the density profile has a top-hat shape. This strong dependence of the spatiotemporal instability of the jet on the exact shape of the base flow profiles is in agreement with recent results by Lesshafft (personal communication). We have found that for high Reynolds numbers, the jet-to-ambient density ratio reaches a maximum value for intermediate tube lengths $L_t \simeq 0.04$, corresponding to a momentum thickness $D/\theta_0 = 25$. Moreover, for long enough injector tubes and small values of the density ratio the helical instability mode may prevail in the dynamics of the jet. A detailed analysis of the separate effects of the Reynolds number and the boundary layer thickness at the outlet has also been performed, allowing us to identify regions in parameter space which may be relevant in understanding the nonlinear behavior of low-density jets.

For base flow profiles with vanishingly thin shear layers, the viscous stability has been analyzed through the use of discontinuous profiles. For this aim, we have extended the formalism originally developed by Drazin (1961) to account for variations in the density and transport properties. This discontinuous representation of the base flow, in which the thin shear layers are substituted by vortex sheets is useful to study modal solutions with wavelengths much larger than the characteristic shear-layer thickness. By successive integrations of the stability equations across the discontinuity in the base profiles, a set of general jump conditions has been deduced, which has then been employed in the study of discontinuous jets and wakes to match the exact solutions of the stability equations in the regions of uniform velocity and density on either side of the vortex sheet. The algebraic dispersion relation that is obtained in this manner has been validated by comparing its solutions with stability calculations for continuous parametric profiles with vanishingly thin shear layers.

We want to emphasize the generality of the discontinuous formalism described hereabove. The application of the derived jump conditions is not restricted to piecewise constant profiles, but can also cope with discontinuities in the derivatives of the base profiles, or a combination of both. For example, they could be used to obtain a viscous dispersion relation valid for planar mixing layers, which appear frequently in applications. Furthermore, the formalism could be readily extended to account for molecular weight variations instead of temperature variations to study, for example, the viscous stability characteristics of Helium jets discharging into air.

The specific shape of the base flow profiles has been shown to matter even in the limit of vanishingly thin shear layers through two types of integrals that appear in the jump conditions. Consequently, to obtain accurate results in the stability analysis of hot gas jets emerging from very short injectors, the Blasius velocity profile found near the wall should be used when evaluating these integrals. This should certainly be addressed in future research, together with the extension to flows with variable molecular weight mentioned hereabove.

In the near field of the jet, the effect of the density profile and its combined downstream evolution with the velocity profile is seen to have an important effect on the local stability properties. With this in mind, and since the downstream mixing of low-density jets with molecular weight variations is significantly different from that of hot jets, it can be anticipated that the evolution of their local stability characteristics will also be different. This has indeed been found in chapter 4, where we treated these two particular cases separately, comparing also the stability calculations with several experimental results available in the literature. At this point, it became clear that more experimental data is needed to have a reasonably complete pictures of the transition conditions need for self-excited behavior in low-density jets. The transition diagrams obtained in this study could thereby prove very helpful in guiding future work aiming at this goal, in-

cluding both experiments and direct numerical simulations of the jet.

Although we have taken the strict application of local stability theory to its limit, a few improvements could be implemented, for instance non-parallel corrections taking into account the slenderness of the jet. To that end, use could be made of the parabolized stability equations.

References

- DRAZIN, P. G. 1961 Discontinuous velocity profiles for the Orr-Sommerfeld equation. *J. Fluid Mech.* **10**, 571–583.

Numerical methods

A.1 Numerical integration of the jet flow

To find a numerical solution of the parabolic boundary-layer equations (1.2)–(1.4), (1.10) that describe the jet flow field, we have used a fully implicit marching procedure in the streamwise x -direction, applying second-order accurate finite difference schemes. The equations are discretized on the points of a non-uniform grid, carefully designed to cluster grid point axially near the entrance of the jet at $x = 0$ and radially around the jet shear layer at $r = 1$. For this purpose, we use grid transformations proposed by Roberts (1971) that map the uniformly distributed computational domains $\xi \in [0, 1]$, $\eta \in [0, 1]$ on the non-uniform physical domains $x \in [0, x_{\max}]$, $r \in [0, r_{\max}]$:

$$\begin{cases} x = 1 + (x_{\max} - 1) \frac{(\tau_x + 1) - (\tau_x - 1) \frac{\tau_x + 1}{\tau_x - 1}^{1-\eta}}{1 + \frac{\tau_x + 1}{\tau_x - 1}^{1-\eta}}, \\ \xi = 1 - \frac{\ln \frac{\tau_x + 1 - x/x_{\max}}{\tau_x - 1 + x/x_{\max}}}{\ln \frac{\tau_x + 1}{\tau_x - 1}}, \end{cases} \quad (\text{A.1a})$$

and

$$\begin{cases} r = \frac{(\beta + 2\alpha) \left(\frac{\beta + 1}{\beta - 1} \right)^{\frac{r_{\max} \eta / Q - \alpha}{1 - \alpha}} - \beta + 2\alpha}{(2\alpha + 1) \left[1 + \left(\frac{\beta + 1}{\beta - 1} \right)^{\frac{r_{\max} \eta / Q - \alpha}{1 - \alpha}} \right]} & \left(0 \leq \eta \leq \frac{Q}{r_{\max}}, 0 \leq r \leq 1 \right), \\ \eta = \frac{Q}{r_{\max}} \left[\alpha + (1 + \alpha) \frac{\ln \frac{\beta + r(2\alpha + 1) - 2\alpha}{\beta - r(2\alpha + 1) + 2\alpha}}{\ln \frac{\beta + 1}{\beta - 1}} \right] \end{cases} \quad (\text{A.1b})$$

$$\begin{cases} r = 1 + (r_{\max} - 1) \frac{(\tau + 1) - (\tau - 1) \left(\frac{\tau + 1}{\tau - 1} \right)^{1 - \frac{\eta - Q/r_{\max}}{1 - Q/r_{\max}}}}{1 + \left(\frac{\tau + 1}{\tau - 1} \right)^{1 - \frac{\eta - Q/r_{\max}}{1 - Q/r_{\max}}}} & \left(\frac{Q}{r_{\max}} \leq \eta \leq 1, 1 \leq r \leq r_{\max} \right), \\ \eta = \frac{Q}{r_{\max}} + \left(1 + \frac{Q}{r_{\max}} \right) \left[1 - \frac{\ln \frac{\tau + 1 - (r - 1)/(r_{\max} - 1)}{\tau - 1 + (r - 1)/(r_{\max} - 1)}}{\ln \frac{\tau + 1}{\tau - 1}} \right] \end{cases} \quad (\text{A.1c})$$

In the calculations we have used $N_x = 400$ grid points in the axial direction, with $x_{\max} = 0.0025$ and $\tau_x - 1 = 0.02$, and $N_r = 5000$ grid points in the radial direction, with $r_{\max} = 1000$, $Q = 100$, $\tau - 1 = 5.32 \times 10^{-6}$ and $\beta - 1 = 0.001$.

In the computational domain, we apply a second-order accurate backward finite-difference formula

$$\left. \frac{\partial \phi}{\partial \xi} \right|_j^{i+1} \simeq \frac{3\phi_j^{i+1} - 4\phi_j^i + \phi_j^{i-1}}{2\Delta\xi} \quad (\text{A.2})$$

in the axial ξ -direction and second-order accurate central-difference schemes

$$\left. \frac{\partial \phi}{\partial \eta} \right|_j^{i+1} \simeq \frac{\phi_{j+1}^{i+1} - \phi_{j-1}^{i+1}}{2\Delta\eta} \quad \text{and} \quad \left. \frac{\partial \phi}{\partial \eta} \right|_j^{i+1} \simeq \frac{\phi_{j+1}^{i+1} + 2\phi_j^{i+1} - \phi_{j-1}^{i+1}}{(\Delta\eta)^2} \quad (\text{A.3})$$

in the radial η direction.

At each step in the marching procedure, an iterative process is carried out, in which we subsequently solve a linearized form of the momentum and energy/species equations for u and T or Y , followed by the solution of the continuity equation to obtain v , using the newly calculated values of u and T or Y . At each iteration step, the flow variables that are used in the linearization are updated with the solution that was found in the last completed step. This process is continued until convergence is achieved, here defined to be when $\{\sum_{j=1}^{N_r} (\phi - \tilde{\phi})_{i,j}^2 / \sum_{j=1}^{N_r} \tilde{\phi}_{i,j}^2\}^{1/2}$ falls below a prescribed tolerance of 10^{-6} for all flow variables ϕ .

A.2 Chebyshev spectral collocation method

The generalized eigenvalue problem set up by the system of ordinary differential equations (1.17a)–(1.17f) with boundary conditions (1.20)–(1.21) can be solved with a Chebyshev spectral collocation method.

When a complex frequency ω needs to be computed for a given complex wavenumber k , the eigenvalue problem is written as

$$\mathbf{A}\mathbf{x} = \omega\mathbf{B}\mathbf{x}, \quad (\text{A.4})$$

where $\mathbf{x} = (\hat{\rho}, \hat{u}, \hat{v}, \hat{w}, \hat{p})$, and \mathbf{A} and \mathbf{B} are two linear operators.

Following Khorrami *et al.* (1989), the eigenfunctions $(\hat{\rho}, \hat{u}, \hat{v}, \hat{w}, \hat{p})$ are mapped from the physical domain $0 \leq r \leq r_{\max}$ onto the Chebyshev interval $-1 \leq \xi \leq 1$, where they are discretized in N collocation points,

$$\xi_j = \cos\left(\frac{j\pi}{N-1}\right), \quad j = 0, \dots, N-1. \quad (\text{A.5})$$

For this purpose, we use the transformation proposed by Lesshafft & Huerre (2007)

$$\xi(r) = \frac{r_c}{2r} - \left(1 + \frac{r_c^2}{4r^2} + \frac{2r_c}{r_{\max}} - \frac{r_c}{r}\right)^{1/2}, \quad (\text{A.6a})$$

$$r(\xi) = r_c \frac{1 - \xi}{1 - \xi^2 + 2r_c/r_{\max}}. \quad (\text{A.6b})$$

In this way, approximately half of the points $r_j = r(\xi_j)$ are placed in the interval $0 \leq r \leq r_c$, concentrated around $r = r_c/2$. For the jet profiles considered in this dissertation, values $r_c = 2$ and $r_{\max} = 1000$ were found satisfying. A minimum number of $N = 128$ collocation points was used, increasing this number for profiles with thin shear layers so that a minimum of 10 collocation points are placed within the high-gradient regions of the velocity and density profiles.

The linear operators \mathbf{A} and \mathbf{B} of the eigenvalue problem (A.4) are $5N \times 5N$ -matrices containing $5(N - 1)$ lines with the five stability equations discretized in the $N - 1$ interior nodes, and $10N$ lines representing the boundary conditions at the extremes of the Chebyshev domain. To compute ω in the generalized eigenvalue problem (A.4), we use the ZGGEV routine from the LAPACK linear algebra library.

If a complex wavenumber k needs to be computed for a given complex frequency ω , we can write the eigenvalue problem as

$$[\mathbf{A} - k\mathbf{B}_1 - k^2\mathbf{B}_2]\mathbf{x} = 0, \quad (\text{A.7})$$

which can be converted into the linear eigenvalue problem

$$\mathbf{M}_A \mathbf{z} = k \mathbf{M}_B \mathbf{z}, \quad (\text{A.8})$$

where $\mathbf{z} = (\mathbf{x}, k\mathbf{x}) = (\hat{\rho}, \hat{u}, \hat{v}, \hat{w}, \hat{p}, k\hat{\rho}, k\hat{u}, k\hat{v}, k\hat{w}, k\hat{p})$,

$$\mathbf{M}_A = \begin{bmatrix} \mathbf{0} & \mathbf{I} \\ \mathbf{A} & -\mathbf{B}_1 \end{bmatrix} \quad \text{and} \quad \mathbf{M}_B = \begin{bmatrix} \mathbf{I} & \mathbf{0} \\ \mathbf{0} & \mathbf{B}_2 \end{bmatrix}. \quad (\text{A.9})$$

This system can be solved as described above. Note that now the matrices \mathbf{M}_A and \mathbf{M}_B are significantly larger, counting $10N \times 10N$ elements, and consequently the computational cost significantly higher.

A.3 Saddle point determination

In the surroundings of the saddle point (ω_0, k_0) , the frequency $\omega(k)$ as a function of the wavenumber k admits a quadratic Taylor expansion around k_0 ,

$$\omega(k) = \omega_0 + l(k - k_0)^2. \quad (\text{A.10})$$

This can be exploited in an iterative procedure to find the location of (ω_0, k_0) as follows. We choose three wavenumbers k_1, k_2, k_3 around an initial guess k_0^* with

$$k_n = k_0^* (1 + \varepsilon e^{i2\pi(n-1)/3}) \quad (n = 1, 2, 3), \quad (\text{A.11})$$

where ε is a distance small enough for k_n to fall in the region where the quadratic approximation of $\omega(k)$ is valid. We then solve the eigenvalue problem for each of the k_n using the spectral collocation method described in the previous section, yielding three frequencies ω_1, ω_2 and ω_3 . Now the three pairs (ω_n, k_n) can be used in a Newton-Raphson method to find (ω_0, k_0) and l that make the quadratic approximation (A.10) fit or, in other words, to find the saddle point. That is, we search the zero $\mathbf{x} = [\omega_0, k_0, l]$ of the function

$$\mathbf{F}(\mathbf{x}) = \begin{bmatrix} \omega_1 - \omega_0 - l(k_1 - k_0)^2 \\ \omega_2 - \omega_0 - l(k_2 - k_0)^2 \\ \omega_3 - \omega_0 - l(k_3 - k_0)^2 \end{bmatrix}. \quad (\text{A.12})$$

With the newly obtained value of k_0 , three new values of k_1, k_2 and k_3 are calculated using (A.11), and the quadratic fitting is repeated. This iterative procedure is repeated until relative differences in (ω_0, k_0) between subsequent iteration steps fall below 10^{-5} . At each step ε is slightly decreased to enhance the accuracy of the procedure.

Note that this method takes advantage of the linearity of the eigenvalue problem in ω . A similar method was formulated by Monkewitz & Sohn (1988), but they proposed an expansion of $k(\omega)$, in this way necessitating the solution of the quadratic eigenvalue problem in k . In the previous section we saw that this implies a higher computational cost.

References

- KHORRAMI, M. R., MALIK, M. R. & ASH, R. L. 1989 Applications of spectral collocation techniques to the stability of swirling flows. *J. Comput. Phys.* **81**, 206.
- LESSHAFFT, L. & HUERRE, P. 2007 Linear impulse response in hot round jets. *Phys. Fluids* **19** (2), 024102.

- MONKEWITZ, P. A. & SOHN, K. D. 1988 Absolute instability in hot jets. *AIAA J.* **28**, 911–916.
- ROBERTS, G. O. 1971 Computational meshes for boundary layer problems. In *Lecture Notes in Physics* **8**, , vol. 61, pp. 171–177. Proc. Second Int. Conf. Num. Methods Fluid Dyn., Springer, Berlin.

Alphabetical list of references

- ABRAMOWITZ, M. & STEGUN, I. A. 1970 *Handbook of Mathematical Functions*. Dover Publications Inc., New York.
- ANDERSON, D. A., TANNEHILL, J. C. & PLETCHER, R. H. 1984 *Computational Fluid Mechanics and Heat Transfer*. Hemisphere, New York.
- BATCHELOR, G. K. & GILL, A. E. 1962 Analysis of the stability of axisymmetric jets. *J. Fluid Mech.* **14**, 529–551.
- BERS, A. 1975 Linear waves and instabilities. In *Physique des plasmas* (ed. C. Dewitt & J. Peyraud), pp. 117–123. Gordon & Breach.
- BERS, A. 1983 Space-time evolution of plasma instabilities – absolute and convective. In *Handbook of Plasma Physics* (ed. M. N. Rosenbluth & R. Z. Sagdeev), , vol. 1, pp. 451–517. North-Holland.
- BRIGGS, R. J. 1964 *Electron-stream interaction with plasmas (Research monograph no. 29)*. MIT Press.
- BROWN, G. L. & ROSHKO, A. 1974 On density effects and large structure in turbulent mixing layers. *J. Fluid Mech.* **64**, 775–816.
- CHAPMAN, D. R. 1949 Laminar mixing of a compressible fluid. *Tech. Rep.* NACA-TN-1800. NASA Ames Research Center.
- CHOMAZ, J. M. 2005 Global instabilities in spatially developing flows: Non-normality and nonlinearity. *Ann. Rev. Fluid Mech.* **37**, 357–392.
- CHOMAZ, J. M., HUERRE, P. & REDEKOPP, L. G. 1988 Bifurcation to local and global modes in spatially developing flows. *Phys. Rev. Lett.* **60**, 25–.
- COENEN, W., SEVILLA, A. & SÁNCHEZ, A. 2008 Absolute instability of light jets emerging from circular injector tubes. *Phys. Fluids* **20**, 074104.
- COHEN, J. & WYGNANSKI, I. 1987 The evolution of instabilities in the axisymmetrical jet. Part 1. The linear growth of disturbances near the nozzle. *J. Fluid Mech.* **176**, 191–219.

- CRIGHTON, D. G. & GASTER, M. 1976 Stability of slowly divergent jet flow. *J. Fluid Mech.* **77**, 397–413.
- CROW, S. C. & CHAMPAGNE, F. H. 1971 Orderly structure in jet turbulence. *J. Fluid Mech.* **48**, 547–591.
- DEISSLER, R. J. 1987 The convective nature of instability in plane Poiseuille flow. *Phys. Fluids* **30** (8), 2303–2305.
- DRAZIN, P. G. 1961 Discontinuous velocity profiles for the Orr-Sommerfeld equation. *J. Fluid Mech.* **10**, 571–583.
- DRAZIN, P. G. 1962 On stability of parallel flow of an incompressible fluid of variable density and viscosity. *Proc. Cambridge Philos. Soc.* **58**, 646–661.
- ESCH, R. E. 1957 The instability of a shear layer between two parallel streams. *J. Fluid Mech.* **3**, 289–303.
- GASTER, M. 1962 A note on the relation between temporally increasing and spatially increasing disturbances in hydrodynamic stability. *J. Fluid Mech.* **14**, 222–224.
- GASTER, M. 1968 Growth of disturbances in both space and time. *Phys. Fluids* **11**, 723–727.
- HALLBERG, M. P., SRINIVASAN, V., GORSE, P. & STRYKOWSKI, P. J. 2007 Suppression of global modes in low-density axisymmetric jets using coflow. *Phys. Fluids* **19** (1), 014102.
- HALLBERG, M. P. & STRYKOWSKI, P. J. 2006 On the universality of global modes in low-density axisymmetric jets. *J. Fluid Mech.* **569**, 493–507.
- HELMHOLTZ, H. VON 1868 Über discontinuirliche Flüssigkeitsbewegungen. *Monats. Königl. Preuss. Akad. Wiss. Berlin* **23**, 215–228.
- HIRSCHFELDER, J. O., CURTISS, C. F. & BIRD, R. B. 1954 *Molecular theory of gases and liquids*. J. Wiley, New York.
- HO, C.-M. & HUERRE, P. 1985 Perturbed free shear layers. *Annu. Rev. Fluid Mech.* **16**, 365–424.
- HOLMES, M. H. 2007 *Introduction to Numerical Methods in Differential Equations*. Springer, New York.
- HUERRE, P. 1987 Spatio-temporal instabilities in closed and open flows. In *Instabilities and Nonequilibrium structures* (ed. E. Tirapegui & D. Villaroel), pp. 141–177. D. Reidel Publishing Company.

- HUERRE, P. 2000 Open shear flow instabilities. In *Perspectives in fluid dynamics* (ed. G. Batchelor, K. Moffatt & G. Worster), pp. 159–229. Cambridge.
- HUERRE, P. & MONKEWITZ, P. A. 1985 Absolute and convective instabilities in free shear layers. *J. Fluid Mech.* **159**, 151–168.
- HUERRE, P. & MONKEWITZ, P. A. 1990 Local and global instabilities in spatially developing flows. *Annu. Rev. Fluid Mech.* **22**, 473–537.
- HUERRE, P. & ROSSI, M. 1998 Hydrodynamic instabilities in open flows. In *Hydrodynamics and nonlinear instabilities* (ed. C. Godrèche & P. Manneville), pp. 81–294. Cambridge.
- ITO, R. & SENO, T. 1979 Effect of exit geometry on jet behavior. *J. Chem. Eng. Jpn.* **12** (6), 430–435.
- JENDOUBI, S. & STRYKOWSKI, P. J. 1994 Absolute and convective instability of axisymmetric jets with external flow. *Phys. Fluids* **6**, 3000–3009.
- JUNIPER, M. P. 2007 The full impulse response of two-dimensional jet/wake flows and implications for confinement. *J. Fluid Mech.* **590**, 163–185.
- JUNIPER, M. P. 2008 The effect of confinement on the stability of non-swirling round jet/wake flows. *J. Fluid Mech.* **605**, 227–252.
- KAMBE, T. 1969 The stability of an axisymmetric jet with parabolic profile. *J. Phys. Soc. Jpn.* **26** (2), 566–575.
- KELVIN, LORD 1871 Hydrokinetic solutions and observations. *Phil Mag.* (4) **42**, 362–377.
- KHORRAMI, M. R., MALIK, M. R. & ASH, R. L. 1989 Applications of spectral collocation techniques to the stability of swirling flows. *J. Comput. Phys.* **81**, 206.
- KOCH, W. 1985 Local instability characteristics and frequency determination of self-excited shear flows. *J. Sound Vibr.* **99**, 53–83.
- KUCHEMAN, D., CRABTREE, L. F. & SOWERBY, L. 1963 Three-dimensional boundary layers. In *Laminar Boundary Layers* (ed. L. Rosenhead), pp. 439–446. Oxford University Press.
- KUPFER, K., BERS, A. & RAM, A. K. 1987 The cusp map in the complex frequency plane for absolute instabilities. *Phys. Fluids* **30**, 3075–3082.
- KYLE, D. M. & SREENIVASAN, K. R. 1993 The instability and breakdown of a round variable-density jet. *J. Fluid Mech.* **249**, 619–664.

- LANDAU, L. & LIFSCHITZ, E. M. 1954 *Mechanics of Continuous Media*. Moscow: Fizmatgiz (In Russian).
- LANDAU, L. & LIFSCHITZ, E. M. 1959 *Fluid Mechanics*. London: Pergamon.
- LECONTE, J. 1858 On the influence of musical sounds on the flame of a jet of coal-gas. *Phil. Mag.* **15**, 235–239.
- LESSEN, M. 1950 On stability of free laminar boundary layer between parallel streams. *Nat. Adv. Comm. Aero.* **979**.
- LESSEN, M. & SINGH, P. J. 1973 The stability of axisymmetric free shear layers. *J. Fluid Mech.* **60** (3), 433–457.
- LESSHAFFT, L. & HUERRE, P. 2007 Linear impulse response in hot round jets. *Phys. Fluids* **19** (2), 024102.
- LESSHAFFT, L., HUERRE, P. & SAGAUT, P. 2007 Frequency selection in globally unstable round jets. *Phys. Fluids* **19** (5), 054108.
- LESSHAFFT, L., HUERRE, P., SAGAUT, P. & TERRACOL, M. 2006 Nonlinear global modes in hot jets. *J. Fluid Mech.* **554**, 393–409.
- MATTINGLY, G. E. & CHANG, C. C. 1974 Unstable waves on an axisymmetric jet column. *J. Fluid Mech.* **65** (3), 541–560.
- MELIGA, P., SIPP, D. & CHOMAZ, J.-M. 2008 Absolute instability in axisymmetric wakes: compressible and density variation effects. *J. Fluid Mech.* **600**, 373–401.
- MICHALKE, A. 1964 On the inviscid instability of the hyperbolic-tangent velocity profile. *J. Fluid Mech.* **19**, 543–556.
- MICHALKE, A. 1965 On spatially growing disturbances in an inviscid shear layer. *J. Fluid Mech.* **23**, 521–544.
- MICHALKE, A. 1970 A note on the spatial jet-instability of the compressible cylindrical vortex sheet. *DLR research rep.* pp. FB–70–51.
- MICHALKE, A. & HERMANN, G. 1982 On the inviscid instability of a circular jet with external flow. *J. Fluid Mech.* **114**, 343–359.
- MOLLENDORF, J. C. & GEBHART, B. 1973 An experimental and numerical study of the viscous stability of a round laminar vertical jet with and without thermal buoyancy for symmetric and asymmetric disturbances. *J. Fluid Mech.* **61** (2), 367–399.

- MONKEWITZ, P. A. 1988 The absolute and convective nature of instability in two-dimensional wakes at low reynolds numbers. *Phys. Fluids* **31**, 999–1006.
- MONKEWITZ, P. A., BECHERT, D. W., BARSIKOW, B. & LEHMANN, B. 1990 Self-excited oscillations and mixing in a heated round jet. *J. Fluid Mech.* **213**, 611–639.
- MONKEWITZ, P. A. & HUERRE, P. 1982 Influence of the velocity ratio on the spatial instability of mixing layer. *Phys. Fluids* **25**, 1137–1143.
- MONKEWITZ, P. A. & SOHN, K. D. 1988 Absolute instability in hot jets. *AIAA J.* **28**, 911–916.
- MORRIS, P. J. 1976 The spatial viscous instability of axisymmetric jets. *J. Fluid Mech.* **77** (3), 511–529.
- NICHOLS, J. W., SCHMID, P. J. & RILEY, J. J. 2007 Self-sustained oscillations in variable-density round jets. *J. Fluid Mech.* **582**, 341–376.
- PAVITHRAN, S. & REDEKOPP, L. G. 1989 The absolute-convective transition in subsonic mixing layers. *Phys. Fluids A* **1** (10), 1736–1739.
- PIER, B. & HUERRE, P. 2001 Nonlinear self-sustained structures and fronts in spatially developing wake flows. *J. Fluid Mech.* **145**, 145–174.
- PIER, B., HUERRE, P., CHOMAZ, J.-M. & COUAIRO, A. 1998 Steep nonlinear global modes in spatially developing media. *Phys. Fluids* **10** (10), 2433–2435.
- RAGHU, S. & MONKEWITZ, P. A. 1991 The bifurcation of a hot round jet to limit-cycle oscillations. *Phys. Fluids* **3** (4), 501–503.
- RAVIER, S., ABID, M., AMIELH, M. & ANSELMET, F. 2006 Direct numerical simulation of variable-density plane jets. *J. Fluid Mech.* **546**, 153–191.
- RAYLEIGH, LORD 1879 On the stability of jets. *Proc. London Math. Soc.* **10**, 4–13.
- RAYLEIGH, LORD 1880 On the stability, or instability, of certain fluid motions. *Proc. London Math. Soc.* **11**, 57–70.
- RAYNAL, L., J.-L., HARION, FAVRE-MARINET, M. & BINDER, G. 1996 The oscillatory instability of plane variable-density jets. *Phys. Fluids* **8**, 993–1006.
- REYNOLDS, A. J. 1962 Observations of a liquid-into-liquid jet. *J. Fluid Mech.* **14**, 552–556.
- ROBERTS, G. O. 1971 Computational meshes for boundary layer problems. In *Lecture Notes in Physics* **8**, , vol. 61, pp. 171–177. Proc. Second Int. Conf. Num. Methods Fluid Dyn., Springer, Berlin.

- SÁNCHEZ-SAN, M., ROSALES, M. & SÁNCHEZ, A.L. 2010 The hydrogen laminar jet. *Int. J. Hydrogen Energy* **35**, 3919–3927.
- SÁNCHEZ-SANZ, M., SÁNCHEZ, A.L. & LIÑÁN, A. 2006 Fronts in high-temperature laminar gas jets. *J. Fluid Mech.* **547**, 257–266.
- SEVILLA, A., GORDILLO, J. M. & MARTÍNEZ-BAZÁN, C. 2002 The effect of the diameter ratio on the absolute and convective instability of free coflowing jets. *Phys. Fluids* **14**, 3028–3038.
- SEVILLA, A. & MARTÍNEZ-BAZÁN, C. 2004 Vortex shedding in high Reynolds number axisymmetric bluff-body wakes: Local linear instability and global bleed control. *Phys. Fluids* **16**, 3460.
- SEVILLA, A. & MARTÍNEZ-BAZÁN, C. 2006 A note on the stabilization of bluff-body wakes by low density base bleed. *Phys. Fluids* **18**, 098102.
- SREENIVASAN, K R 1995 On the universality of the kolmogorov constant. *Phys. Fluids* **11**, 2778–2784.
- SREENIVASAN, K. R., RAGHU, S. & KYLE, D. 1989 Absolute instability in variable density round jets. *Exps. Fluids* **7**, 309–317.
- SRINIVASAN, K., HALLBERG, M. P. & STRYKOWSKI, P. J. 2010 Viscous linear stability of axisymmetric low-density jets: Parameters influencing absolute instability. *Phys. Fluids* **22**, 024103.
- STRYKOWSKI, P. J. & NICCUM, D. L. 1991 The stability of countercurrent mixing layers in circular jets. *J. Fluid Mech.* **227**, 309–343.
- STURROCK, P. A. 1958 Kinematics of growing waves. *Phys. Rev.* **112**, 1488–1503.
- TAM, C. K. W. 1971 Directional acoustic radiation from a supersonic jet generated by shear layer instability. *J. Fluid Mechanics* **46**, 757–768.
- TATSUMI, T. & GOTOH, K. 1960 Stability of free boundary layers between two streams. *J. Fluid Mech.* **7**, 433–441.
- TATSUMI, T. & KAKUTANI, T. 1958 The stability of a two-dimensional laminar jet. *J. Fluid Mech.* **4**, 261–275.
- THEOFILIS, V. 2003 Advances in global linear instability analysis of nonparallel and three-dimensional flows. *Prog. Aerosp. Sci.* **39**, 249.
- TWISS, Q. 1951a On bailey's theory of amplified circulating polarized waves in an ionized medium. *Phys. Rev.* **84**, 448–457.

- TWISS, Q. 1951*b* On oscillations in electron streams. *Proc. Phys. Soc. (London)* **B64**, 654–669.
- TWISS, Q. 1952 Propagation in electron-ion streams. *Phys. Rev.* **88**, 1392–1407.
- TYNDALL, J. 1867*a* On the action of sonorous vibrations on gaseous and liquid jets. *Phil. Mag.* **33**, 375–391.
- TYNDALL, J. 1867*b* *Sound: a course of lectures delivered at the Royal Institution of Great Britain*. New York: D. Appleton and Company.
- YU, M.-H. & MONKEWITZ, P. A. 1990 The effect of nonuniform density on the absolute instability of two-dimensional inertial wakes and jets. *Phys. Fluids A* **2**, 611–639.
- YU, M.-H. & MONKEWITZ, P. A. 1993 Oscillations in the near field of a heated two-dimensional jet. *J. Fluid Mech.* **25**, 323–347.
- ZAMAN, K. B. M. Q. & SEINER, J. M. 1990 Viscous effects on the instability of an axisymmetric jet. *Tech. Rep.* NASA-TM-102396. NASA Glenn Research Center.

Curriculum Vitae

Wilfried Coenen

Calle Canillas 30, 1º

28002 Madrid

Tel: +34 662 048 586

E-mail: wilfried.coenen@uc3m.es

Nacido el 18 de septiembre de 1982 en Sint-Truiden, Bélgica

Nacionalidad belga

FORMACIÓN ACADÉMICA

- 2005 - 2007 **Universidad Carlos III de Madrid**
Master en Ingeniería Matemática
- 2002 - 2005 **Technische Universiteit Eindhoven** (*Eindhoven, Holanda*)
Bachelor of Science en Física Aplicada (mayo de 2004)
Master of Science en Física Aplicada (agosto de 2005)
- 2000 - 2002 **Limburgs Universitair Centrum** (*Diepenbeek, Bélgica*)
“Kandidaat in de Natuurkunde” (Bachelor of Science en Física)
Con mención, nota media de 73 %
- 1994 - 2000 **Koninklijk Atheneum Hasselt** (*Hasselt, Bélgica*)
Diploma de instituto (rama científica)

BECAS Y AYUDAS

- 2006 - 2010 **Beca de Formación de Personal Investigador (FPI)**
Ministerio de Educación y Ciencia
- 2005 - 2006 **Beca de Doctorado**
Departamento de Ingeniería Térmica y de Fluidos
Universidad Carlos III de Madrid

PUBLICACIONES

W. Coenen, A. Sevilla, A.L. Sánchez “Absolute instability of light jets emerging from circular injector tubes” *Phys. Fluids*, 2008, vol. 20, 074104.

W. Coenen, N. Riley “Oscillatory flow about a cylinder pair” tubes” *Q. Jl. Mech. Appl. Math.*, 2009, vol. 61(1), 53-66.

ESTANCIAS DOCTORALES

2009 **University of Hawai’i at Manoa** (*Honolulu, EEUU*)

Department of Ocean and Resources Engineering
2 meses, en colaboración con Prof. Eugene Pawlak

2008 **University of East-Anglia** (*Norwich, Reino Unido*)

School of Mathematics
3 meses, en colaboración con Prof. Norman Riley.

2007 **University of California, San Diego** (*San Diego, EEUU*)

Center for Energy Research
3 meses, colaboración con Prof. Forman Williams.

IDIOMAS

Neerlandés: lengua materna

Español: nivel alto, escrito y hablado

Inglés: nivel alto, escrito y hablado

Francés: nivel medio, escrito y hablado

Alemán: nivel básico